Autonomous Unmanned Aerial Vehicle for Non-Destructive Testing

Dayi Zhang

Centre for Ultrasonic Engineering
Department of Electronic and Electrical Engineering
University of Strathclyde

A thesis presented in fulfilment of the requirements for the degree of

Doctor of Philosophy

Copyright

Signed:

Date: 21^{st} May, 2019

I would like to dedicate this thesis to myself, my parents, my friends and November 2018, a millstone in my life.

Acknowledgements

I would like to acknowledge my supervisor Dr. Gordon Dobie, Dr. Charles Macleod, Professor Gareth Pierce and Professor Anthony Gachagan for the opportunity to conduct this research and their engagement, supervision, mentoring and patience throughout. More, I would like to all my colleagues within the Centre for Ultrasonic Engineering (CUE) for their input on this research work. In particular, I would like to thank Dr. Kenneth Burnham, Dr. Rahul Summan, Dr. Aamir Khan for their ideas and suggestions on photogrammetric inspections; Advice given by Walter Galbraith, David Lines and Dr. Riliang Su has been a great help in ultrasonic inspections; and Robert Watson for his assistance during this research.

Furthermore, I must particularly mention the sponsors of this research, the Pressure Profile Systems (PPS), and the Engineering and Physical Sciences Research Council (EPSRC). I would acknowledge Dr. Jae Son and other staffs from Pressure Profile Systems for their support and suggestions. I would also like to thank the AscTec (the UAV manufacturer) for their technical support.

I would appreciate my friend, Jia, for encouragements during my most difficult time. I would also like to acknowledge the support provided by Ning during my PhD researches.

Finally, special thanks to my parents for their love, support and encouragement.

Abstract

Unmanned Aerial Vehicles (UAVs) are receiving increasing attention for use in Non-Destructive Testing / Evaluation (NDT / NDE), due to affordability, safety, and the ability to access areas where manned inspection is not practical. The mobility and size of UAVs offer the flexibility to quickly deploy remote inspections of large-scale assets and targets with complex geometry, such as wind turbine blades. The platform also provides airborne approaches to inspect high-risk sites, such as areas within nuclear facilities, which conventionally require inspectors to work at high altitude or in the presence of safety risks. Although ground crawler vehicles have been seen in such applications, UAVs offers true three-dimensional (3D) inspections and solve many challenging access problems.

Commercial UAV-deployed NDT inspections typically rely on a high-resolution camera that is manually piloted with a relatively large standoff distance, due to collision concerns and aerodynamic challenges. Close-range and contact-based inspections grant more detailed and accurate evaluations, whilst demanding an advanced UAV flight control system. This thesis evaluates two approaches to automated remote NDT, namely 3D photogrammetric and ultrasonic inspection. 3D photogrammetric inspection is a visual NDT method used to quantify surface integrity and detect discontinuities in a structure's coating. Compared with traditional inspections from offline images, a 3D photogrammetric inspection provides results with intrinsic position and location information, which is essential to meaningful surface condition evaluations. Structural health conditions, such as internal support material corrosion and fatigue crack formation beneath an outer surface coating, require contact-based measurement technologies. Contact-based

ultrasonic measurements grant the opportunity to remotely monitor the structural health of an industrial asset with enhanced internal integrity information.

This thesis has investigated and evaluated photogrammetric and contact-based inspections deployed by an aerial vehicle. The novel contribution of the research is to investigate the connection between the inspection accuracy and parameters in UAV-deployed inspections. Additionally, a novel, airborne, ultrasonic measurement system for the contact inspection of non-magnetic facilities was established. As far as the author aware, this is the first time such an inspection has been implemented and evaluated.

The implementation and modification of the autonomous flight controller on an AscTec Firefly UAV for indoor inspections are detailed within. A miniature planar laser scanner with a curve fitting was integrated into the system to map the UAV surroundings, measuring the displacement and alignment error against the inspection target. Brightness conditions, motion blur, and focal blur parameters influenced the accuracy of the photogrammetric inspections and were quantified and discussed. The inspection accuracy was improved from 0.3853 mm to 0.3098 mm using more detailed features on the mesh while the photogrammetric inspection was undertaken with a laser-based flight trajectory. The negative influences of these parameters were mitigated with an active flight path and an appropriate experimental setup, improving the reconstruction error by a factor of 13 versus the poorest scenario.

An autonomous UAV-deployed ultrasonic measurement system was developed for the inspection of vertical structures. The inspection constraints, such as transducer alignment and UAV positional accuracy, impacted the measurement error during the ultrasonic inspections. The influences of these constraints were evaluated and analysed. An additional contribution was presented on the improved inspection accuracy while applying a coded excitation to the ultrasonic measurement system to increase Signal-to-Noise Ratio. The maximum error was reduced from 0.83 mm to 0.66 mm in scenarios where the transducer was sub-optimally aligned.

Table of Contents

List of Figures

List of Tables

List of Acronyms

2D	Two Dimensional
3D	Three Dimensional
API	Application Programming Interface
CAD	Computer Aided design
DGPS	Differential Global Positioning System
DOF	Degrees of Freedom
EMAT	Electromagnetic Acoustic Transducer
FAA	Federal Aviation Administration
GNC	Guidance, Navigation and Control
GPS	Global Positioning System
GUI	Graphical User Interface
IMU	Inertial Measurement Unit
ISO	International Organization for Standardization
LQR	Linear–Quadratic Regulator
MP	MegaPixel
NDE	Non-Destructive Evaluation
NDT	Non-Destructive Testing
PEC	Pulsed Eddy Current
PID	Proportional–Integral–Derivative

PSL	Peak-to-SideLobe Level
RGB	Red, Green, Blue
RGBD	Red, Green, Blue, Depth
SDK	Software Development Kit
SfM	Structure from Motion
SIFT	Scale-invariant Feature Transform
SLAM	Simultaneous Localization and Mapping
SNR	Signal-to-Noise Ratio
SSH	Secure Shell
TCP	Transmission Control Protocol
TOF	Time of Flight
UART	Universal Asynchronous Receiver-Transmitter
UAV	Unmanned Aerial Vehicle
USB	Universal Serial Bus

Chapter 1

Introduction

1.1 Non-Destructive Testing

In the industrialised world, electric power systems, including wind turbines, power distribution lines, and nuclear facilities, are essential civil infrastructures supporting human life. Natural factors, which may include strong winds, oxidation, erosion, and ageing materials, can cause critical damage to this infrastructure, reducing the safe working lifetime. Naturally occurring damage can lead to further unscheduled failures or costly outages if the structures are not adequately serviced [1]. The consequences of such failures can be catastrophic disasters and the loss of life. Therefore, periodic inspections are required to monitor structural integrity, ensure continued safe and efficient operations, and prevent such failures.

Non-Destructive Testing (NDT), also known as Non-Destructive Evaluation (NDE), is an inspection method used to quantify structural health before failure occurs. It examines structures and components in a safe manner without causing damage. The process of such evaluations does not permanently destroy the serviceability of the target object; thus, components are still usable after inspection. The advantages are both operational and financial. Such evaluations provide an indication

of the structural health to experienced inspectors, which then leads to a decision on repairing or retiring the corresponding component. Such inspections can be undertaken in-situ, while the system is operating. Numerous NDT approaches have been developed, researched, and observed in many industrial applications over the last few decades. Examples of NDT techniques include liquid penetrant, magnetic particle, eddy current, and radiographic testing, as well as visual and ultrasonic methods used by many commercial and industrial inspection services [2].

Visual inspection is an optical technique used to evaluate the asset's surface condition [2]. Traditionally, visual inspection was conducted by a human inspector, where the human eye was the evaluation tool. To improve inspection repeatability and accuracy, while reducing the inspector's workload, numerous autonomous inspection approaches have been developed, whereby a robotic system with an optical sensor (e.g. vision camera) conducts measurements near the target structure. The onboard camera screens the surface for discontinuities and indentations. These captured images or videos assist inspectors in determining the asset's structural health. Such visual evaluation processes of the target object are called photogrammetry, which is defined as the measurement of objects from photographs [3]. Compared to traditional visual inspection based on the human eye, photogrammetric inspection offers more reliable evidence in assessing the surface condition. Currently, a 3D photogrammetric approach is being developed for industrial applications to further reduce the operator's workload. The inspectors uses a reconstructed 3D profile of the inspection target to quickly locate any abnormalities on the surface [4].

Ultrasonic inspection is another NDT method used to quantify structural conditions, and it is based on the propagation of a sound wave at an inaudible high frequency in air, solids, and liquids [5]. The sound wave consists of atoms vibrating in an elastic material. A typical ultrasound device produces mechanical vibrations of over 20 kHz [5]. Depending on the material and the boundary, ultrasound

waves can propagate inside a structure in many modes. Longitudinal waves and shear waves are the most common modes used in ultrasonic NDT inspections [5]. An ultrasound wave is generated by a piezoelectric crystal inside an ultrasonic transducer and it propagates into the target object. Wave reflections from the component's internal structures (e.g. discontinuities and defects) and the back-wall are converted into electrical signals by the transducer's receiver crystal. A post-processing system digitises the received signals and utilises time-of-flight or signal attenuation to locate the positions where the feature of the soundwave changed [2]. Ultrasonic inspection provides a detailed internal structure with a lower resolution, as compared to photogrammetric evaluations, which cover a large area at a rapid speed, albeit with no internal structural data [2].

1.2 UAV Inspections

Generically, NDT inspections can be conducted by a human operator, who inspects specific sections using a handheld sensor. Large-scale assets, such as wind turbine blades and selected areas within nuclear facilities, are often inconvenient to access and hazardous. Conventional manual inspection of these structures requires external scaffolding to support facilities for human access. The inspection targets may also need to be temporarily shut down during the inspection period. Additionally, human factors impact inspection accuracies. Inspectors will inevitably experience different psychological states during inspections, which may influence performance. Such human factors are seen in visual inspections, where the inspectors may overlook physical evidence [2].

The fourth industrial revolution is currently unfolding on an international scale. It is characterised by the fusion of multiple techniques and autonomous systems, leading to the development of more advanced manufacturing and infrastructure. The NDE Research Association (NDEvR) together with its industrial members

produced 5-, 10-, and 20-year visions on the role of NDT in this industrial revolution [6, 7]. In particular, inspection automation, including the widespread use of robots, advanced defect detection, and characterisation, as well as network connections of sensors, systems, and infrastructures, were identified to fundamentally address human error and conduct inspections in inaccessible areas.

In terms of safety, convenience, and legal requirements, autonomous inspection systems offer significant potential benefits. Such systems can precisely position NDT transducers and autonomously conduct measurements. Previous research at our university developed a miniature magnetic-based crawler vehicle [8, 9] equipped with multiple sensors (e.g. visual, ultrasonic, eddy current, and magnetic flux leakage), to perform NDT inspections on vertical structures [10]. The research was further developed into an industrial inspection product, named Silverwing Scorpion 2 [11].

Ground crawler robots addressed the access challenges and reduced the impact of human factors. However, compared with an Unmanned Aerial Vehicle (UAV), as shown in Figure 1.1, the crawler robots were only capable of conducting inspections in a 2D plane. The mobility and size of a UAV facilitate easy access to places where manual inspection is not practical; thus, providing global 3D coverage of target assets. The utilisation of UAVs is a well-established inspection method in use on various infrastructures, such as building surveys [12], detecting discontinuities on power cables [13], inspections of a nuclear waste container [14], evaluating structural conditions of bridges [15], and outdoor sculpture survey [16].

Figure 1.1: AscTec Firefly, the aerial platform utilised in this thesis

1.3 Aims, Objectives and Methodologies

Previous research and industrial applications within the field of NDT inspections using UAVs have highlighted the challenges and constraints of airborne inspections in practical industrial deployments. Conventional UAV-deployed photogrammetric inspections rely on a high-resolution camera, capturing images at a relatively large standoff distance. Close-range photogrammetric inspections increase the level of detail that can be acquired from the inspection object, enhancing accuracy. Contact-based ultrasonic inspections offer thickness mappings of the target object, providing more detailed internal structural information. However, manually deploying a close-range or a contact-based inspection using a UAV increases the likelihood of a collision and requires a highly developed skillset and the intense concentration of the pilot. Therefore, the aim of this thesis is to develop an aerial platform to autonomously conduct the remote NDT inspections of large-scale assets, such as wind turbines and facilities inside nuclear stations and provides precise inspection results.

In particular, the objectives of this thesis are:

- To investigate the parameters that impact the 3D photogrammetric inspection accuracy, including environment brightness conditions, motion blur, and focal blur.
- To integrate the laser scanner into the UAV platform and with strategies to achieve waypoint generations on the flight and improve the accuracy of the close-range photogrammetric inspection.
- To develop a novel, airborne, contact-based ultrasonic thickness measurement system to fill the gap in internal structural health monitoring of non-magnetic facilities using UAVs.

- To evaluate the challenges during the UAV-deployed ultrasonic measurements, including the electromagnetic interference from UAV motors, transducer alignment error and UAV positional accuracy.

This research was based in the indoor laboratory, using an existing AscTec UAV with a customised PID-based controller allows for autonomous indoor flight (detailed in Chapter 2 and Chapter 3). The integration of the laser scanner is described in Chapter 3. The laser scanner maps the surroundings for the flight controller.

In Chapter 4, a section of the wind turbine blade, a decommissioned part of a Gaia–Wind turbine, was photogrammetric inspected using the modified UAV [17]. The influences of image parameters such as environmental light levels, motion blur and focal blur were evaluated in terms of their impact on the inspection accuracy. These were presented by the comparisons between the reconstruction results from different experiment setups and a ground-truth reference model.

In Chapter 5, a novel, contact-based ultrasonic inspection system was developed and integrated into the UAV. A 1 m^2 aluminium plate of 15 mm nominal thickness, including varied thicknesses and simulated defects was fabricated to mimic an industrial inspection scenario. Multiple independent thickness measurements were deployed by the UAV with a 5 MHz split-crystal probe. The influences of electrical noise and UAV positional accuracy were evaluated in terms of their impacts on the thickness measurement errors and the Signal-to-Noise Ratio of the ultrasound A-scan signals. The connection between the transducer alignment angles and inspection accuracy was established based on the measurements from the KUKA manipulator, which isolated flight uncertainties from different UAV trials to provide accurate results.

1.4 Contributions to Knowledge

This thesis presents a number of unique, novel, and industry-focused contributions to the field of UAV-deployed NDT inspections, as follows:

- The parameters impacting photogrammetric inspection accuracy, environment brightness conditions, motion blur, and focal blur were quantified and discussed. As far as the author aware, this is the first time such impacts have been evaluated. Over the range of parameter values studied, the poorest scenario (in the dark environment, error range = 68.00 mm) was observed to cause a degradation in reconstruction error by a factor of 13 versus the optimal (in the bright environment, error range = 5.09 mm).

- A laser scanner-based photogrammetric inspection of an object with complex geometry was performed, which demonstrated higher accuracy with appropriate experimental setup and an adaptive flight path based on laser data. The laser corrected flight path maintained the standoff distance and reduced errors by a factor of 2.7, from 13.56 mm to 5.09 mm.

- An autonomous background feature removal algorithm was developed based on the integration of the laser scanner data. The 3D profile reconstructed from these post-processed images showed that the backgrounds contributed to the current reconstructions. Despite these post-processed images were not aligned properly, the background features did not impact the reconstruction accuracy. These results demonstrated the current limitations of UAV-deployed photogrammetric inspections, which will serve as the basis for future research.

- A discontinuity detection algorithm was developed. The algorithm highlighted the abnormal areas, which potentially contained discontinuities, helping inspectors locate the positions of surface defects.

- The ultrasonic inspection system for UAV-deployed inspections was developed. The payload was composed of a 3D-printed, lightweight, mounting structure, a commercial 5 MHz split-crystal ultrasonic probe, and customised FPGA-driven ultrasonic transceiver circuitry. These were mounted onto the UAV to perform the autonomous contact-based ultrasonic thickness measurements. The Xylo-EM FPGA [18] acts as a communication bridge buffers the data stream. It additionally offers the capabilities to customise ultrasound excitation wave pattern, tune variable amplifier gain programmatically, without manual hardware modification.

- The parameters, transducer alignment error, electrical noise, and UAV positional error, which could have potentially influenced the accuracy of the ultrasonic thickness measurements were evaluated and discussed. A coded excitation method was proposed for integration into the ultrasonic thickness measurement system. A 13-bit Barker code sequence was evaluated, which improved the Signal-to-Noise Ratio within the current UAV ultrasonic inspection system and reduced the error from 0.83 mm to 0.66 mm in the thickness measurements. The findings demonstrated the challenges of the current contact-based ultrasonic measurement system, which will serve as the basis for future research.

1.5 Thesis Structure

This thesis is structured as follows:

Chapter 2 reviews different types of aerial platforms. The AscTec Firefly, a commercial UAV platform, was studied and adapted for the realisation of a research-focused NDT platform. The development of the UAV onboard controller's software and firmware and the off-board ground-based controller's software workstation are detailed.

Chapter 3 presents the implementation and evaluation of the aerial platform's PID (Proportional–Integral–Derivative) controller [19]. This chapter also describes the integration of a miniature laser scanner with a curve fitting procedure. The controller with the laser scanner provides the UAV autonomous navigation, positional control, and adaptive trajectory generation, which is fundamental to the autonomous NDT inspections, as described in Chapter 4 and 5. The controller and laser scanner performance are evaluated and discussed. The work described in this chapter and Chapter 2 resulted in a UAV with the capability to autonomously conduct indoor inspections.

Chapter 4 focuses on the implementation and challenges quantifications of the photogrammetric inspections using the aerial platform. The impact of three parameters (i.e. environmental brightness conditions, motion blur, and focal blur) on the accuracy when deploying the UAV-based photogrammetric inspections are quantified and reviewed. The results demonstrated the accuracy improvement with the flight path generated from the laser scanner data when close-range inspecting a complex-shaped object. The contribution of the background features in the current 3D reconstruction pipeline are analysed. This chapter also describes a discontinuity detection algorithm to extract and highlight the features on a 3D profile.

The implementation and challenges of the contact-based ultrasonic inspections using the aerial platform with a conventional ultrasonic transducer [20] are presented in Chapter 5. The UAV-deployed inspection accuracy, including thickness measurement and positional accuracy, was dependent on many factors. As such, transducer alignment constraints, electrical noise, and UAV stability are evaluated and discussed. This chapter also presents a 13-bit Barker code sequence to improve SNR and reduce measurement errors from 0.83 mm to 0.66 mm.

Finally, Chapter 6 summarises this research on a UAV-deployed NDT inspection system and provides suggestions for future research.

1.6 Publications Arising from This Thesis

D. Zhang, R. Watson, G. Dobie, C.N. MacLeod, A. Khan, S.G. Pierce, 'Quantifying Impacts on Remote Photogrammetric Inspection Using Unmanned Aerial Vehicles', *Engineering Structures*, Submitted

D. Zhang, R. Watson, G. Dobie, C.N. MacLeod, W. Galbraith, S.G. Pierce, 'Implementation and Evaluation of an Autonomous Airborne Ultrasound Inspection System', *Automation in Construction*, Submitted

D. Zhang, K. Burnham, L. Mcdonald, C.N. Macleod, G. Dobie, R. Summan, S.G. Pierce, 'Remote inspection of wind turbine blades using UAV with photogrammetry payload',*56th Annual British Conference of Non-Destructive Testing - NDT 2017, Telford, United Kingdom, 2017* (Awarded with 'The William Gardner Award')

S.G. Pierce, K. Burnham, D. Zhang, L. Mcdonald, C.N. Macleod, G. Dobie, R. Summan, D McMahon, 'Quantitative inspection of wind turbine blades using UAV deployed photogrammetry', *9th European Workshop on Structural Health Monitoring, Manchester, United Kingdom, 2018*

D. Zhang, R. Watson, G. Dobie, C.N. MacLeod, S.G. Pierce, 'Autonomous Ultrasonic Inspection Using Unmanned Aerial Vehicle', *2018 IEEE International Ultrasonics Symposium - IUS 2018, Kobe, Japan, 2018*

Chapter 2

Aerial Platform for Non-Destructive Testing

2.1 Introduction

UAVs equipped with NDT inspection payloads have been commercialised in many applications using photogrammetric [13] and thermography inspection techniques [21]. The platform developed in this thesis is different to existing commercial UAVs in that it uses an autonomous controller to perform close-range and contact-based inspections, instead of being manually piloted by a qualified UAV expert at a significant standoff distance. The AscTec Firefly [22] was used as the platform for this research and development, detailed in Section 2.4.2. This UAV is available in the laboratory and has been utilised in the previous research [23]. Moreover, this UAV offers the flexibility to modify for researches, in addition to the reliability and safety features as a commercial product. However, this UAV was designed to conduct outdoor photogrammetric inspections with the aid of conventional GPS. This was problematic, as the experiments herein were conducted in a laboratory-

based environment; thus, system adaptations and further developments of the AscTec UAV were required.

This chapter presents the modifications to the AscTec Firefly platform in order to enable NDT inspections with the guides from the flight controller. This chapter begins with literature reviews of traditional aerial vehicles, followed by novel UAV designs, and UAV positioning systems. The development of the research platform is then detailed, including modification of the existing controller's firmware, which increased wireless communication throughput. The resultant firmware extended the bandwidth to facilitate more frequent control communications. The software applications running on the onboard and off-board computers were designed, including the integrations of multiple peripherals, NDT payloads, control algorithms, and the UAV positional tracking system. The graphical user interface, included in the software on the off-board workstation, monitored the instantaneous flight status. The subsequent chapter will describe the flight controller design and the laser scanner integration into this aerial platform for flight stabilisation, navigation, and adaptive waypoints generation.

2.2 Unmanned Aerial Vehicle Overview

UAV technology began with pilotless bombers (the predecessors of current guided missiles) called "aerial torpedoes", developed in 1917 by the U.S. Army. The biplane wood bomber carried a 136 kg explosive payload and attacked targets up to 50 km away with a 3.2 km positional accuracy. Using previously determined wind speed, wind direction, and the distance to the target, the number of engine revolutions required for the bomber to travel to the target was calculated. When the engine had turned the designated number of the revolutions, the explosive fuselage fell on the target and completed the unmanned attack [24].

Low altitude, miniature, and short-range UAVs are popular in the civilian field, widely seen in rescue missions and for geographic mappings. Currently, firefighting and rescue teams rely on manned helicopters. Hot temperatures and toxic smoke directly threaten the safety of the onboard pilots. UAVs made from temperature resistant materials can survive in these environments and thereby offer the capability to remotely control the UAV from a safe area. These commercialised rescue UAVs utilise a sensing system to perform real-time scene mapping, streaming details to the ground team [25, 26]. Researchers in this field are developing more robust, efficient, and autonomous UAV sensing platforms. Multi-UAV rescuing systems, presented in [27], demonstrated the enhanced task efficiency with swarm UAV cooperation. Such UAVs can also play a role in temporary infrastructure to provide essential support to victims. Guevara et al. proposed a concept to utilise multiple UAVs as mobile stations to establish a temporary communication channel if cellular infrastructure was destroyed [28].

UAVs are also popular in geographic sensing and land surveying. With the positional information from the outdoor navigation system (e.g. GPS), UAVs can be utilised for surveying, for instance, building infrastructures [29]. Images captured by the onboard camera are processed using software to provide a 3D geographic map. Researches are enhancing the accuracy of UAV-deployed remote mapping and are developing autonomous real-time sensing. UAVs equipped with a photogrammetric payload have been shown to deliver high accuracy mapping for a small-scale scene, such as office areas [30], as well as large-scale infrastructure [31] and land surveys [32]. Geographic mapping includes agricultural surveys, which remotely monitor food crops. 3D reconstructions offer agronomists a rapid estimate of the height of plants and estimated health [32, 33].

The dimensions and flexibility of UAVs allow for remote inspection of inaccessible assets, while reducing risk during evaluations, which conventionally required human operators to work at high altitudes or in the presence of safety risks. According to the Health and Safety Executive [34] working at height is dangerous and should

be avoided as much as possible. Current UAVs are typically remotely piloted by experienced users in order to perform non-contact inspections. Photogrammetric inspection is one such approach whereby UAVs equipped with a high-resolution camera evaluate the surface condition of the target object [35]. This technique has been demonstrated by many commercial and industrial inspection services [36]. Thermographic inspection is another non-contact evaluation technique. It uses a thermal camera to monitor heat distribution in damaged or worn structures [37]. In more sophisticated cases, it observes infrared absorption spectra specific to a gaseous hydrocarbon [21]. Thermographic inspection is also used in solar panel defect detection [38].

Numerous UAV systems have been developed, researched, and observed in many industrial applications over the last few decades. Several aerial vehicles, including fixed wing, inflatable, single- and multiple-rotor, have been utilised by commercial and industrial services, including solar farm inspections using a fix-wing vehicle [39]; bridge inspections by a single-rotor helicopter [40] and power line inspections by an inflatable airship [41].

2.2.1 Fixed Wing Aerial Vehicle

A fixed wing configuration is widely used on modern aircraft, from military bombers to commercial jet airliners. The engines on the vehicle generate the forward thrust to take-off. Flight control surfaces, such as ailerons and stabilisers, are utilised to control the craft's yaw, roll, and pitch orientations. Such an aircraft is being used for unmanned geometry mappings [42].

Indoor NDT inspections typically require craft manoeuvring around the target objects, stabilising in desired positions, and vertically taking-off / landing in a relatively small space. This remains problematic, as fixed-wing aerial vehicles can only undertake forward movements. Additionally, such vehicles need a large

space for free flight and a runway for take-off and landing. Hence, the fixed-wing aircraft is not preferred for indoor inspections, due to its kinematics.

2.2.2 Inflatable Vehicle

An inflatable vehicle, also known as an airship, consists of an air bag filled with a buoyant gas, which is lighter than air (e.g. helium). The kinematics of this aerial vehicle are similar to a balloon, where the lift is generated by the buoyancy of the low-density gas. Independent actuators and engines are installed below the craft to control the vehicle's flying direction. The concept of the aircraft's motion control is illustrated in Figure 2.1.

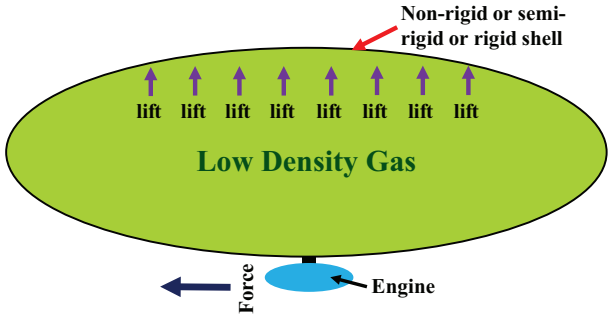

Figure 2.1: Motion control of an inflatable aerial vehicle

Unmanned autonomously controlled airships were used in navigation and robust path planning [43, 44]. Specific airships equipped with an IMU (Inertial Measurement Unit) and a camera were utilised for indoor localisation and undertaking navigation and mapping tasks [45, 46]. Compared with other aerial vehicles, airships demand less power to stabilise in a hover condition, thus, airships generally have higher power efficiency and longer flight endurance. However, the airship payload mass is limited by the volume and the density of buoyant gas. Additionally, such airships are sensitive to wind gust in outdoor environment, which is problematic for outdoor inspections [47].

2.2.3 Rotating Wing Vehicle

A conventional helicopter (as shown in Figure 2.2(a)) is a rotating wing vehicle, using one rotor with a large propeller and a small rotor at the tail section. The rotation of the main blade generates the aircraft's lift. The tail rotor is used to counterbalance the yawing effect, caused by the main rotor. Roll and pitch angle are controlled by adjusting the orientation of the main rotor, whereas the rotor at the tail controls the aircraft's yaw angle [48].

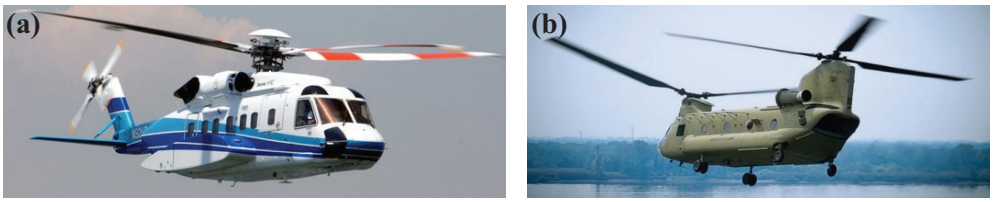

Figure 2.2: Helicopters (a) Sikorsky S-92 [49] (b) Boeing CH-47 CHINOOK[50]

The kinematics of the single rotor helicopter naturally induced the yawing effect of the main rotor, originated from the torque. Part of the helicopter's power is used to drive the tail rotor to counterbalance this effect, reducing power efficiency. Twin-rotor vehicles, powered by rotors at opposite ends of the aircraft, were designed to lessen the impact of the yawing effect, whilst lift is generated by two rotors. Thus, compared with single rotor helicopters, such vehicles have better power efficiency.

Tandem rotor aircraft (as in Figure 2.2(b)) feature two rotors located at the ends of the aircraft. The torque from both rotors generates the lifts for vertical movements and hovering. The two rotors are mechanically connected to ensure synchronisation and avoid propeller collisions. Differential rotor speeds and propeller thrusts control the aircraft's yaw and pitch orientations.

2.2.4 Quadrotor Aerial Vehicle

A quadrotor aerial vehicle is typically composed of four independent electric motors, which are installed symmetrically, parallel to the horizontal plane [19]. The lift is generated by the thrust of all the motors. The differential rotor thrusts control its yaw, roll, and pitch orientations, as shown in Figure 2.3. Rotor 1 and rotor 3 rotate anticlockwise, whilst rotor 2 and rotor 4 rotate clockwise.

The thrust levels of the four propellers can be adjusted separately by the controller. Increasing or reducing the rotor thrust at opposite ends can produce pitch or roll torque, resulting in accelerations in the aircraft's horizontal plane. Differential thrusts from two clockwise or anticlockwise rotors provide a control interface for the aircraft's orientation. The aircraft's vertical alterations are conducted by adjusting all rotor thrusts [19]. The concept of the quadrotor has been extended to the hexarotor design, which is powered by the differential thrusts from six electric motors [22].

Numerous limitations and constraints exist on current quadrotors. The payload capacity is relatively lower than the vehicles described previously. Since the large-scale, fuel-powered engines are not suitable for civilian applications, quadrotors are driven by electric motors and powered by an onboard battery. This design minimises the vehicle's size and weight, and offers more flexibility, but it also reduces the payloads that can be lifted by the aircraft.

Flight endurance is another constraint of quadrotors, and is dependent on the UAV payload mass. A heavier payload reduces the flight time. AscTec provided a relationship between the flight endurance of an AscTec Firefly UAV (the UAV utilised in this thesis) and its payload mass, shown in Figure 2.4 [22].

Aerodynamics are a challenge for the quadrotor flight control system. Wind gusts during outdoor inspections, as well as near-surface instabilities during contact inspections, are examples of the aerodynamic challenges that destabilise the UAV.

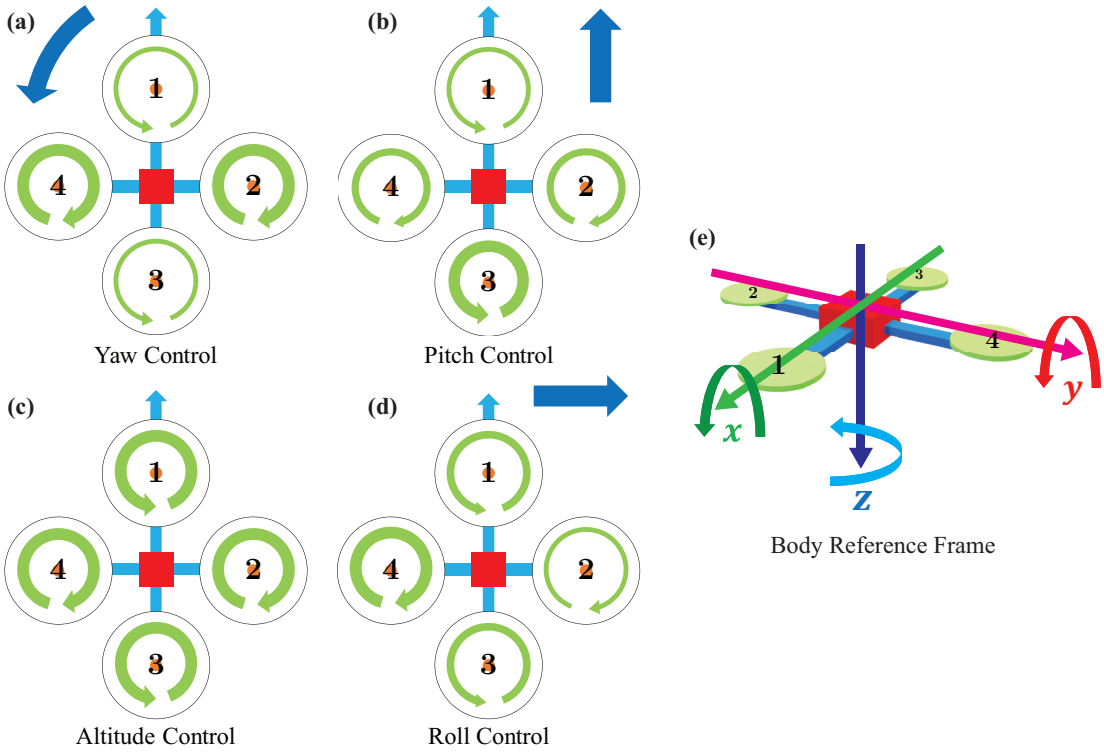

Figure 2.3: The kinematics of a typical quadrotor, adapted from [51]

Quadrotor kinematics are based on the combination of thrusts from multiple motors. When the aircraft is approaching the inspection target, the air between the aircraft and surface is pressured, leading to a reaction force applied to the aircraft's body, which is observed as unstable flight. Ground effect, a similar aerodynamic phenomenon, is commonly observed when the craft is hovering near the ground [48]. Here, the reaction force from the ground generates an upward force that lifts the quadrotor, which causes the aircraft to bounce near the boundary of the ground effect [52]. When conducting inspections under strong wind conditions (typically during outdoor inspections), the UAV motor speeds adjust frequently to overcome this challenge. To lessen the negative impacts of such aerodynamic challenges and stabilise the UAV, a controller is required to counteract the reaction forces from the quadrotor's surroundings.

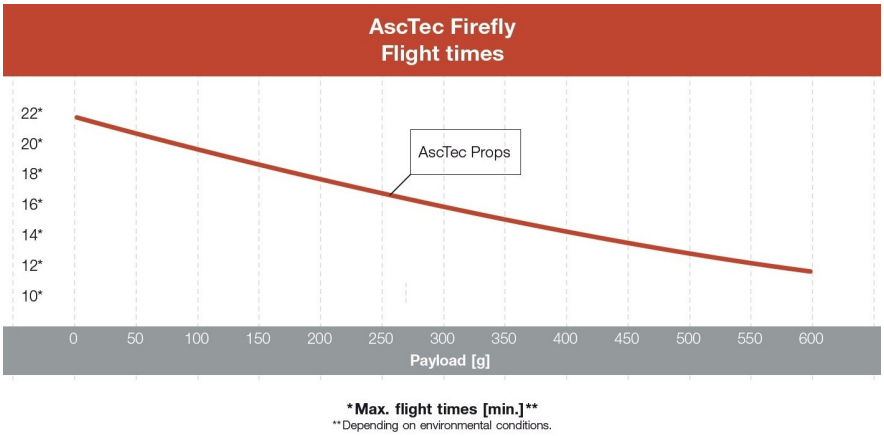

Figure 2.4: Relationship between flight time and Firefly payload mass [22]

2.2.5 Novel UAV Designs

2.2.5.1 Hybrid Design

To overcome the UAV's aerodynamic challenges and increase battery efficiency, researchers designed hybrid UAV structures, which are a combination of an aerial vehicle and a ground vehicle. Authors in [53] added steering wheels below the conventional UAV, as shown in Figure 2.5. A sticker structure was installed in the centre of the UAV to provide a roll angle offset, converting the thrust to power the UAV ground movements. The UAV endurance time was increased by a factor of two when hovering near the ground, as compared with a conventional quadrotor. Further enhanced battery efficiencies were seen when the vehicle was moving on a smooth surface, such a concrete block.

Figure 2.5: Novel UAV structure with steering wheels [53]

Findlay et al. designed a hybrid vehicle system composed of a traditional UAV with a ground crawler robot attached underneath, as shown in Figure 2.6 [54]. This hybrid structure can be split into two separate vehicles. The UAV transports the crawler robot to a target position. After finishing the task, the ground vehicle attaches to the UAV. The thrust from the UAV lifts the entire system and carries the ground vehicle back to its start position. The ground vehicle can also cooperate with the UAV to undertake tasks requiring three-dimensional access. Simulation results proved the concept and demonstrated the stability of this design. However, the system equipped with the ground vehicle required extra mechanical supports and more UAV power to lift the entire system.

Figure 2.6: CAD model of hybrid UAV and crawler robot structure [54]

HyTAQ is another novel hybrid craft, as shown in Figure 2.7 [55]. The researchers attached a lightweight plastic cage around a conventional quadrotor, giving the system two operation modes (terrestrial and aerial). The internal flying mechanism was mechanically decoupled from the outside plastic cage. When the system flies close to an obstacle, the thrust from motors is converted to a force rolling the cage on the obstacle surface. The cage is made from rods, which reduce the aerodynamic impact on the quadrotor inside the cage, as well as the total mass. This special UAV can naturally prevent physical damage from collisions. Compared with conventional UAVs, the obstacles and ground surface extended the UAV battery life by a factor of four. The concept was observed in the industrial inspection UAV, Flyability Elios [56].

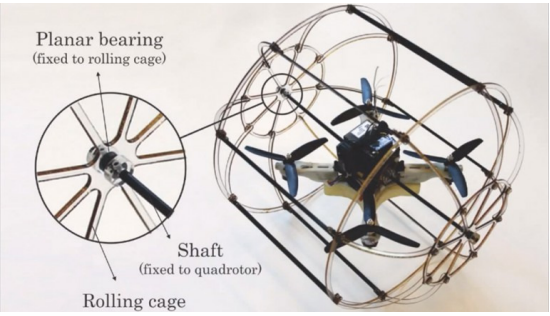

Figure 2.7: Hybrid terrestrial and aerial quadrotor [55]

2.2.5.2 Tiltrotor Aircraft

Tiltrotor is an aircraft that has the capability to take-off and land vertically, similar to a conventional helicopter. The tiltrotor consumes a similar amount of power as a fixed-wing aircraft, with tilted engines installed on the craft's wing. During vertical take-off and landing, motors are tilted 90° upwards to create a vertical airspeed. After reaching the desired altitude, motors are tilted back to the horizontal orientation, providing forward airspeed. Compared with conventional quadrotors, a tiltrotor requires less power to maintain altitude.

Because conventional quadrotor UAVs contain four motors in a horizontal plane, force can only be generated in the same direction. Hence, researchers are designing UAVs which can tilt the quadrotor motors to provide horizontal airspeed, and thereby extend the battery life while the UAV is moving forward [57, 58]. Figure 2.8 shows a hybrid craft concept design, which added four extra rotating motors [59], such that the thrust can fully be utilised to power ground and forward movement. When the motors are tilted parallel to the ground, the vehicle performs similarly to a ground vehicle. When the UAV is configured as a conventional quadrotor, the motors are rotated vertical to the ground, such that the thrust can be utilised to generate lift for vertical movements. However, as the authors stated, such designs increase the challenges for flight controller design.

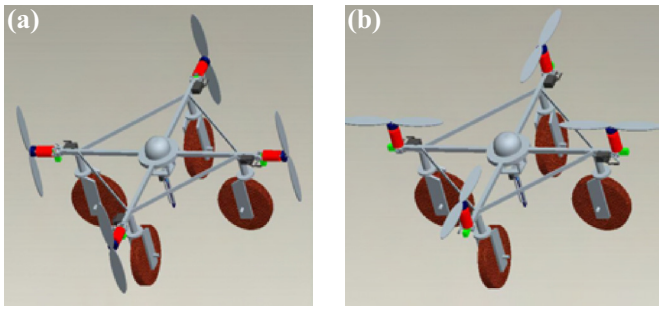

Figure 2.8: Two operation modes of a hybrid vehicle concept design: (a) ground vehicle (b) aerial vehicle [59]

Similarly, Elsamanty presented a concept that combined a ground vehicle and an aerial vehicle, as presented in Figure 2.9 [60]. The system had a ground mode and an airborne mode. The ground mode was proposed for movements similar to a ground crawler, whereas the airborne mode was a conventional quadrotor. Mode conversion on this vehicle was achieved by utilising solenoids with gravity to rotate the robot arms. Mode conversion in this design did not rely on extra motors to drive the robot arms resulting in a lightweight design that extended battery life.

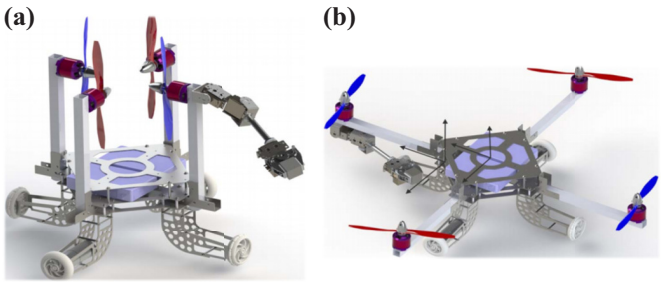

Figure 2.9: Two modes in a hybrid vehicle with solenoids: (a) ground mode (b) aerial mode [60]

2.2.5.3 Wall Climbing Robot

NDT inspections (e.g. ultrasonic thickness measurements) require a sensor to contact the measurement surface to acquire sufficient inspection signals. Researchers developed climbing and sticking UAV systems so that the UAVs could stably attach to a surface during inspections [61, 62]. The wall-stick robot offers better

contact to the asset surface, solves the near-surface aerodynamic challenges, and requires less effort to maintain sensor contact on the asset surface.

Myeong et al. designed a climbing UAV with locomotion equipment, as shown in Figure 2.10 [61]. The wheels were installed under four edges and driven by an independent power supply. These four wheels provided extra support to the UAV while it was sticking to the wall. When the robot inspected a vertical structure, such frictional forces were converted to adhesive forces to maintain contact between the robot and the inspection surface. The experimental results showed that the robot successfully attached to the vertical surface with an over 90% success rate. Additionally, battery endurance was also increased by 50% when conducting the contact operations, as compared to non-stick aerial vehicles.

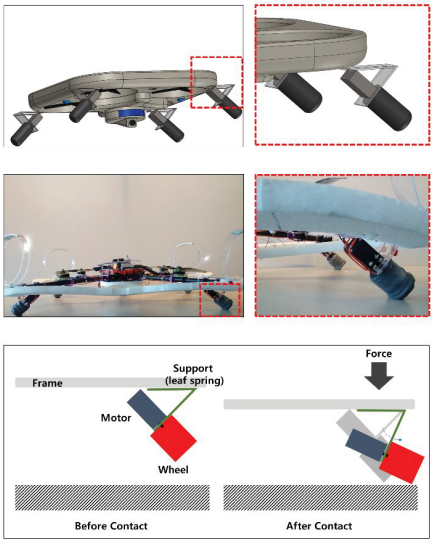

Figure 2.10: Diagrams of the wall-sticker and climbing robot [61]

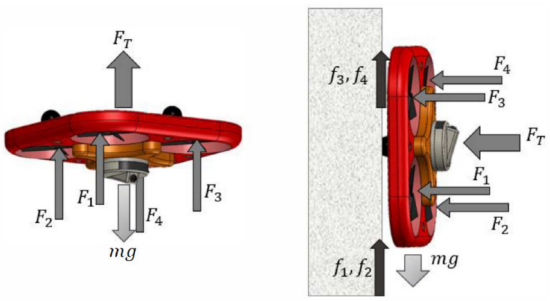

Figure 2.11: Diagrams of the climbing robot for wind turbine inspection [62]

Jung et al. designed a similar sticking and climbing UAV mechanism for wind turbine structural health monitoring [62]. The researchers installed several Omni wheels to allow for free movement on the target surface. The frictional force for sticking and climbing was generated by the motor's thrust, as shown in Figure 2.11.

2.2.6 Summary

In summary, fixed-wing aerial vehicles utilise two wings in a fixed position to produce forward airspeed and accomplish manoeuvring flight. Thus, such aircrafts are naturally limited to performing forward movements, and are thus not traditionally used in enclosed spaces, due to the space requirements for taking-off and landing.

Inflatable vehicles are driven by buoyant gas in an onboard airbag, and orientations / translations are controlled by independent actuators and engines. The advantage of inflatable vehicles is the low energy cost for hovering and maintaining a certain altitude. However, the massive volume occupation of the craft's airbag as well as the sensitivity to the wind gust make it not suitable for inspection with limited space and high accurate positioning.

Helicopter and tandem rotor aircraft are rotating wing vehicles, featuring two rotors to control the aircraft's actions. A combination of the thrust from the two rotors provides accelerations in six degrees of freedom. Similarly, a quadrotor and its evolution, a hexarotor, are composed of four or more rotors organised in the same horizontal plane. The aircraft again is controlled by the thrust combination of each motor. Compared to fixed-wing aircraft and inflatable vehicles, it can achieve vertical take-off and landing, as well as being dimensionally small, providing the flexibility to perform indoor inspections. The challenges for this type of vehicle are the payload mass limitation, flight endurance time, and aerodynamics. Therefore,

some innovative designs, including hybrid vehicle, tiltrotor, and wall climbing robots, were developed to fundamentally address the challenges of current UAV systems. However, such vehicles require unique controller designs for stabilised hover and flight control.

2.3 UAV Positioning Overview

As an autonomous robot system, positioning and acquiring knowledge about the surrounding environment are the most crucial tasks of the UAV [63]. Practically, such systems require instantaneous measurements, whereupon the controller can adjust the UAV rotor speeds for different control actions. This process utilises various sensors, including GPS, time-of-flight sensors, and visual odometry systems, from which the positioning information is extracted.

2.3.1 Global Positioning System (GPS)

The Global Positioning System (GPS) is a satellite-based system, providing object locations in 3D global coordinates. The current GPS was developed from the NAVSTAR GPS by the U.S. Department of Defence in the 1970s. The system has been fully operational since 1993 with 24 satellites in operation [64]. A GPS receiver requires the signals from more than four satellites to precisely estimate the location of the receiver in global coordinates, as shown in Figure 2.12.

The accuracy of GPS is affected by satellites' ephemeris, clock asynchronous effects, ionosphere and troposphere effects, multipath reception, and measurement error [65]. The Federal Aviation Administration stated that 95% of horizontal errors were less than 3.351 m [66]. Such positional accuracies are not suitable for precise UAV navigation. Thus, to improve the accuracy of the conventional GPS navigation system, researchers developed DGPS (Differential GPS), an enhancement of

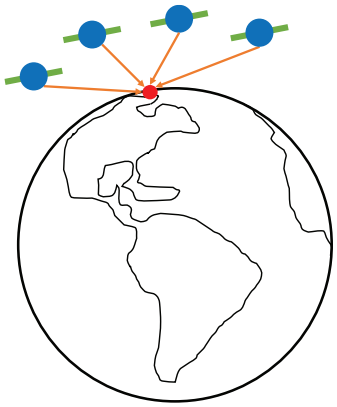

Figure 2.12: A generic representation of the GPS

traditional GPS. The system includes two GPS receivers. One is installed on the mobile UAV, and the other is stationary, as a ground truth reference to provide differential corrections of GPS satellites. Eisenbeiss presented the 3D trajectory accuracy of DGPS was 0.3 m, quantified using a RMAX helicopter [67]. Monteiro et al. described the accuracy of the DGPS was diminished with the increments of the distance between the reference station and mobile platform (about plus 0.2 m for each 100 km) [68]. Such DGPS systems have been integrated into the controllers for UAV navigations to provide more accurate position tracking than the traditional GPS [69, 70].

GPS cannot be applied within an indoor environment, where GPS signals are blocked by the building structure. Hence, GPS is typically used for UAV outdoor applications, providing rough positional estimations in broad areas, especially in inaccessible places. Amazon and other logistics companies are developing a GPS-guided UAV for goods delivery [71]. Researchers used a GPS sensor for UAV navigation along with a thermal infrared sensor to image geothermal environments [72].

2.3.2 Simultaneous Localization and Mapping

Since GPS sensors are not suitable for indoor environments, an indoor positioning system is required for UAV navigation. SLAM (Simultaneous Localization and Mapping) is one potential approach, where the robot utilises the onboard sensors to autonomously create and modify the map of an unknown environment, while simultaneously localising itself relative to this mapping [63].

This can be achieved through a laser rangefinder (described in Section 2.3.3), which utilises the attached laser sensor to navigate in a GPS-denied area [73]. SLAM is also used to perform indoor mapping in cooperation with IMUs [74, 75] in order to navigate a robot through a dark space [76]. SLAM can use a camera sensor (referred as visual SLAM), which is detailed in Section 2.3.4. Yang et al. utilised a monocular camera to map the UAV surroundings and navigate an autonomous landing with the aid of GPS signals [77]. Figure 2.13 is an example of visual SLAM, which is a grid map reconstructed by the UAV with a monocular camera [77].

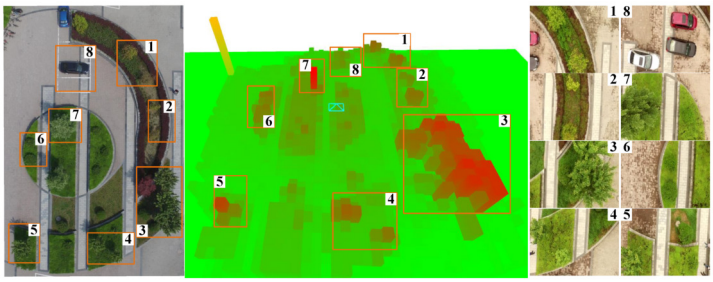

Figure 2.13: Grid map obtained by a monocular camera on the UAV [77]

2.3.3 Time-of-Flight Sensor

Time-of-flight sensors make use of the propagation speed of sound or light to estimate the standoff distance to a target object. In general, the distance, d, is

calculated by:

$$d = \frac{c \times t}{2} \tag{2.1}$$

where t is the time difference between the transmitted and received signals and c is the propagation speed. The speed of light in air is 3×10^8 m/s, whereas the speed of sound is 343 m/s at room temperature and standard pressure [63].

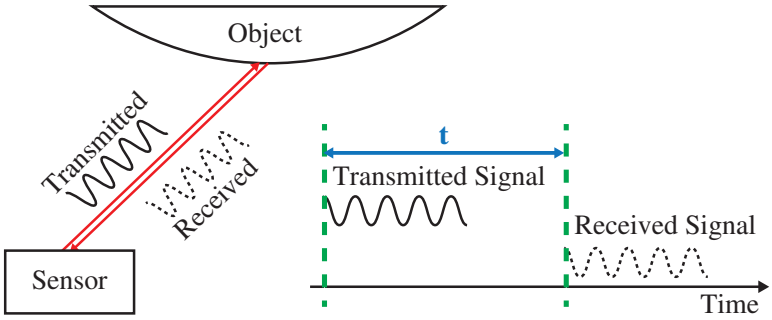

Figure 2.14: An illustration of a time-of-flight sensor

An ultrasonic ranging sensor is a time-of-flight sensor, which transmits a packet of ultrasound and measures the distance by using the time between the transmission and reception. The transducer typically excites a sound wave of between 40 kHz and 180 kHz, and the range is 0.12 to 5 m [63]. Multiple ultrasound sensors were used in the literature to map the surroundings of a UAV [78]. Twelve low-cost ultrasonic sensors were mounted on a UAV for obstacle tracking and avoidance. This setup facilitated 360° mapping of the UAV with angular redundancies. An additional ultrasonic sensor was installed vertically to cooperate with infrared sensors and provide altitude measurements for height maintenance and vertical movement control. The results showed that sensor reading became unreliable when standoff distance to the obstacle was over 2.2 m, because of sound wave attenuation in the air. In addition, soundproofing and rough surfaces were also identified as impacting measurement accuracy.

As an air-coupled transducer, the accuracy of such ultrasonic distance measurement sensors is influenced by room humidity and temperature [79]. This accuracy impact has been quantified by Papa et al., using an ultrasonic distance sensor to measure

UAV altitude during landing [80]. The paper documented the error from an uncalibrated sensor at room temperature as 2.54 cm, compared with the value after calibration.

A laser rangefinder is also a time-of-flight sensor that uses laser light instead of ultrasound to measure distance. Such a sensor is composed of a laser light emitter that emits a laser beam towards the target object and a receiver calculates the distance by using the light wave propagation time. A laser scanner, often referred as lidar, estimates distances at various angles. This uses a mechanism to rotate the transducer with a minor sweep, thereby covering the required scene in a 2D plane [63]. This type of sensor has been widely utilised to map the surroundings and measure the standoff to objects in applications of robotic obstacle avoidance and mapping [81, 82].

2.3.4 Visual Sensor

Using a visual sensor (e.g. camera) is a photogrammetric approach, which estimates the motion of a UAV using visual input [63]. It can be used for visual odometry [83] and visual SLAM [84]. Visual odometry estimates the robot's egomotion by only using the visual outputs from onboard cameras, whereas visual SLAM is the process of the robot localising itself in an unknown environment and simultaneously mapping the environment using the cameras attached to it. The onboard camera extracts surrounding features to achieve aircraft localisation and navigation. The camera can be traditional [85, 86], stereo [87], or depth [88].

Navigation utilises the monocular camera to capture images in various positions and orientations. These images are post-processed by machine-vision algorithms and further reconstruct the surrounding scene for localisations, obstacle avoidance, and real-time navigation [85]. Current state-of-art is focused on the implementation of UAV outdoor navigation, which does not require precise measurements. de

Croon et al. used a monocular camera with a machine learning algorithm on a powerful onboard computer to identify obstacles [86]. The algorithms developed by these researchers used a threshold to classify the sky and obstacles, assuming obstacles inside the camera's field of view had a significant difference in colour compared to the sky.

Monocular cameras provide only bearing information rather than the depth information of the surroundings, requiring the camera to be positioned in multiple poses to retrieve the depth. Stereo cameras, an emulation of the human vision system, inherently capture the optical features and the depth, reconstructing the 3D world from two distinct cameras. The relative position and orientation of the two cameras are known. Researchers utilised UAVs with stereo cameras to estimate the height and distance of obstacles [87], to avoid obstacles [89], and to position autonomously [90]. A stereo camera consists of two monocular cameras in the same baseline at a known distance acquiring photographs synchronously [91]. Extracting and matching similar features from two captured images allows for the calculation of the camera orientation versus the object. Figure 2.15 is a simplified diagram, demonstrating the principle of a stereo camera. Referring to Figure 2.15, using these two angles, θ_1 and θ_2, in combination with the given distance, x, between the two cameras, the object standoff can be obtained [63]:

$$d = \frac{\tan\theta_1 \tan\theta_2}{\tan\theta_1 + \tan\theta_2} x \tag{2.2}$$

Using structured light is another approach, which recovers the object depth by projecting a coded light beam onto an unknown 3D object's surface. The reflected lights with distorted patterns are captured by a specific camera to reconstruct the 3D pattern. Microsoft Kinect is a commercialised product using this technique [92]. The applications of such structured light cameras are visual odometry and real-time 3D mapping. A UAV equipped with a Microsoft Kinect camera has been applied to visual SLAM, which maps an unknown indoor area, localises,

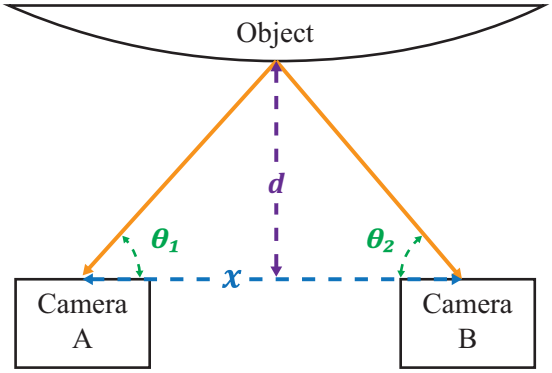

Figure 2.15: Triangulation diagram of a stereo camera. The camera measures the standoff, d, with respect to the given distance, x

and autonomously navigates [88] a path that facilitates obstacle avoidance [93]. The camera has also been used to provide indoor navigation and positioning [94]. It provides the positional tracking for the UAV and obstacles, such that the controller can adjust the UAV path.

However, as documented in [95], the main drawback of such camera-based navigations is that sensor performance depends on environmental conditions. Sunlight and surface condition influence sensor performance. In addition, to perform precise indoor navigation and positional tracking, the system requires real-time image feature extraction and matching to reconstruct the surroundings, which need a large number of onboard computational resources.

2.3.5 Vicon Tracking System

Vicon T160 is a commercialised photogrammetry-based tracking system, providing a global position in a measurement volume by using multiple off-board infrared cameras. Unlike the onboard cameras described in the previous section, Vicon is an off-board measurement system, which processes the data on a ground-based workstation. It utilises multiple optical cameras to extract positions of reflective markers and reconstruct the tracking object shape in a 3D volume. A custom-built camera lens, surrounded by a circular infrared light array, offers low distortion

images and continuous strobe, as shown in Figure 2.16. The system can track the positional six degrees of freedom (translations and orientations) of multiple objects at a 100 Hz updating rate [96].

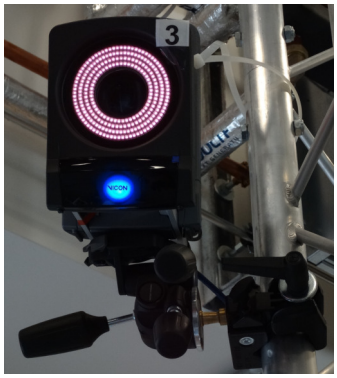

Figure 2.16: Vicon MX series T160 camera

Compared with the navigation sensors described previously, the Vicon system provides the most accurate indoor tracking and navigation. The system variability error is less than 0.025 mm when tracking a constant item and the mean error is less than 2 mm during dynamic testing [97]. The Vicon-based navigation system has been observed in existing state-of-art ground robotics tracking [98], multiple UAVs [99] ,and the previous University of Strathclyde research [100].

The experiments in this thesis were undertaken in the measurement volume, while the UAV was tracked by 12 Vicon T160 cameras. The cameras (as in Figure 2.17) constitute the Vicon MX capturing system, utilised for real-time positioning of multiple tracking objects inside the 280 m^3 ($8m \times 7m \times 5m$) measurement volume. The positions of these Vicon cameras have been optimised to cover the entire measurement volume. The Vicon system tracks the UAV position, as well as the position of the inspection target.

The Vicon tracking system requires more than three reflectors to locate the position of the UAV. An asymmetric combination of seven Vicon reflectors was placed on the top of the aircraft (as in Figure 2.18) to define the UAV as a unique object in the 3D measurement volume.

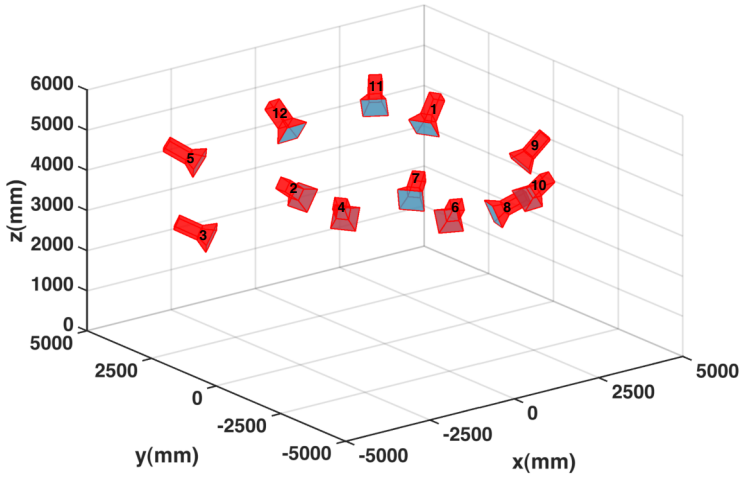

Figure 2.17: Vicon MX series measurement volume, which includes 12 Vicon T160 cameras

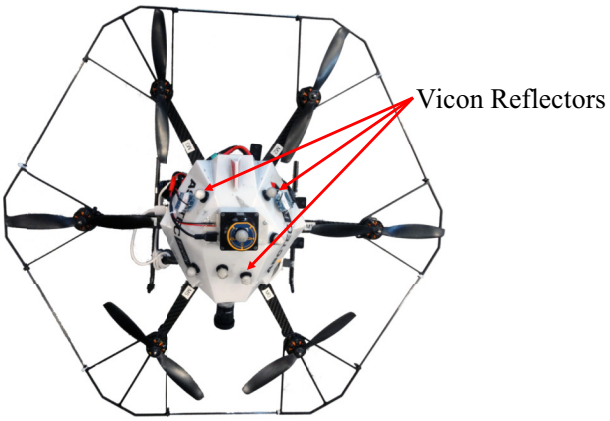

Figure 2.18: Vicon reflectors placed on the top of the UAV

The UAV translations and attitudes were transmitted from the Vicon tracking system to the controller workstation on the TCP (Transmission Control Protocol) profile with a 100 Hz frequency. The Vicon Datastream SDK (Software Development Kit) was used to decode the incoming TCP packets and extract the required information [96].

The UAV horizontal translation (x, y) is captured in the Vicon system coordinate, defined during the calibration process. The control commands for the UAV actions are based on the UAV coordinates. Hence, the (x, y) position in Vicon coordinates

is converted to UAV coordinates on the controller workstation. The coordinate conversion between the UAV and the Vicon system is related to the UAV real-time instantaneous pitch (θ), roll (ϕ) and yaw angle (ψ). The conversion can be described by the standard vector rotation equation [101]:

$$\begin{bmatrix} x' \\ y' \\ z' \end{bmatrix} = \begin{bmatrix} \cos\psi & \sin\psi & 0 \\ -\sin\psi & \cos\psi & 0 \\ 0 & 0 & 1 \end{bmatrix} \begin{bmatrix} \cos\theta & 0 & -\sin\theta \\ 0 & 1 & 0 \\ \sin\theta & 0 & \cos\theta \end{bmatrix} \begin{bmatrix} 1 & 0 & 0 \\ 0 & \cos\phi & \sin\phi \\ 1 & -\sin\phi & \cos\phi \end{bmatrix} \begin{bmatrix} x \\ y \\ z \end{bmatrix} \tag{2.3}$$

Since the pitch and roll angle are relatively small during the slow manoeuvring for NDT inspections, $\cos\theta \approx \cos\phi \approx 1$ and $\sin\theta \approx \sin\phi \approx 0$. Therefore, their influences are negligible, and the conversion can be simplified as:

$$\begin{bmatrix} x' \\ y' \\ z' \end{bmatrix} \approx \begin{bmatrix} \cos\psi & \sin\psi & 0 \\ -\sin\psi & \cos\psi & 0 \\ 0 & 0 & 1 \end{bmatrix} \begin{bmatrix} x \\ y \\ z \end{bmatrix} \tag{2.4}$$

where $\begin{bmatrix} x' \\ y' \\ z' \end{bmatrix}$ denotes the positional vector in UAV coordinates and $\begin{bmatrix} x \\ y \\ z \end{bmatrix}$ is the positional vector in the Vicon coordinates.

Processed position, altitude, and yaw information are fed into the PID controllers in the workstation, where the control commands are calculated for the UAV onboard controller (details are presented in Chapter 3).

2.4 Aerial Platform Design

2.4.1 Design Concept

Flexibility, such as loading different sensors for various inspection targets, and reliability were the main concerns during aerial platform development. The novel mechanical designs described in Section 2.2.5 lessened the negative impacts of some of the UAV challenges, improved battery efficiency, and offered more flexibility. However, such novel platforms were less robust and reliable than commercialised platforms. These novel structures had more challenges in terms of the controller design. Fixed wing and other conventional aerial platforms have natural limitations regarding the aircraft's kinematics and flexibility resulting in these configurations being unsuitable for indoor inspections.

The development for current research and ongoing future work is the focus of the proposed remote inspection platform. When designing the controller and algorithms, as well as integrating peripherals into the flight system, it is useful to track the instant sensor outputs, monitoring the intermediary controller output and flight status. This offers the capability to tune parameters in different function blocks independently and to monitor variable changes during flight. The current system is complicated, as signals and variables are described at a low-level, but it is convenient for ongoing research. The proposed platform provides hardware capabilities to deliver various kinds of NDT payloads to inspect large-scale assets. It also provides a sustainable platform for further development on the UAV control system or optimisation of results presentation to obtain higher stability and enhanced inspection accuracy.

In particular, the design specifications for this research are summarised as follows:

- The UAV was required to autonomously guided to follow the desired trajectories in the indoor laboratory environment.

- The UAV was required to carry a traditional photogrammetric sensor as well as an ultrasonic inspection system.
- The UAV was required to fly in a small standoff (< 1 m) for close-range and contact-based NDT inspections.

2.4.2 AscTec UAV Platform

A UAV platform for NDT evaluation must have an adequate payload capacity, have small dimensions to provide flexibility, and be reliable and robust enough to prevent system failures. Previous research assessed numerous commercial aerial platforms in terms of specifications and performance [102]. Considering the above requirements with respect to NDT inspections, a commercial UAV, the AscTec Firefly by Ascending Technologies [22], was used as the aerial platform to be adapted, as shown in Figure 2.19. The UAV is available in the laboratory and has been used in the previous research [23]. Additionally, the features of the UAV are suitable for this research. As a research-based platform, the UAV includes a reprogrammable high-level controller to customise the firmware. As a commercial product, it is featured a patented redundant propulsion system, which allowing the safe control with the loss of one rotor. The safe mode in AscTec Autopilot controller, triggered by a switch on the remote controller, grants extra safety protection to prevent unforeseen behaviours. The UAV's additional dedicated Core2 DUO computer offers the computational power to communicate with peripherals (e.g. onboard camera) for higher computational tasks. The UAV's six onboard rotors can generate 36 N of thrust in total, which creates the lift for take-off and thrust for movement. The maximum payload mass specified was 600 g, at a 1 kg net-weight with 15 minutes of maximum flight time under nominal conditions.

The UAV featured an onboard Core2 DUO computer (with a pre-installed Linux Operating System), which provides sufficient computational power to execute onboard software applications and communicates with serial devices, such as the camera and the laser scanner. The onboard laser scanner was utilised for distance and alignment measurements, detailed in Chapter 3. Various sensing payloads could be mounted to the UAV for different inspection prospects; for example, a machine vision camera, as shown in Figure 2.19, was utilised for photogrammetric inspections.

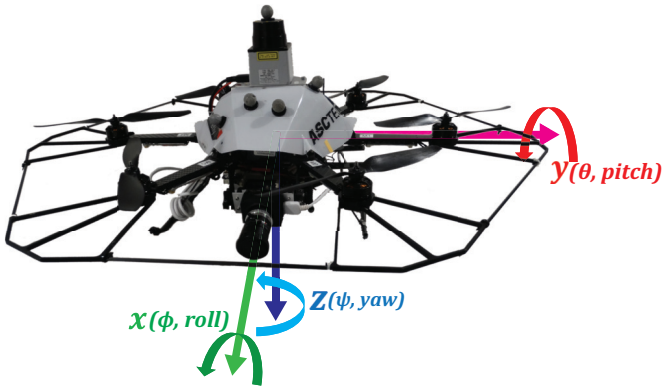

Figure 2.19: AscTec Firefly with a machine vision camera for photogrammetric inspections and the UAV's body reference frame used in this thesis

The UAV was equipped with two onboard ARM7 processors, which stabilise flight and offer redundancy to achieve robust action controls. However, this UAV was designed for outdoor photogrammetric inspections, and thus, the two controllers were programmed to navigate the UAV using GPS, in cooperation with an onboard barometer.

Previous research at our university developed a bipartite Guidance, Navigation and Control (GNC) system for outdoor surveying using the AscTec UAV [23]. The system was separated into two segments. The ground segment was used to provide desired waypoints and corresponding legs, while the onboard segment was the centre of autonomous GNC. The AscTec onboard high-level controller computed control commands based on the waypoints and legs from the ground segment and the instantaneous GPS readings. The works herein were undertaken

within a laboratory environment. The Vicon system cannot be integrated into the non-editable low-level processor or the high-level controller due to the incompatible communication protocol. Hence, the GNC has to be implemented on the off-board workstation to achieve the Vicon-based indoor navigations. This integration will be detailed in subsequent sections.

During the outdoor inspections, the Vicon indoor tracking system is required to be replaced by the GPS and barometer. Thus, the GNC can be implemented on the onboard segment, as described in [23]. However, because of the non-editable low-level controller, the GNC may still need to be integrated into the ground segment while utilising other positioning systems (e.g. DGPS).

Figure 2.20 presents a block diagram of the inspection UAV platform developed in this research, which is separated into two segments. Off-board control workstation is the ground segment, while the AscTec UAV is the onboard segment.

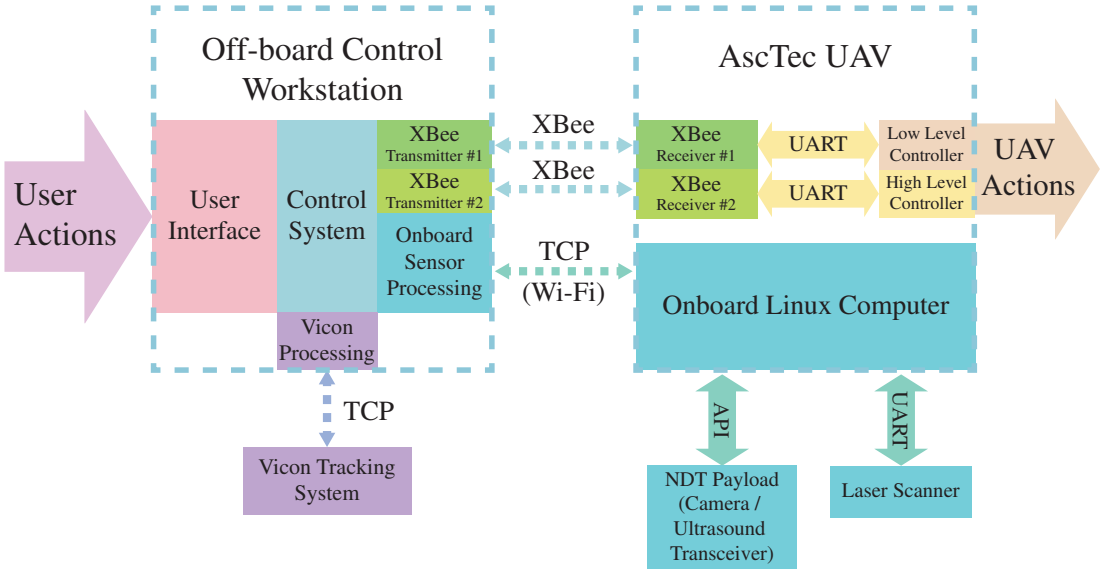

Figure 2.20: Diagram of the system structure utilised in this thesis

The ground segment is the centre of UAV GNC. In receiving, it decodes and displays the UAV instantaneous position from the Vicon system and UAV onboard sensor readings. In transmitting, it calculates the target waypoints, navigates the

UAV, computes the control commands based on the Vicon data, and passes the commands to the onboard segment through two XBee transmission channels.

The onboard segment is composed of three computational powers. Two XBee receivers correspond to two UAV microcontrollers, which were coded with the UAV control algorithms (e.g. motor speed control). The high-level controller receives control commands from the off-board workstation, decodes and transfers to the low-level controller to execute UAV motions. The onboard Linux-based computer was programmed in C++, which wirelessly transmits the onboard sensor data to the ground segment.

Since the GNC may still need to be implemented on the ground workstation for the use of other navigation systems, two XBee channels and the Wi-Fi channel between the ground and onboard segments may be applied during the outdoor inspections. However, with the increments of the distance between two segments, the data transmission throughput will be diminished. The AscTec UAV has a safety feature, which will automatically enter the emergency hovering mode once the remote controller communication is lost (distance $>$ 1 km) [103]. Hence, the maximum range of this UAV is 1 km. When the distance is increased to 1 km, the Wi-Fi and XBee throughputs will decrease from 36.2 Mbps to 7.8 Mbps [104] and from 250 kbps to 1.2 kbps [105], respectively.

2.4.3 UAV Firmware Modification

The UAV had two onboard processors: low-level and high-level. The low-level microcontroller processed key commands for low-level UAV communications, such as the UAV attitudes, positions, and motor speed control. The low-level controller is crucial for safe and reliable flight; thus, the firmware of this microcontroller was factory hard-coded and non-modifiable. In contrast, the firmware running on the high-level microcontroller was open-sourced, mainly utilised for data exchange

with less crucial sensors and customised functions. The control communications to these two controllers were based on the UART (Universal Asynchronous Receiver-Transmitter) protocol through the XBee Wireless modules [106]. To increase the control rate, the communication between the off-board controller workstation and UAV was separated into two independent wireless channels. One channel communicates with the low-level processor and streams the UAV configuration, such as the IMU sensor readings, using the AscTec Autopilot protocol [22]. The second channel is connected to the high-level processor and is utilised to transmit the UAV control commands using a customised protocol, listed in Table 2.1. A command processing function is developed in the firmware of the high-level microcontroller to decode incoming packets with a custom-built control protocol. This development substantially increases the average control rate from 7 Hz to 20 Hz.

Signal noises and byte errors were observed during platform development. These errors were introduced in the wireless communication stage, leading to the firmware on the microcontroller executing incorrect actions. To prevent UAV crashes from executing unexpected actions due to byte errors, a checksum byte was attached to the end of the command packet. The checksum is the sum of all command bytes and is generated on the off-board workstation. The UAV onboard processor checks the checksum byte and rejects the entire packet if the checksum created does not match the received byte. The firmware running on the AscTec high-level controller then transfers the control commands to the low-level processor to execute corresponding actions.

Table 2.1: Customised control protocol from the controller workstation to the UAV

Byte Index	Description
1	Header = 0x24
2	Control functions enable bits
3	Pitch command, most significant byte
4	Pitch command, least significant byte
5	Roll command, MSB
6	Roll command, LSB
7	Yaw command, MSB
8	Yaw command, LSB
9	Thrust command, MSB
10	Thrust command, LSB
11	Checksum, the sum of the 2nd to 10th bytes.
12	Footer = 0xFF

2.4.4 Software Development

2.4.4.1 System Structure

The aerial platform described in this thesis is composed of the hardware components (motors and sensors) and the software applications, which bridge between the hardware sensors, adjust the motor speed, and execute control actions. As shown in Figure 2.20, the software can be split into two contributions: the software application running on the UAV onboard computer and that running on the off-board, ground-based workstation. The software application on the UAV onboard Linux computer acts as a communication bridge for the onboard laser scanner, the NDT inspection payload, and the off-board workstation. The software offers the capability to wirelessly transmit the acquired sensor data and adjust the sensor parameters programmatically, without manual hardware modification. The computer buffers the sensor data and stacks data into TCP packets. The software was written in C++ and communicates with the controller workstation through a Wi-Fi protocol.

The software application running on the off-board controller workstation has two main functions. First, it offers a graphical user interface from which to manually adjust the controller parameters (e.g. UAV waypoints) during flight, and it monitors the intermediary sensor outputs and flight status. Second, it is the hub of the controller algorithms, where the sensor outputs are processed and converted to control commands. The implementation of the control algorithms and the integration of the sensors will be detailed in Section 2.4.4.2. The software was written in C# 7.0 using Microsoft .NET Framework 4.7 running in Visual Studio 2017 [107]. The .NET Framework provides a substantial number of libraries, such as Windows Forms, serial communications, and TCP networks.

2.4.4.2 Off-Board Workstation

The software on the off-board controller workstation, equipped with a quad-core CPU, processes the incoming data stream from multiple sensors. It includes a GUI (Graphical User Interface), sensor data integrations, and controller implementations. The GUI provides a simplified interface allowing the UAV operator to execute basic commands, such as take-off and landing. The real-time visualised variable values and sensor readings offer the capability to debug the software more efficiently. The application also records parameters, including UAV transitions, orientations, control commands sent to the UAV, sensor readings, and intermediary control outputs. The parameters are stored in the workstation, which is convenient for investigation after flight and system optimisation. Figure 2.21 is an example of this GUI.

The UAV flight control system, described in Chapter 3, is also integrated into this software application. The control system includes the implementation of the control theory in six degrees of freedoms the communications between multiple devices (e.g. Vicon, Wi-Fi, multiple CPU processors), and data processing. To increase processing speed, the application was written as a structure with multiple

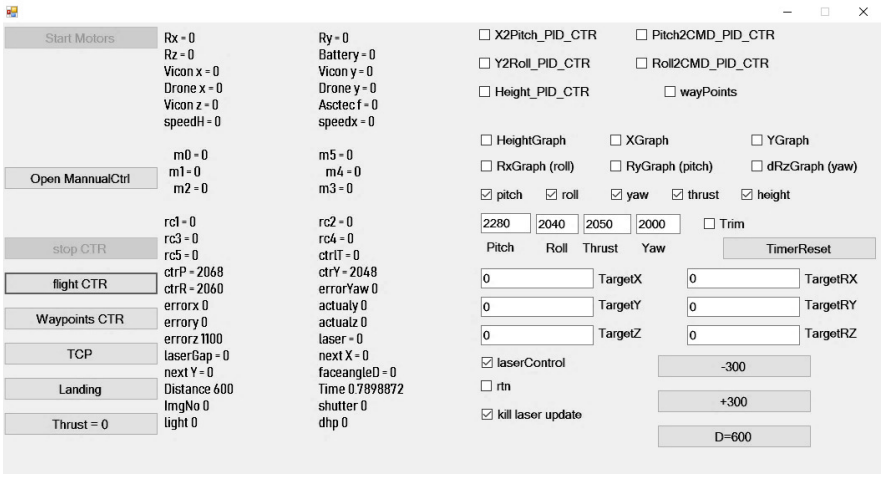

Figure 2.21: GUI developed with the software running on the off-board control workstation

threads, spreading the tasks into different CPU processing units. Thus, the sensor data can be handled simultaneously with low processing latency. The Vicon data and serial communications between the UAV and the flight controller are processed in different threads. The user interface is refreshed periodically within the system user interface thread.

2.4.4.3 UAV Controller Communication

The communications between the controller workstation and the UAV microcontrollers were facilitated with two wireless XBee modules [106]. Two onboard microcontrollers were connected to two independent XBee receivers, transmitting the signals in two independent wireless channels. The workstation communicated with two corresponding XBee transmitters using USB serial communication. The microcontroller on the XBee transmitter encoded the serial commands from the workstation to a packet, which was sent to the receiver. The XBee receiver decoded the wireless packets and transmitted the UART commands to the UAV microcontroller. Because of communication bandwidth and processing speed limitations, the serial speed was restricted in 57,600 bits per second. Such limitations have

been identified as one of the sources increasing control latency, leading to UAV positional errors [108].

2.4.4.4 Laser Scanner Communication

The communication between the onboard computer and the laser scanner was based on the *Hokuyo SCIP* 2.0 protocol, running on standard serial communication [109]. Once the onboard computer received an incoming packet from the laser scanner, it sent the packet to the off-board controller workstation through the wireless TCP protocol. The .NET Framework network library created a TCP client on the controller workstation, whilst the software on the UAV computer acted as a TCP server. Once the handshake process between the server and the client finished and the network connection was established, the UAV computer started triggering the laser scanner and transmitted the sensor data. On the workstation, communication ran on an independent thread. The incoming packets were initially placed in a buffer, and a notification was sent to the main thread. The main thread routinely checked the notifications and assigned another thread to process the pending packets.

2.4.4.5 UAV Onboard Computer

The software on the UAV onboard computer consisted of two parts: data acquisitions from the onboard sensors and data communication with the controller workstation. The communication protocol for data acquisition depended on the sensor. The laser scanner ran on the native C++ UART library, whereas the camera and ultrasonic circuitry required specific SDKs. Similar to the software on the off-board workstation, to achieve a high data acquisition rate, the software was developed in two threads. One thread was specified for the laser scanner acquisition. Image acquisition (during the photogrammetric inspections) or ul-

trasonic excitation (during the ultrasonic inspections) ran on the other thread. A C++ native network library was applied to establish the TCP server, which was intended for the wireless communication with the controller workstation. The server started the socket during the software initialisation stage and waited for the client to establish the network. Once the client (controller workstation) connected to the server, the software began sending the laser data readings and started NDT payload acquisitions.

Additionally, as the computer was mounted on the UAV and did not connect to a human interface device (e.g. monitor, mouse), Secure Shell (SSH) was used, in order to remote access the file folders and execute applications remotely.

2.5 Summary

This chapter reviewed different aerial vehicles, novel designs, and navigation sensors for UAV operation. The development of a UAV platform for remote NDT inspections was presented in this chapter. The platform had the following features:

- The platform was modified from an AscTec commercial UAV, which is reliable and robust for NDT inspections.
- The firmware running on the UAV onboard microcontroller was modified for two wireless communication channels. The modification increased the wireless bandwidth to provide more accurate controls.
- The software application running on the UAV onboard computer acquired the onboard sensor readings and transmitted the data to the off-board workstation through Wi-Fi.

- The wireless control communications were achieved by two separate XBee modules with a customised protocol. The communication rate was up to 20 Hz.
- The GUI visualised the instantaneous UAV poses, and sensor readings allowed for basic user controls and UAV flight status monitoring.
- The control algorithms for the UAV poses and flight trajectory control were integrated. Details will be discussed in Chapter 3.
- The integration of the Vicon positioning tracking system facilitated UAV navigation and real-time control feedback.

The features listed above were used to build a basic aerial platform. The platform was further developed with positional and flight control to deliver different sensing payloads for NDT inspections, which will be detailed in subsequent chapters.

Chapter 3

UAV Control and Miniature Laser Scanner Implementation

3.1 Introduction

The previous chapter outlined several aerial platforms and detailed the software development required for the AscTec Firefly UAV to perform indoor NDT inspections. This chapter focuses on the UAV flight controller scheme and laser-based flight path generation. Various UAV control theories are reviewed in Section 3.2. Section 3.3 describes the controller design for this aerial platform, based on PID (Proportional-Integral-Derivative) control technique. Section 3.4 details the integration of the Hokuyo URG-04LX [109] miniature laser scanner into the platform. Section 3.5 presents a path planning method, which utilises the laser scanner outputs to generate adaptive flight paths based on the sensor outputs. The laser scanner performance and UAV positional accuracies are evaluated in Section 3.6.

While conducting the inspection measurements, the UAV was guided to follow a flight trajectory composed of multiple discrete waypoints. Conventionally,

flight trajectories are planned before inspection, based on the CAD model of the target. Such trajectories typically require a proper standoff redundancy to avoid collisions, and thereby cannot offer close-range (standoff distance < 1 metre), detailed inspection. Additionally, inspections of ageing infrastructures cannot provide accurate CAD models to plan the flight trajectory in advance. To evaluate assets with unknown and complex geometry and enhance inspection accuracy, a miniature laser scanner was mounted on the top of the UAV. It measured the standoff distance to the target object, as well as its alignment offset versus the target's surface normal vector. The laser scanner was integrated into the flight controller. The controller updated the flight trajectory every 100 ms based on the laser scanner sample rate [109] using the instantaneous sensor readings. Typical of miniature and low-power laser scanners, some measurement errors occurred in the raw sensor outputs. These errors impacted the accuracy of distance measurements, which accumulated in alignment measurements. Thus, a curve fitting procedure, a typical strategy to extract the line features from the laser data [63], was applied to the raw data to further improve measurement accuracy, which is detailed in Section 3.4.3. The accuracies of the distance and alignment measurements were significantly improved. The error reduced from 2.77 mm to 1.20 mm on the distance measurements and reduced from 4.68° to 0.32° on the alignment measurements, as detailed in Section 3.6.1.

3.2 UAV Control Theories

As described in Chapter 2, the AscTec Firefly is a ready-to-fly UAV with two onboard microcontrollers for outdoor navigation. However, these two controllers were not suitable for laboratory-based experiments, because GPS signals were unavailable. Thus, a customised controller was required. The SDK (Software Development Kit) provided by the AscTec [22] offered primary communication to

the UAV onboard microcontrollers, which was crucial to the implementation of an autonomous UAV control [22].

A UAV is a six Degree Of Freedom (DoF) system, containing three translations $(x,\ y,\ z)$ and three orientations (pitch θ, roll ϕ, yaw ψ) [19]. Movement is facilitated by adjusting the motors' speeds, such that different thrust force combinations produce various actions. Translations and orientations are dependent in such vehicles. Forward acceleration is produced by rotating the aircraft's pitch angle, resulting in movements in the x-direction, as shown in Figure 3.1(a). Adjusting the roll angle generates lateral acceleration (Figure 3.1(b)), which will facilitate movement in the y-direction. Changing motor speed leads to altitude alterations, as shown in Figure 3.1(c). The yaw angle, or UAV facing direction, is adjusted by the differential motor thrusts, as shown in Figure 3.1(d).

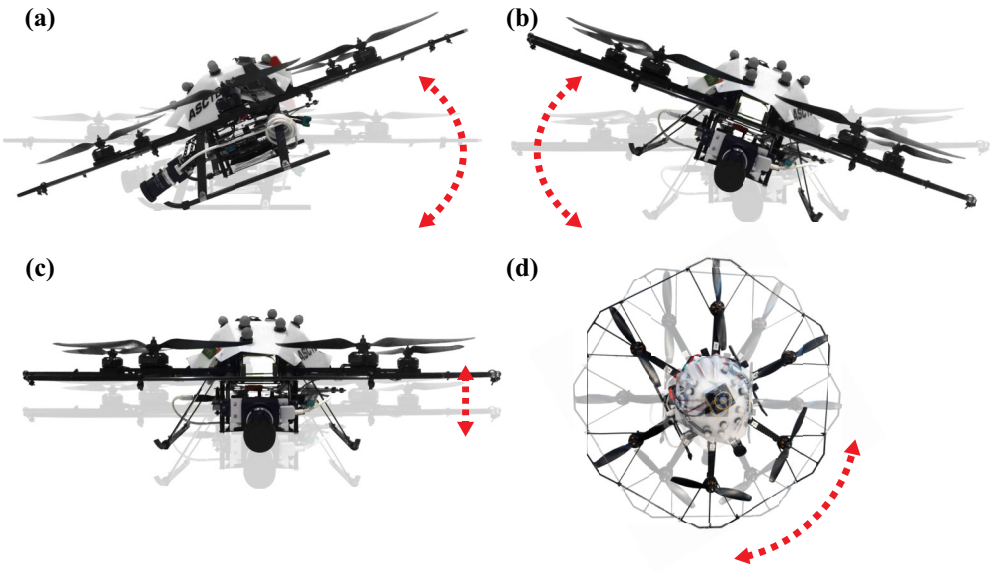

Figure 3.1: AscTec Firefly kinematics: (a) pitch (b) roll (c) altitude (d) yaw

To manipulate the UAV to move without manual intervention, the aircraft must be guided by an autonomous controller. Numerous existing state-of-art controller designs can stabilise the UAV in different conditions. Several control techniques, including PID, Linear Quadratic Regulator, backstepping, and sliding mode have been demonstrated by previous studies [110].

3.2.1 Proportional Integral Derivative Control

Introduced by Minorsky in 1922 [111], a PID-based controller is a closed-loop feedback system, continuously calculating the error ($e(t)$) between the instantaneous measurement and the desired value, defined as:

$$e(t) = X_d - X \tag{3.1}$$

where X_d is the desired positional vector, and X is the actual positional vector measured by the sensor.

The output of the controller ($u(t)$) is the sum of three terms (proportional, integral and derivative of the error), given by:

$$u(t) = k_p \times e(t) + k_i \times \int e(t)dt + k_d \times \frac{d}{dt}e(t) \tag{3.2}$$

where k_p, k_i, and k_d denote the weights applied to each term. The P term represents the instantaneous error between the actual measurement and the desired setpoint. The I term is the sum of the error from the starting time (t_0), which is used to analyse the past error. The D term is the changing rate of the error, for future error predications [112]. Figure 3.2 is a general schematic diagram of a UAV control system utilising the PID technique.

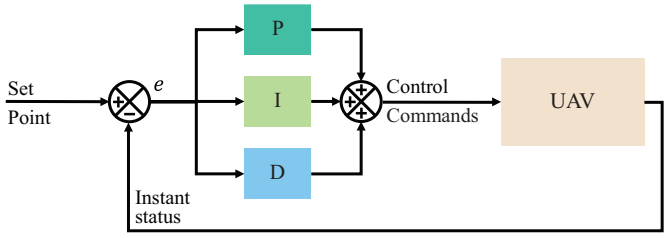

Figure 3.2: General schematic diagram of a PID-based UAV control system

Based on the UAV kinematics, the UAV control of six DoFs are dependent. The pitch angle controls the velocity along the UAV's x-body, while the velocity of UAV's y-axis is dictated by the roll angle. Therefore, the structure of the UAV

controller can be a three-loop cascaded model,as shown in Figure 3.3. Each loop can be a PID controller. The first loop is a position controller, which feeds the positional velocity loop. The output of the positional velocity loop creates the desired orientation for the attitude controller.

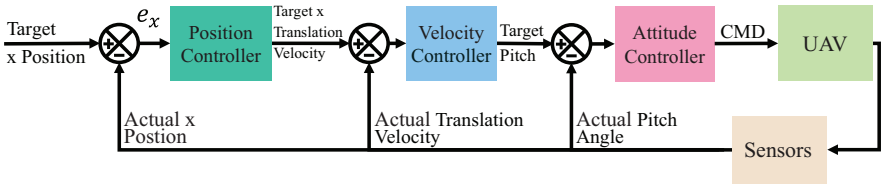

Figure 3.3: An example of the three-layer position PID control system

The controls of the yaw and the altitude are different. During slow manoeuvrings, the pitch and roll are expected to be small, so their influences on the yaw and altitude are negligible. Hence, the UAV six DoFs can be controlled by eight controllers. These are:

$$
\begin{aligned}
\dot{x}_d &= k_{px} \times e_x + k_{ix} \times \int e_x dt + k_{dx} \times \frac{d}{dt} e_x \\
\theta_d &= k_{p\dot{x}} \times e_{\dot{x}} + k_{i\dot{x}} \times \int e_{\dot{x}} dt + k_{d\dot{x}} \times \frac{d}{dt} e_{\dot{x}} \\
u_\theta &= k_{p\theta} \times e_\theta + k_{i\theta} \times \int e_\theta dt + k_{d\theta} \times \frac{d}{dt} e_\theta \\
\dot{y}_d &= k_{py} \times e_y + k_{iy} \times \int e_y dt + k_{dy} \times \frac{d}{dt} e_y \\
\phi_d &= k_{p\dot{y}} \times e_{\dot{y}} + k_{i\dot{y}} \times \int e_{\dot{y}} dt + k_{d\dot{y}} \times \frac{d}{dt} e_{\dot{y}} \\
u_\phi &= k_{p\phi} \times e_\phi + k_{i\phi} \times \int e_\phi dt + k_{d\phi} \times \frac{d}{dt} e_\phi \\
u_z &= k_{pz} \times e_z + k_{iz} \times \int e_z dt + k_{dz} \times \frac{d}{dt} e_z \\
u_\psi &= k_{p\psi} \times e_\psi + k_{i\psi} \times \int e_\psi dt + k_{d\psi} \times \frac{d}{dt} e_\psi
\end{aligned}
\tag{3.3}
$$

where the controller outputs $\dot{x}_d$, θ_d, $\dot{y}_d$ and ϕ_d are desired setpoints of the positional velocities and attitudes controller. u_θ, u_ϕ, u_z and u_ψ are the commands to the

UAV system. The controller inputs are the measured errors, determined by:

$$\begin{aligned} e_x(t) &= x_d - x \\ e_{\dot{x}}(t) &= \dot{x}_d - \dot{x} \\ e_\theta(t) &= \theta_d - \theta \\ e_y(t) &= y_d - y \\ e_{\dot{y}}(t) &= \dot{y}_d - \dot{y} \\ e_\phi(t) &= \phi_d - \phi \\ e_z(t) &= z_d - z \\ e_\psi(t) &= \psi_d - \psi \end{aligned} \tag{3.4}$$

where x_d, y_d, z_d, θ_d, ϕ_d and ψ_d are the desired setpoints of the $(x,\ y,\ z)$ position and pitch, roll, and yaw orientations, respectively. x, y, z, θ, ϕ and ψ are the aircraft's instantaneous positions and orientations. $\dot{x}_d$, $\dot{y}_d$, $\dot{x}$ and $\dot{y}$ are the desired velocities along the UAV's x- and y-axis and the cosponsoring instantaneous velocities.

Bouabdallah et al. demonstrated UAV height control using a one-layer positional controller, which was implemented in the x and y-directions using a positional controller and an attitude controller [19]. Similarly, Hoffmann et al. applied PID controllers to tune the motor speeds for a UAV's attitude and positional control [113].

Liu et al. implemented a PD controller with a compensator to reduce UAV positional errors [114]. The robust compensator was designed to restrain the influences of uncertainties, provide more robustness to compensate environmental disturbances, such as wind gusts.

k_p, k_i and k_d in Eq. (3.3) are the parameters of each PID term, which dictate the controller's performance [112]. These values must be fine-tuned to optimise performance. The theory of fuzzy set, or fuzzy logic, was introduced by Zadeh in

1965 [115]. The fuzzy controller, based on this theory, was implemented into the control system to automatically tune these three PID parameters. The controller graded the control performance, using several logic states under fuzzy rules. These graded states were used to tune the parameters and achieve the best performance [116]. Fuzzy controller theory has been implemented onto a UAV, in order to tune the controller automatically. Simulations demonstrated positional accuracy was improved by a factor of two on an autonomously-tuned PID controller. The controller was also able to compensate for payload mass variation using online tuning of the controller parameter, whilst a conventional controller crashed after eight seconds [117].

3.2.2 Linear Quadratic Regulator Control

Linear Quadratic Regulator (LQR) is an optimal, state feedback controller based on the state space model. Figure 3.4 shows the system diagram of the LQR feedback system [118].

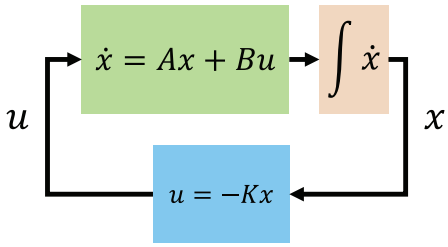

Figure 3.4: Generic schematic diagram of an LQR feedback controller

The state space model of a continuous linear system can be described as:

$$\begin{aligned} \dot{x} &= Ax + Bu \\ x(t_0) &= x_0 \end{aligned} \tag{3.5}$$

where x is the state vector, u is the input vector, A is the state matrix, and B is the input matrix. The state feedback control is given by:

$$u = -Kx \tag{3.6}$$

where K is the feedback matrix, which is a trade-off between the transit response and control effort. Therefore, the optimal approach to design is to minimise the cost function of the system, which is defined by:

$$J = \frac{1}{2}\int_0^{t_0} [x^T(t)Qx(t) + u^T(t)Ru(t)]dt \tag{3.7}$$

where Q and R are the coefficient matrices. Q represents the weight of the transit response and R is the weight of the cost of the control input.

Based on a Hamiltonian function and Hamilton-Jacobi-Bellman equations, the cost function can be calculated from the numerical solution of [119]:

$$K = R^{-1}B^T P \tag{3.8}$$

where P is found by solving the Riccati differential equation [119]:

$$Q + A^T P + PA - PBR^{-1}B^T P = 0 \tag{3.9}$$

Therefore, the feedback control can be designed as:

$$u = -R^{-1}B^T Px \tag{3.10}$$

The following numerical example, which has been adapted from [120], is the controller design for the UAV movements along the x-axis.

The simplified, state space model can be represented as:

$$\begin{bmatrix} \dot{x} \\ \ddot{x} \end{bmatrix} = \begin{bmatrix} 0 & 1 \\ 0 & 0 \end{bmatrix} \begin{bmatrix} x \\ \dot{x} \end{bmatrix} + \begin{bmatrix} 0 \\ -g \end{bmatrix} u \tag{3.11}$$

where g is the gravitational acceleration (9.8) and u represents pitch angle input for the UAV movements on the x-axis.

Therefore, the state matrix and the input matrix in Eq. (3.5) can be represented by:

$$A = \begin{bmatrix} 0 & 1 \\ 0 & 0 \end{bmatrix}, \; B = \begin{bmatrix} 0 \\ -g \end{bmatrix} \tag{3.12}$$

Assume the weights of transit response and the control effort are the same.

$$Q = \begin{bmatrix} 1 & 0 \\ 0 & 1 \end{bmatrix}, \; R = 1 \tag{3.13}$$

The optimised feedback matrix K is $\begin{bmatrix} -10 & -1.7438 \end{bmatrix}$, calculated by the MATLAB function *lqr* (based on theory described in Eq. (3.8) and Eq. (3.9)). Since the first element of B in Eq. (3.12) is zero, the value of first element of K is independent to the performance of the system described in Eq. (3.11).

Conventional PID controllers have an input saturation constraint, which influences flight stability, including possible sudden mass changes during the flight [121]. Utilising the LQR design rules, Kahveci et al. successfully addressed the aerodynamic challenges [122]. [123] presented an LQR controller with a Kalman filter for UAV altitude control to improve controller efficiency and better estimate disturbances. Bouabdallah et al. implemented and evaluated an LQR-based controller and a PID controller [19]. The performance of the two controllers was determined using UAV dynamic model simulations and real experimental flights. The real flights showed that the classic PID controller performed slightly better, due to model imperfections. Another comparison presented in [124] characterised

the performance of an LQR controller, a PID controller, and an LQR tuned PID controller. The LQR tuned PID controller was inferior. Similar comparisons were conducted in [125]. The LQR controller had smaller steady-state errors and a faster response, while the PID controller had better stability.

3.2.3 Backstepping Control

Backstepping is a control technique used to asymptotically stabilise the non-linear system, as introduced by Kokotovic in 1992 [126]. A nonlinear system is a strict-feedback form. The controller design progress is a recursive method, which starts from the stabilised subsystem and designs another controller to stabilise its outer layers until all layers have been covered. The system strict-feedback form can be described as:

$$\begin{aligned}
\dot{x} &= f_x(x) + g_x(x)z_1 \\
\dot{z_1} &= f_1(x, z_1) + g_1(x, z_1)z_2 \\
\dot{z_2} &= f_2(x, z_1, z_2) + g_2(x, z_1, z_2)z_3 \\
&\vdots \\
\dot{z_{k-1}} &= f_{k-1}(x, z_1, \ldots, z_{k-1}) + g_{k-1}(x, z_1, \ldots, z_{k-1})z_k \\
\dot{z_k} &= f_k(x, z_1, \ldots, z_k) + g_k(x, z_1, \ldots, z_k)u
\end{aligned} \tag{3.14}$$

where u is the control input, $z_1, \ldots,\ z_k$ are the virtual states, $f_x,\ f_1, \ldots,\ f_k$ vanish at the origin, and g_k is non-zero. The system design is approached based on the Lyapunov theorem [127].

To design the simplified backstepping controller for movements along the x-axis, as described in the previous section, the kinematic model (Eq. (3.11)) can be rewritten as:

$$\ddot{x} = -g \times u \tag{3.15}$$

The first virtual state is the velocity on the x-axis, given by:

$$z_1 = x - \ x_d \tag{3.16}$$

The second virtual state represents the error between the actual control ($\dot{z_1}$) and virtual control (α), defined as:

$$z_2 = \dot{x} - \ \dot{x_d} - \alpha \tag{3.17}$$

The first Lyapunov function can be presented as:

$$V_1 = \frac{1}{2}{z_1}^2 \tag{3.18}$$

To achieve the first virtual stable system, the derivative form of the Lyapunov function V_1 must be negative, when z_2 approaches zero. This is achieved by:

$$\begin{aligned} &\alpha = -k_1 \times z_1 \\ &\dot{V_1} = z_1\dot{z_1} = z_1(z_2 + \alpha) = -k_1 \times {z_1}^2 + z_1 z_2 \end{aligned} \tag{3.19}$$

where k_1 is a tuning parameter used to determine the controller's performance.

Thus:

$$\dot{z_2} = -g \times u - \ \ddot{x_d} + k_1 \times \dot{z_1} \tag{3.20}$$

The second Lyapunov function is presented as:

$$V_2 = \dot{V_1} + \frac{1}{2}{z_2}^2 \tag{3.21}$$

To achieve the second virtual system stable:

$$\begin{aligned} \dot{V_2} &= z_1\dot{z_1} + z_2\dot{z_2} < 0 \\ &= -k_1 \times {z_1}^2 + z_2\left(z_1 + \dot{z_2}\right) \\ &= -k_1 \times {z_1}^2 + z_2(z_1 - g \times u - \ \ddot{x_d} + k_1 \times \dot{z_1}) \end{aligned} \tag{3.22}$$

Thus, the actual control input is:

$$u = \frac{1}{g}(k_2 \times z_2 + k_1 \times \dot{z_1} + z_1) - \ \ddot{x_d} \tag{3.23}$$

In this case, the derivative form of the second Lyapunov function becomes:

$$\dot{V_2} = -k_1 \times {z_1}^2 - k_2 \times {z_2}^2 < 0 \tag{3.24}$$

where k_2 is the second parameter to be optimised for system performance.

Authors in [128–131] described UAVs equipped with backstepping controllers, which were more robust and stable than conventional PID controllers in the presence of uncertainties (e.g. windy conditions and reaction forces). Bouabdallah et al. implemented a backstepping controller on a UAV, based on the Lyapunov theorem [128]. The system contained two layers, starting from the error function of the UAV's physical kinematic model. [130] designed an integral backstepping controller, which was a combination of PID theory and a backstepping technique. The controller's integral terms eliminated the impact of the steady-state error. The authors of [131] described a hybrid backstepping controller, based on the Frenet-Serret theory. The controller had lower amplitude and shorter oscillations than a linear PID controller, especially during high-speed manoeuvring.

Uncertainties during the flight, such as payload variation and disturbance, limit the controller's performance and impact its optimisation process. Additionally, backstepping requires full information of all the system states [132]. Moreover, one of the difficulties of this technique is the finding an appropriate Lyapunov candidate [132]. Authors in [133, 134] designed backstepping controllers to stabilise the UAV and control its attitude. The adaptive controller decreased the negative impacts of mass variation and aerodynamic challenges, offering more robustness.

3.2.4 Sliding Mode Control

Sliding mode control, first presented in 1977, is a control technology using the control signal to switch between two distinctively different system structures, by "sliding" on a sliding surface ($s(t) = 0$) [135]. Systems with the sliding mode controller are more robust to disturbances and decrease the impact of uncertainties. The system stabilities are approached by the Lyapunov theorem, while $s(t)\dot{s(t)} < 0$.

The following example demonstrates the procedure when designing a sliding mode approach to movement along the x-axis.

The model in Eq. (3.11) can be presented as:

$$\ddot{x(t)} = -g \times u(t) \tag{3.25}$$

where $x(t)$ is the x-axis position and $u(t)$ is the pitch angle control input. The sliding mode surface is designated as [136]:

$$s(t) = c \times e(t) + \dot{e(t)} \tag{3.26}$$

where c is a positive coefficient parameter, representing the trade-off between performance and robustness. $e(t)$ and $\dot{e(t)}$ are the positional error and its derivative, defined as:

$$\begin{aligned} e(t) &= x(t) \ - \ x_d(t) \\ \dot{e(t)} &= \dot{x(t)} \ - \ \dot{x_d(t)} \end{aligned} \tag{3.27}$$

where $x_d(t)$ is the desired setpoint.

From the definition of a sliding surface, if $s(t) = 0, c \times e(t) + \dot{e(t)} = 0$, and $e(t) = e(0) \times exp(-c \times t)$. Therefore, with an increment of time, the positional

error will tend to zero exponentially with the decay rate c [136].

$$\begin{aligned} s\dot{(t)} &= c \times e\dot{(t)} + e\ddot{(t)} = c \times e\dot{(t)} \ + \ x\ddot{(t)} \ - \ x_d\ddot{(t)} \\ &= c \times e\dot{(t)} - g \times u\,(t) - x_d\ddot{(t)} \end{aligned} \tag{3.28}$$

To satisfy the approaching and sliding condition, $s\,(t)\,s\dot{(t)} < -\eta\,|s(t)|\,, \quad \eta > 0, \quad s(t) \neq 0,$

$$u(t) = \frac{1}{g}(c \times e\dot{(t)} - \ x_d\ddot{(t)}) - (s(t) + \eta sign(s(t))) \tag{3.29}$$

Thus:

$$s(t)s\dot{(t)} = -s(t)^2 - \eta\,|s(t)| < -\eta\,|s(t)| \tag{3.30}$$

where η are the parameter to be tuned. $\eta sign(s(t))$ is a sign function, which is used to overcome disturbances. Increasing the value of η can increase system reaction speed. Large value of η can cause chattering of the control input [136].

Xu et al. designed a sliding mode controller along with a rate-bounded PID controller to position the UAV in a desired three-dimensional position with an appropriate face angle [137]. The controller was divided into two subsystems: a fully-actuated and an underactuated subsystem. A PID controller and a sliding mode controller were used for the fully-actuated system to drive the UAV height and yaw angle to the desired setpoints. The underactuated subsystem used a sliding mode controller to maintain pitch and roll angles of zero during the flight. The simulation results demonstrated the capability of the controller to stabilise the UAV with parametric uncertainties. Benallegue proposed a high-order sliding mode observer to stabilise a UAV in the presence of uncertainties from measurement sensors [138]. [139] demonstrated the control of an eight-rotor UAV by using a combination of backstepping and sliding mode techniques with an adaptive radial basis function neural network. The adaptive neural network estimated the uncertainties and disturbances without prior knowledge of the

uncertainty bounds. The system demonstrated the performance and robustness of uncertainty rejection.

The main challenge of the sliding mode control is chattering effect. Sliding mode on the sliding surface represented as a high frequency switching control, resulting the chattering effect, an undesired effect can cause the energy loss, unmodeled dynamics, plant destruction and electromagnetic interference [132]. Authors in [137] presented a continuous approximation of the sign function to avoid such a drawback.

Authors in [140, 141] designed a second-order sliding mode controller for a UAV, which exhibited better performance in attenuating chattering effects. The controller, described in [141], was a combination of integral backstepping and sliding mode technologies used to stabilise the UAV with an external constant and unknown stochastic disturbances. Controller performances and positional accuracies were also quantified for the UAV utilising PID, LQR, integral backstepping, and an integral backstepping sliding mode controller. Simulation results demonstrated that the proposed combination of sliding mode and backstepping had less vibration and higher accuracy than other approaches.

3.3 Flight Controller Design

Nonlinear controllers, such as backstepping and sliding mode controller, are widely presented in the literature. The UAVs built with a nonlinear controller are more robust than those with linear controllers [142]. These nonlinear controllers facilitate stable flight, especially during high speed operations [142]. Linear controllers are easier to implement [110] but difficult to guarantee stability during agile manuavourings [143].

However, a non-linear controller was not necessary for the aerial platform herein. Inspection flight is typically slow manoeuvring around the target object, instead of agile maneuvers, in order for the sensor to capture detailed features. For example, the flight must be slow enough to avoid motion blur during photogrammetric inspections. Wind gusts in the indoor laboratory can be assumed to be zero. Therefore, the pitch and roll angles are approximate to zero. The literature presented the stability performance of a nonlinear controller as similar to the linear controller under such flight conditions [144, 108]. Additionally, from a software perspective, a three-layer (i.e. Vicon, Workstation, and UAV) PID controller was easier to implement [110]. Therefore, classic PID theory was utilised in the aerial platform (shown in Figure 3.5). Due to the UAV kinematics, the positional velocities can be driven by rotating the UAV. Hence, the output of the velocity controller is the desired UAV angles. The pitch angle controls the velocity along the body x-axis, while the roll angle controlling the velocity along the body y-axis.

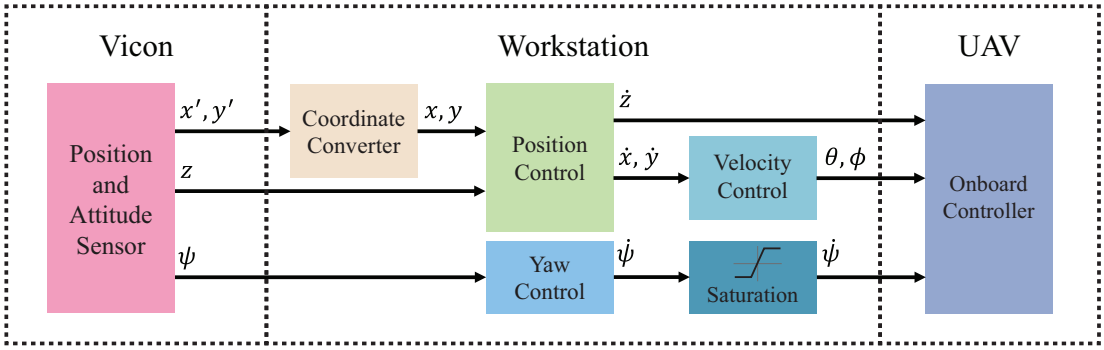

Figure 3.5: High-level architecture of UAV control

Herein, the controller real-time feedback is approached by the Vicon motion capture hardware. The UAV positional velocities were calculated by the differential of the Vicon positional readings with reference to the UAV body coordinates, described in Section 2.3.5. Additionally, in attempting to quantify the flight stability performance of the current hardware, the UAV's full pose was tracked by the Vicon and the positional accuracy relative to the desired point.

To achieve autonomous UAV control, the flight trajectory was planned based on the target geometry and was digitised into a sequence of discrete waypoints. These waypoints were fed into the UAV controller for appropriate control actions. The controller stably guided the UAV approach to a particular waypoint. Once the UAV approached the waypoint, the system assigned the controller setpoint to the next waypoint.

Figure 3.6 shows the high-level diagram of the closed-loop controller. The controller was designed based on the UAV kinematics. A combination of motor thrusts generated attitude angles and vertical lift. Pitch and roll angles were coupled with the forward and lateral accelerations. The lift from the propellers produced acceleration in the vertical direction. When the UAV was hovering, the ideal accelerations and velocities were zero. When the UAV was assigned a new pose, appropriate accelerations and velocities were adjusted and executed by the flight controller. Herein, the controller was adapted from Eq. (3.3), except the pitch and roll angular velocity controls as these have been implemented by AscTec on the UAV's low-level controller.

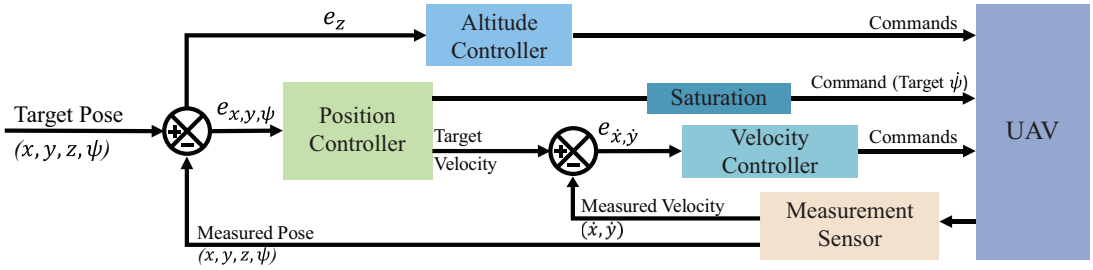

Figure 3.6: High-level diagram of the UAV position and attitude control system

The PID controller uses the feedback system to continuously calculate the error between the immediate measured value and the desired setpoint. The output of the controller is generated by the combination of the scale (P term), the integration (I term), and the changing rate (D term) of the error. The system performance, coupled with the craft's stability, is affected by these three terms, which can be tuned by altering k_p, k_i and k_d. Herein, these gains were tuned utilising the

trial and error method, which use the actual UAV flight performance to adjust these gains. The tuned gains of controllers used for photogrammetric inspections (detailed in Chapter 4) and for ultrasonic inspections (detailed in Chapter 5) are listed in Table 3.1. It is worth to note that the controller gains can also be tuned based on the flight performance in the simulator [145].

Table 3.1: PID controller gains used in photogrammetric inspections and Ultrasonic inspections

	Photogrammetric			**Ultrasonic**		
	k_p	k_i	k_d	k_p	k_i	k_d
x position	1.3	0	0.3	1.3	0	0.3
x velocity	1	0.005	0.1	0.5	0.0015	0.05
y position	1.3	0	0.3	1	0	0.3
y velocity	1	0.002	0.1	0.6	0.005	0.05
z position (Height Mode)	7	0	1.1	6	0	1
z position (Thrust Mode)	1	0.001	0.2	0.75	0.004	0.24
Yaw angle	40	0.002	0	40	0 0.05	0

The control system included two subsystems, where x, y and ψ (yaw) were implemented using three independent cascade multi-layer controllers. A parallel PID controller was utilised to control the UAV's vertical altitude. The controller of x, y and ψ (yaw) was composed of two cascaded PID loops. The PID controller in the first loop calculated the desired velocities for the second layer controller from the error between measurement and target poses. The velocity errors were the input of the second loop, and the second loop's output was the attitude commands for the UAV onboard controller. Because the UAV 6 DOF are dependant, the positional velocities can be controlled by adjusting the UAV attitude angles. The speed control of the yaw angle was implemented on the AscTec onboard controller. Therefore, the second loop in the yaw angle controller was used as saturation block to bound the yaw angle velocity ($\pm$ 15°/second).

The vertical altitude was implemented by combining two control modes (Height and Thrust). The mode shifting depended on the inspection requirements and flight status. AscTec provided three vertical control modes (GPS, Height, and

Thrust) in the SDK. The GPS mode required the signals from GPS satellites, which could not provide tracking and navigation within the laboratory environment.

The Height mode was based on the vertical velocity measured by the onboard barometer, and was hardcoded into the low-level microcontroller. The barometer measures the pressure and converts them to the altitude, and differential the altitude to obtain the vertical velocity. The setpoint, assigned by the off-board workstation, was the desired vertical velocity. The onboard microcontroller continuously measured the UAV's instantaneous vertical velocity and adjusted the motor speed to approach the desired setpoint. This approach is typically used for outdoor navigation and was not accurate enough for indoor inspections. The control algorithms were tuned by the manufacturer, but could provide more robustness in terms of mass variation. However, altitude drifts were observed during the experiments as a result of the noise from the onboard barometer. Additionally, the UAV controlled in the Height mode was unstable when the payload mass approached the upper limit of the UAV's capability. Therefore, the Thrust mode was utilised to address these challenges in the Height mode controller.

The Thrust mode was a purely user-controlled mode, providing direct access to the motors' thrust control. The control setpoint was the percentage of motor speed used without the involvement of the barometer. The controller tuned the motor speed to reach the desired setpoint. The flexibility and replacing the data from the barometer by the Vicon measured velocities offered more accurate vertical positional control. Control was based on the fundamental UAV kinematics: increasing the motor speed to generate upward acceleration, whereas downward acceleration was produced by reducing thrust. The mass-normalised thrust (T_m), which maintains UAV altitude, represents the intersection point where the thrust cancels out the system gravity, such that the vertical acceleration is zero. Therefore, this value must be well tuned to balance the UAV mass. Thrust tuning is only required when the UAV total mass changes; for instance, when

altering the sensing payload. Inappropriate motor speed and mass disturbances will lead to an unstable UAV, with oscillations, overshooting, and underdamping along the z-axis. Herein, these challenges only happened during the controller tuning stage. When the controller detected the UAV is unstable in z-axis, the control mode will be shifted to the Height mode.

Since the photogrammetric inspection is a non-contact remote evaluation approach, position errors in the z-axis are less likely to cause UAV collisions with the target object during inspections. In contrast, contact-based inspections require higher positional accuracies. The positional accuracies in the Height mode, as presented in Section 3.6, are not sufficient for contact-based inspections. Unstable flight and non-ideal UAV positioning will lead to collisions and measurement errors (detailed in Chapter 5). Additionally, the ultrasonic payload mass approached the UAV's upper limit, resulting in instability with the Height mode controller. Therefore, during ultrasonic inspections, the UAV position along the z-axis was maintained by a hybrid controller based on the Height and Thrust modes.

In the hybrid controller, the Thrust mode was used for slow speed operations, such as maintaining altitude to avoid error from the barometer. The Height mode was used for fast movements, such as take-off and landing. It was also used to prevent unexpected UAV crashes originating from sudden mass variations and inaccurate values of the thrust, T_m. Therefore, when the UAV was unstable in the Thrust mode, identified as oscillating or large overshoots, the vertical control was automatically changed to the Height mode. Figure 3.7 presents the Vicon recorded UAV altitude during the tuning procedure. The UAV was controlled by the Height mode and Thrust mode.

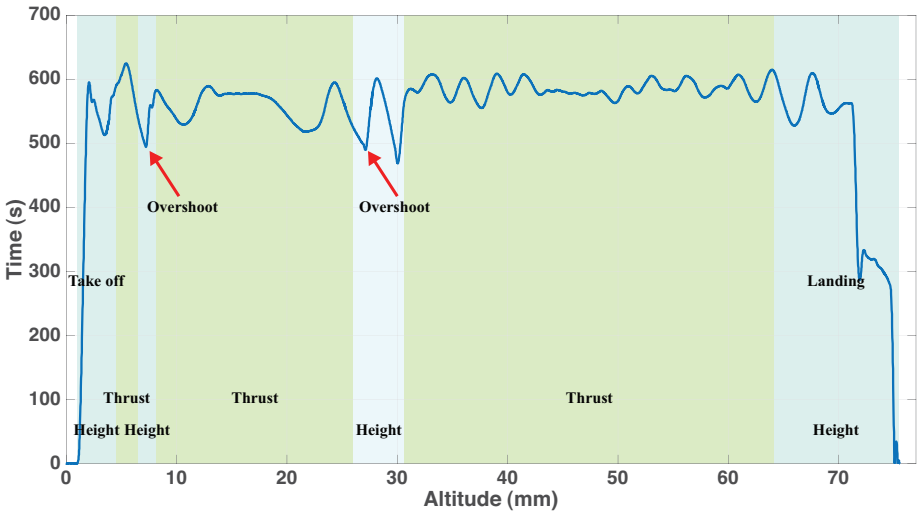

Figure 3.7: UAV altitude with two flight modes during the controller tuning procedure, recorded by the Vicon system

3.4 Implementation of Miniature Laser Scanner

3.4.1 Distance and Alignment Displacement Measurement

To provide an extra geometrical sensing of the target asset, a Hokuyo URG-04LX laser scanner [109] was mounted atop the UAV, whilst its data outputs were integrated into the UAV control loop as a feedback measurement sensor of the aircraft's instant translation and yaw angle.

The UAV onboard laser scanner has been implemented in many research platforms. Kneip et al. have characterised the performance of this scanner [146] and demonstrated its accuracy when measuring the distance to industrial samples [147]. The results disseminated in these publications show the sensor's aptitude for distance measurement during the NDT inspection process and justify its employment here.

The sensor, depicted in Figure 3.8, uses amplitude modulation signals and the phase shift between the transmitted and received signals to calculate the distance to the object [148]. Additionally, to measure the distance of more than one

scanning cycle period, the sensor transmits alternate modulated laser waves. The Hokuyo laser scanner has specifications shown in Table 3.2 [109]. Figure 3.9 shows an example of the laser scanner output when the object was located 760 mm away.

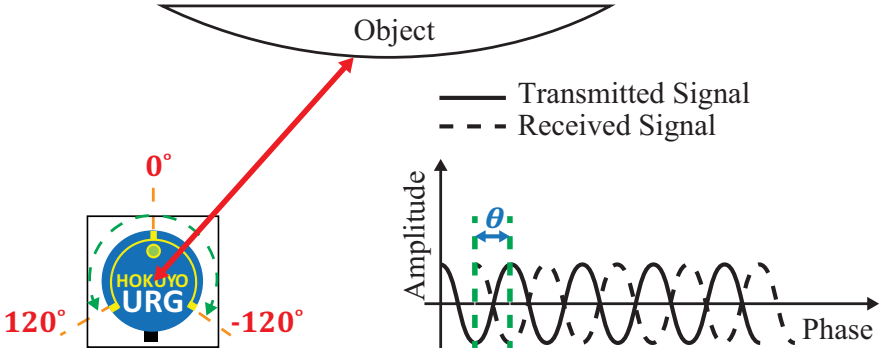

Figure 3.8: Principle of the HOKUYO URG-04LX laser scanner

Table 3.2: Hokuyo URG-04LX laser scanner specifications

Field of View	240°
Resolution	360/1024°
Scanning Rate	10 Hz
Mass	160 g
Scanning Range	60 mm to 4095 mm
Accuracy	± 10 mm error, d <1000 mm 1 %, d >1000 mm

Data from the laser scanner were processed and integrated into the flight control system on the off-board controller workstation. Wireless communication between the laser scanner and the workstation was established by the customised C++ application running on the UAV onboard computer. The application was a communication bridge, acquiring the measurements from the sensor and wirelessly transmitting the packets to the off-board workstation, as detailed in Chapter 2.

To effectively interpret the integration of the laser scanner and data processing approaches, the wind turbine blade (the target object photogrammetry inspected, described in Chapter 4) is used as an illustrative example. The target object was presumed to always be located in front of the UAV and inside the sensor's field of view. To achieve faster data processing and to shorten the scanner travelling

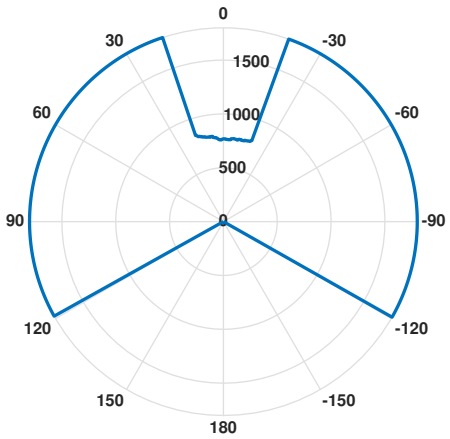

Figure 3.9: An example of the URG-04LX output when the object was placed 760 mm in front of the scanner

distance, the laser scanner sweep range was narrowed to ± 90°. Therefore, the measurement output in a single acquisition cycle was a 512-integer array. Each integer in the array was a distance measurement at the corresponding angle.

When scanning a flat surface, the ideal sensor outputs can be represented as [63]:

$$D_\theta = \frac{D}{\cos(\theta - \theta')} \tag{3.31}$$

where D_θ is the measured distance to the surface at θ. θ' is the rotation with the shortest distance, as shown in Figure 3.10. Herein, when the UAV's x-body is along with the object's surface normal vector, $\theta' = 0°$.

While scanning an non-flat surface with a simple geometry (e.g. circular structure), Eq. (3.31) can be replaced by other mathematical models. For an object with unknown or complex shape, a more generic line extraction algorithm can be applied [149, 63]. The algorithm subdivides the laser scan into multiple segments, fitting a line (Eq. (3.31)) to each segment, and merging these fitted lines to estimate the entire structure.

Herein, the inspections took place in a university laboratory, where the background infrastructure and furniture reflected the infrared lights, leading to spikes in the

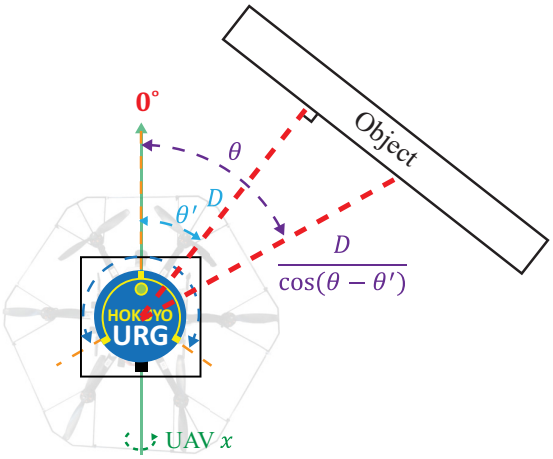

Figure 3.10: A generic representation of the laser scanner reading with θ' alignment angle offset, adapted from [63]

measurements, as shown in Figure 3.11. Since the distances to the background facilities were measured as over 1800 mm, the sensor measurements over that threshold were assumed to be background noise and were rejected. It should be noted that the measurand during the inspections was the UAV standoff distance, which is defined as the distance between the UAV edge and the target object. The sensor outputs were the distances from the laser scanner (UAV central) to the target surface. Therefore, the standoff distance was the sensor measurement minus the UAV diameter (330 mm). The UAV standoff distance that the sensor could detect around the wind turbine blade was between 0 and 1470 mm.

The target object was identified in the laser output by assuming the inspection target was always the closest object in the laser field of view. The post-processed measurement represented a set of sensor measurements that was reflected from the target surface. Figure 3.11 is an illustrative example of the laser data output in the laboratory environment. Distances over 1800 mm in this figure were recognised as reflections from the background. The resultant output was a set of distances $\{D_{\theta_{min}} \dots D_{\theta_{max}}\}$, measured from the angle sweep between θ_{min} and θ_{max}. θ_{min} denoted the right edge of the target object and θ_{max} was the reflection from the left edge. The smallest value in the output curve was used as the minimum distance to the inspection object.

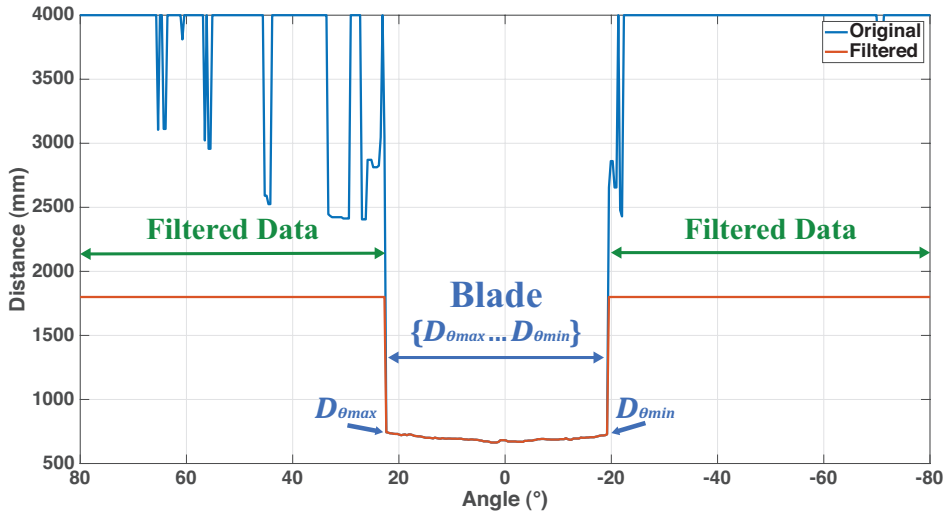

Figure 3.11: An example of the laser data captured in the laboratory with the raw and background removed laser scanner results

3.4.2 Alignment Error Measurement

To conduct a meaningful inspection, NDT sensing payload had to be perpendicular to the target surface normal vector. The laser scanner on the UAV estimated the craft's alignment offset versus the target's surface normal vector, and thus, the flight controller could adjust the UAV horizontal orientation in real-time to minimise the alignment error.

To adequately describe the alignment error estimation procedure, the UAV was simplified as a point. Since the blade surface was smooth and flat, it was presumed to be a 2D vertical plane. The standoff between the UAV and the blade was equal to the distance from the point to its closest point projection on the plane [150]. When the UAV orientation was perpendicular to the blade surface normal vector, the laser scanner centre beam produced the shortest range. The angle that produced the minimum standoff was equivalent to the alignment error between the UAV yaw orientation and the surface normal vector.

3.4.2.1 Simulations of Alignment Error Measurement

To better demonstrate the approach described above, a simulation was performed to mimic real inspection scenarios. A MATLAB script firstly simulated the laser scanner outputs using Eq. (3.31), with different alignment errors $\theta' = 0°, \pm 45°$ and $D = 600$ mm to replicate the inspection scenarios described in Chapter 4. Figure 3.12 presents the diagrams of three simulated scenarios. The simulated laser scanner outputs are plotted in polar graphs (Figure 3.13) and line graphs (Figure 3.14).

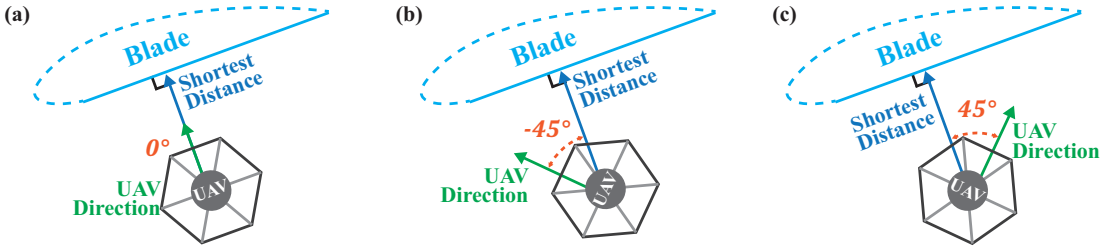

Figure 3.12: Simulated sensor scenarios when (a) UAV was heading to the blade (b) UAV had -45° alignment error (c) UAV had 45° alignment error. The blue arrow is the surface normal vector and the green arrow denotes the UAV yaw angle

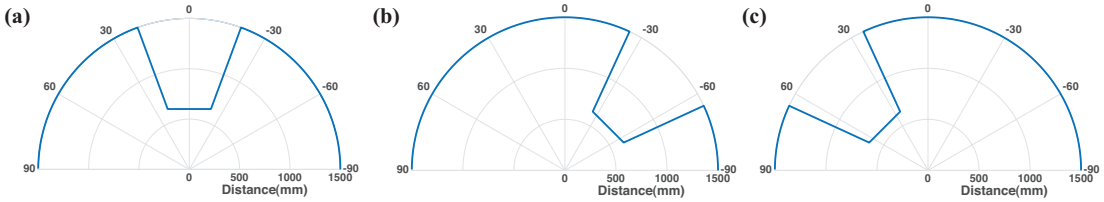

Figure 3.13: Simulated sensor outputs when the UAV had different alignment errors, plotted on polar graphs: (a) 0° (b) -45° (c) 45°

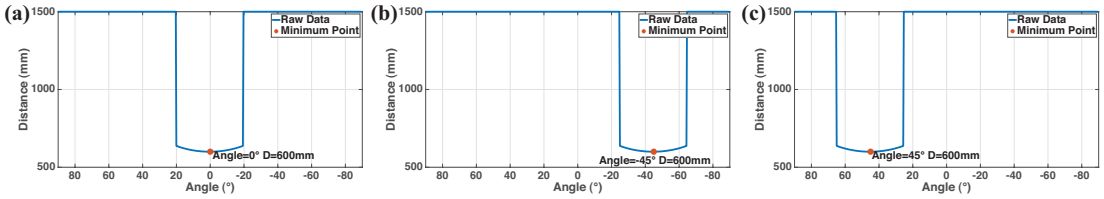

Figure 3.14: Simulated sensor outputs when the UAV had different alignment errors plotted on line graphs: (a) 0° (b) -45° (c) 45°

Then, the alignment errors θ' were calculated based on the strategy described in Section 3.4.2. The estimated alignment errors were labelled in Figure 3.14. The results showed that the alignment errors calculated by MATLAB matched the simulation inputs. This proves the minimum value in a laser data set can be used to as the UAV alignment error.

3.4.2.2 Error Analysis

The alignment error was estimated by utilising the minimum distance in the raw data. The raw sensor data contained $\pm$ 10 mm measurement error (e), which could lead to a large propagated error in the results of the alignment estimation procedure. The maximum value of such propagated errors can be calculated, assuming the raw measurements contained the maximum errors at θ_e and 0°, as shown in Figure 3.15. Presume the value at θ_e ($D_{\theta e}$) is the smallest in the scanner results and its value is the actual distance with the maximum negative error, given by:

$$D_{\theta e} = \frac{D}{\cos(\theta_e)} - e \tag{3.32}$$

where D is the minimum distance to the blade.

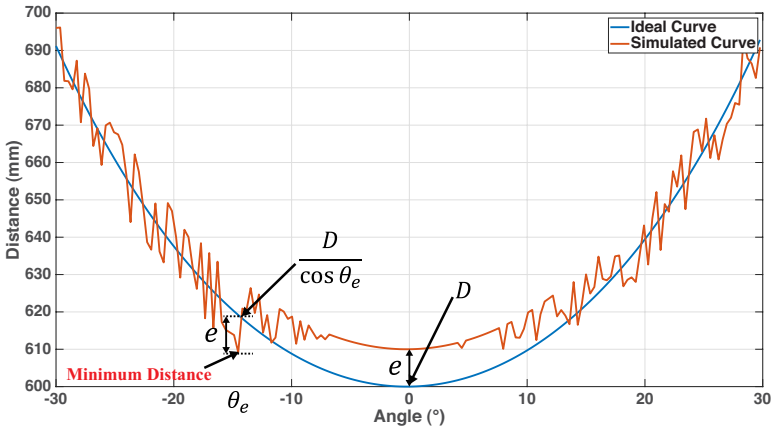

Figure 3.15: The worse case scenario. The true alignment error is 0°, and the estimated angle is θ_e using the sensor raw data.

In addition, the values between $-\theta_e$ and θ_e must be larger than the actual distances. To create the maximum errors in the alignment estimation, the value of $D_{\theta e}$ must be smaller than the maximum possible value at the true alignment offset angle $(D + e)$.

Therefore, the accuracy of alignment measurement is expressed as follows:

$$\begin{aligned} &\frac{D}{\cos(\theta_e)} - e \leq D + e \\ &\theta_e \leq \left|\arccos \frac{D}{D + 2e}\right| \end{aligned} \tag{3.33}$$

Thus, the maximum error of the alignment measurement, depending on the standoff distance, can be calculated by:

$$\begin{aligned} &\theta_e = \arccos \frac{D}{D + 2e} \\ &e = 10 \end{aligned} \tag{3.34}$$

The error is incremented with the shorter standoff distance. When the laser scanner has a 600 mm standoff distance, the error in the alignment measurement using the laser scanner raw data could be 14.59°. The error is increased to 24.61° when the standoff is 200 mm. Such errors can cause the target object to be located outside the camera field of view, especially when inspecting the edges of the blade. Hence, the raw data from the laser scanner were not accurate enough to estimate alignment errors in the NDT inspections.

3.4.3 Laser Curve Fitting

To lessen the uncertainty in the alignment error measurement and to improve the accuracy of distance measurement, a curve fitting procedure was applied to the raw data. The procedure used the measurements from various angles to estimate a smoother curve, which was the best approximation to the raw scanner

output. This resultant curve replaced the raw output for further distance and alignment calculations. Because the blade surface was relatively flat and smooth, the measurement can be simplified as Eq. (3.31), while D is the the minimum distance (D) to the blade.

Since Eq. (3.31) is the mathematical representation of the ideal laser scanner outputs when measuring the side of the wind turbine blade, this equation was selected as the curve fitting model.

The curve fitting procedure was implemented in the controller workstation. As shown in Figure 3.16 the procedure herein is the Least Squares method [63, 143], which tuned two variables, the θ' angle and distance D, in Eq. (3.31) to minimise the average of the squared residuals, defined as:

$$r = \frac{1}{n} \sum_{\theta=\theta_{min}}^{\theta_{max}} \left(D_{\theta(raw)} - D_{\theta(fitting)} \right)^2 \tag{3.35}$$

where n is the number of reflected beams from the object.

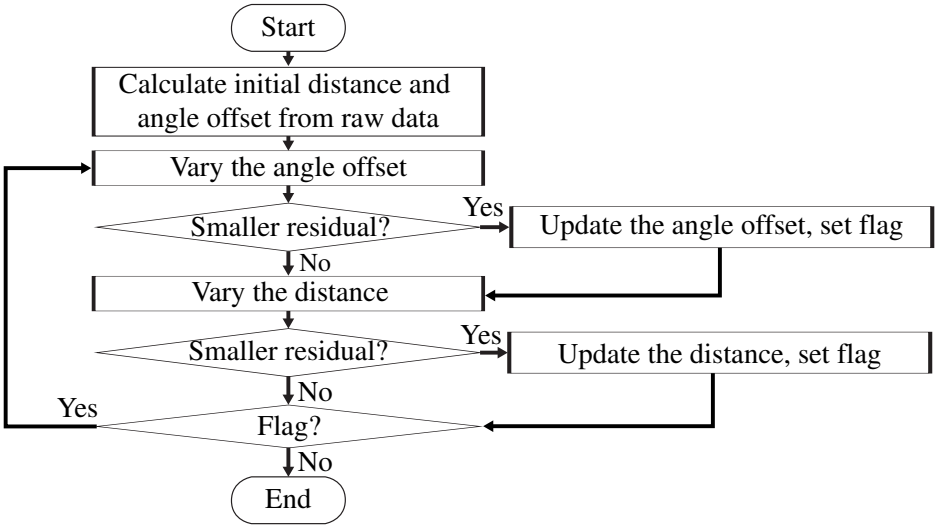

Figure 3.16: Flowchart of the curve fitting

The curve fitting procedure can be described as follows, as shown in Figure 3.16. Initially, the distance D was fixed to the smallest distance in the raw data. The alignment offset θ' was enumerated from θ_{min} to θ_{max}. The angle θ' was updated

when the attempt found a smaller residual sum of squares. The angle θ' was then fixed as the result from the last step, whilst the distance D was enumerated from 90% to 110% of the shortest distance. This range was defined as the measurement accuracy quantified in [147]. The distance was updated when the residual sum of squares had a smaller value. These two steps were repeated with the latest enumeration results until the process could not find a smaller residual sum of squares. Thus, the resultant curve was the best representation with the lowest fitting error.

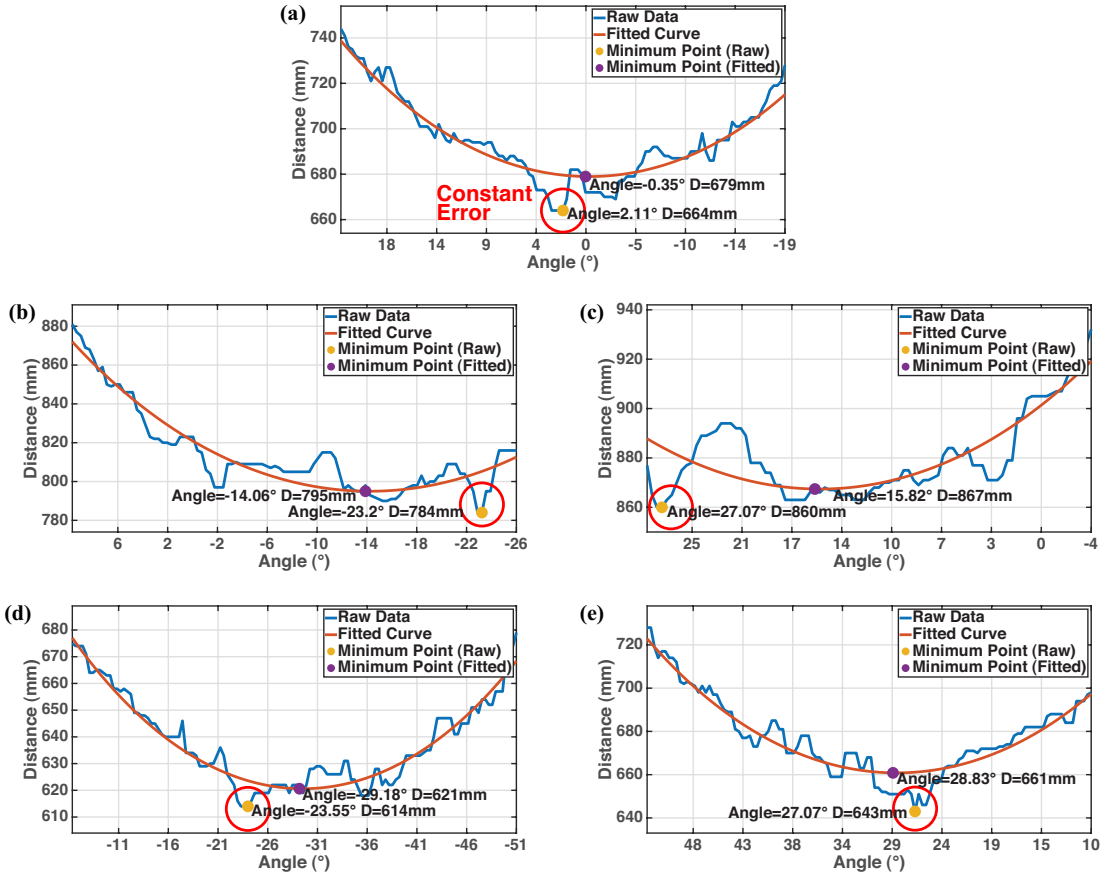

Figure 3.17: Laser scanner raw data, fitted curve, standoffs, and alignment errors estimated from the raw data and fitted curve, when the UAV had the following alignment errors (a) 0° (b) -15° (c) 15° (d) -30° (e) 30°

As demonstrated in Section 3.4.2.2, the alignment error could be larger than 10° when using the raw data. Thus, the curve fitting procedure was implemented to reduce such errors by applying spatial averaging. However, if the resultant

squared residual value (r) in Eq. (3.35) was relatively large (>1000, whilst the values of the Figure 3.17 examples were below 100), curve fitting was insufficient for the specific dataset. To prevent the UAV from rotating unpredictably, the estimated angle in this case would be rejected by the controller, and the UAV is hovering at the current position.

Figure 3.17 presents three laser scanner raw datasets and the corresponding fitted curves when the UAV was positioned with five different alignment errors (0°, ± 15°, ± 30°). The alignment errors were calculated from the raw data and the fitted curves, which are labelled in Figure 3.17. The results highlight the improved accuracy when the fitted curve was utilised to estimate the alignment error.

During the experiments, the laser beams at several specific angles (0° ± 1°, -23° ± 1° and 27° ± 1°) produced relatively large errors, independent of the UAV orientations. These errors were originated from the tiny scratches on the laser optical window, which diffused the laser beam and introduced extra noise. The resultant errors were observed in the alignment estimations using the raw output (Figure 3.17, Figure 3.19 and Table 3.4), and were mitigated by the curve fitting procedure, as shown in Figure 3.17(b)(c).

3.5 Laser Scanner Waypoints Generation

The UAV is required to manoeuvre around the target object to measure the desired locations on the surfaces for a complete NDT inspection. Therefore, flight trajectory and path planning are crucial for meaningful NDT inspections. The trajectory can be generated by a pre-planned path, requiring it to be defined in advance. Such trajectories are less robust, requiring a precise CAD model of the target asset and the object must be placed in the centre of the measurement volume, which is not practical for in-service inspections. Therefore, laser scanner-

based algorithms were developed to generate and adjust the waypoints in real time during airborne inspections.

The onboard laser scanner maps the surroundings and determines the aircraft distance and alignment offset versus the target object in real time. This information is fed into the controller workstation to produce an adaptive flight path. The UAV's position and orientation setpoints are adjusted depending on the measurements of the UAV's instantaneous state. When the position error and alignment error are below 100 mm and 10°, respectively, the UAV is presumed to have reached the desired position, and the setpoint is assigned to the next waypoint. Currently, the inspection section in front of the UAV is simplified as a flat plate, and thereby the subsequent waypoint is assumed to have the same standoff and the same orientation . Thus, the UAV is assigned to 200 mm right with the same orientation for anticlockwise geometry following, once the aircraft is close to the current waypoint. However, such a method requires orientation and yaw alignment adjustments while inspecting a curved surface. An illustrative example of the path planning algorithm using laser data is shown in Figure 3.18.

As shown in Figure 3.18, Point 1 is one of the setpoints in the flight path. After the UAV approached Point 1, the system created a new waypoint, Point 2, at 200 mm to the right by assuming the front section was flat. However, since Point 1 and Point 2 are close to the edge of the blade, the controller must adjust the alignment and standoff. Point 2 was then replaced by Point 2b using the laser measurements at Point 2. Similarly, the UAV was guided through Point 2b to Point 3b. Because the geometry in front of the UAV from Point 3b to Point 5 was close to a flat plate, the alignment and standoff did not need to be adjusted from Point 3b to Point 4. Therefore, the UAV was directly assigned to Point 5 without any pose adjustments.

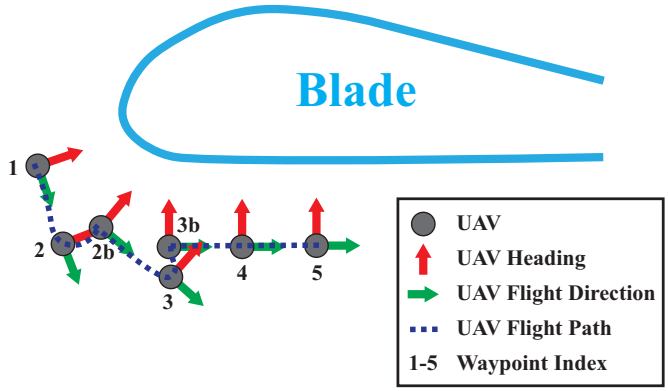

Figure 3.18: An illustrative example of the laser-based waypoints generation on the flight

3.6 Experimental Results

3.6.1 Laser Scanner Performance

To evaluate the performance of the laser scanner and the curve fitting procedure, a series of experiments were undertaken including measurements of the repeatably of the distance and alignment measurements, and the consistency with the Vicon system.

In order to provide a comparison, the pose data was simultaneously tracked by the Vicon system. These tracking data were utilised as the references of the laser scanner. In the experiments described in this section, the UAV with a laser scanner was placed on a 1 m tall table on castors and the position of the table was manually adjusted. Compared with adjusting the UAV poses during the flight, this setup placed the laser scanner more stably granting the experiment repeatability and providing more accurate results. The inspection target utilised in this section was the wind turbine blade.

3.6.1.1 Distance Measurement

The measurand in this experiment was the distance between the scanner and the wind turbine blade. The UAV's x-body, as defined in Figure 2.19, was maintained along with the object's surface normal vector (the alignment error was zero). To quantify the sensor accuracy, the measurements at six nominal values (200, 400, 600, 800, 1000 and 1200 mm) were taken over one minute at each distance. These values covered the range of the UAV indoor NDT application and were selected from the minimum distance with 200 mm increments.

Table 3.3 illustrates the mean absolute errors from the raw laser data and the fitted curve, as compared to the desired standoff distance. The measurement accuracies were significantly enhanced at standoffs between 200 mm and 800 mm by utilising the fitted curve. The mean absolute error was improved by a factor of four between 200 and 600 mm, and the accuracy was enhanced by a factor of two at 800 mm. As shown in Table 3.3, the peak-to-peak errors and the standard deviations calculated from the fitted curve were reduced by a factor of two when the standoff was below 1000 mm. Since the distance increased and the scan area width remained constant, the scanning sweep angle was reduced, causing fewer laser measurements to be used in the curve fitting procedure. Therefore, the errors at larger distances (1000 and 1200 mm) were similar to the raw data output. Although the errors increased at larger distances, the errors from both raw sensor outputs and the fitted curves were measured as below 10%, quantifiably demonstrating the accuracy of the standoff measurement in inspections. Additionally, most of the measurement results were larger than the desired distances, and thus the mean absolute errors were greater than the peak-to-peak errors, as presented in Table 3.3.

Table 3.3: Mean absolute error, peak-to-peak error, and standard deviation of the laser distance measurement from raw data and the fitted curve

Standoff Distance (mm)	**Mean Absolute Error (mm)**		**Peak-to-peak Error (mm)**		**Standard Deviation (mm)**	
	Raw	**Fitted Curve**	**Raw**	**Fitted Curve**	**Raw**	**Fitted Curve**
200	25.38	7.37	19	6	2.77	1.20
400	36.49	1.25	17	9	2.95	1.42
600	47.71	9.96	18	8	2.41	1.19
800	47.39	21.29	18	9	2.66	1.48
1000	52.03	54.57	16	18	2.50	2.96
1200	54.34	53.26	14	20	2.15	2.42

3.6.1.2 Alignment Measurement

Rotating the UAV orientation introduces the alignment error. In this experiment, the UAV with a laser scanner was placed in a constant waypoint, while its orientation (yaw angle) was manually rotated within ± 30°. The measurements at 0°, ± 15°, and ± 30° were repeated over one minute in each orientation to quantify the error of the alignment measurement.

Table 3.4 shows the alignment measurement mean errors, based on the raw data and the fitted curve. The angle estimation from the raw data contained more substantial uncertainties than that of the fitted curve. The values from the raw output had large measurement errors, especially at ± 15° alignment errors (7.47° and 11.66°), while the mean errors from the fitted curve were under 1.61°. Table 3.4 lists the peak-to-peak errors and standard deviations. The results provide evidence showing that the alignment measurements from the fitted curve were more accurate than the values from the raw data.

Table 3.4: Mean absolute error, peak-to-peak error and standard deviation of the laser alignment measurement from raw data and the fitted curve

Vicon Yaw Angle (°)	**Mean Absolute Error (°)**		**Peak-to-peak Error (°)**		**Standard Deviation (°)**	
	Raw	**Fitted Curve**	**Raw**	**Fitted Curve**	**Raw**	**Fitted Curve**
-30	5.84	0.90	16.17	2.11	4.68	0.32
-15	7.47	1.34	11.95	2.11	3.23	0.28
0	2.18	0.60	7.03	3.16	2.04	0.29
15	11.66	0.41	13.48	2.58	0.55	0.30
30	2.66	1.61	4.69	3.05	0.65	0.41

3.6.1.3 Consistency Test

The consistency between the laser scanner and the Vicon system was evaluated by continuously moving the UAV between 400 mm and 1200 mm from the blade surface. The distance from the laser scanner together with the position of the blade surface provided the laser-based positions. These positions, compared with the values from the Vicon, demonstrated the consistency between the measurements from two independent systems. Similarly, the consistency in terms of the alignment measurements was quantified by continuously rotating the UAV within $\pm$ 45° and comparing to the reference yaw angles from the Vicon system.

The experimental results are shown in Figure 3.19. Figure 3.19(a)(b) are the distance consistencies from the raw laser output and the fitted curve, respectively. Figure 3.19(c)(d) are the alignment consistencies from the raw laser output and the fitted curve, respectively. The distance consistencies from the raw data and fitted curve were similar, except for the spike that appeared around 600 mm, causing a 200 mm measurement error. The spike was originated from the scratches on the optical window. Figure 3.19(c) illustrates that the alignment measurement from the raw data was generally fit to the Vicon measurements, but it had poor output resolution and contained large uncertainties. Such errors originated from the constant laser errors at specific beam angles, as described in Section 3.4.3.

In contrast, the yaw angle measured from the fitted curve, as in Figure 3.19(d), linearly fit to the Vicon output and contained less error and higher resolution.

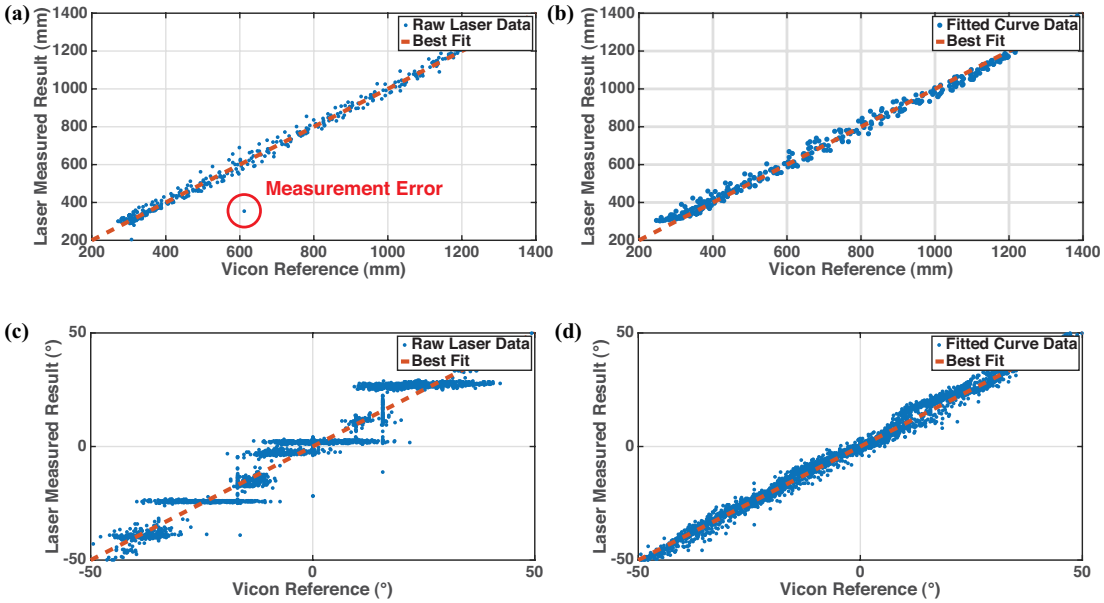

Figure 3.19: Consistency of (a) distance measurement from raw laser output, (b) distance measurement from fitted curve, (c) alignment measurement from raw laser output, (d) alignment measurement from the fitted curve

From the results above, the standoff and alignment offset calculated from fitted curves had more accurate outputs and better resolution, when compared to the results from the raw data. The implementation of the curve fitting procedure offered more precise and stable measurements on alignment and displacement, which allowed the UAV to follow the asset's geometry more precisely. Thus, the inspection payload could be positioned perpendicular to the object's surface normal vector for meaningful NDT applications.

3.6.2 Hovering Stability

The hovering stability represents the accuracy of the UAV maintaining a pose. This experiment was thus designed to quantify the performance of the current system's hovering stability. The first evaluation was undertaken in the absence of

the laser scanner, which had the potential to introduce uncertainties along the x-axis and to further destabilise the craft in the horizontal plane. The UAV was closed-loop controlled based on the Vicon measurements. The Vicon tracking system recorded the position errors along the x-, y- and z-axis of the UAV body frame (as shown in Figure 2.19) when the UAV was hovering for over one minute. The UAV was equipped with a camera, as described in Chapter 4. The horizontal setpoint was the UAV take-off position, which was the centre of the measurement volume where the craft experienced free flight. The desired height was selected as 500 mm above the ground. The UAV altitude was maintained by the Height mode controller. The errors are plotted in Figure 3.20 and listed in Table 3.5.

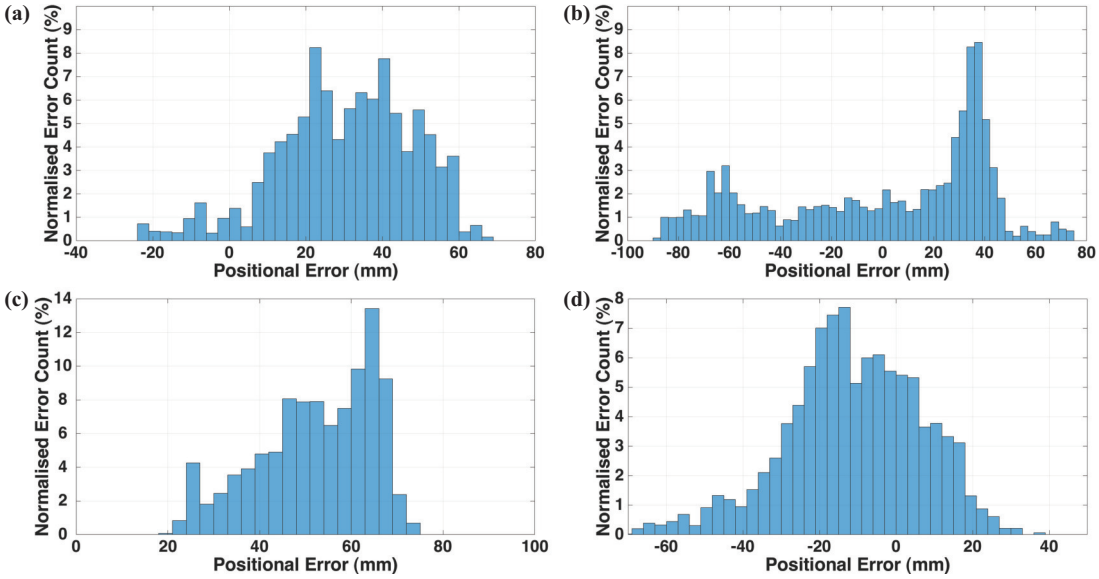

Figure 3.20: Histograms of UAV translation errors during the hovering stability test: (a) y-axis in free flight (b) z-axis in free flight (c) x-axis in free flight (d) x-axis with laser scanner

Table 3.5: Mean error and standard deviation of the UAV translations during the hovering stability test

	x-axis	**y-axis**	**z-axis**
Mean Absolute Error (mm)	52.30	31.57	36.67
Standard Deviation (mm)	12.45	17.68	41.93
Median (mm)	53.78	31.51	14.64
Interquartile Range (mm)	18.83	23.36	71.27

The stability and the standoff error of the UAV with the laser scanner during hovering is critical for NDT inspections and ongoing research. Compared with the Vicon system, the laser scanner had a larger measurement error. Thus, using the laser as the feedback control sensor might cause instability in the x-axis. A second experiment was then designed to quantify the mean error and standard deviation of the height and distance when the UAV maintained a designated distance using the laser scanner. The desired standoff distance was 600 mm from the side of the wind turbine blade, which mimicked the inspections described in Chapter 4. The experimental results are shown in Figure 3.20(d). The mean absolute error and standard deviation of the standoff distance were 19.46 and 16.16 mm, respectively.

The UAV hovering with the laser scanner and in free flight had similar positional errors and standard deviations, which illustrates that the presence of the laser scanner did not destabilise the UAV in the x-direction. The results presented in Figure 3.20(d) show that the UAV was successfully maintained the standoff distance within the ± 60 mm error range using the data from the laser scanner. As shown in the results from both experiments, the UAV experienced large drifts between ± 100 mm along the z-axis and the errors along this axis were nearly double those along the x- and y-axis. Such instabilities in the z-axis originated from the barometer, as mentioned in Section 3.3. The positional errors on the x-axis were not distributed around 0 mm, which is the result of the UAV unbalancing. Since the battery was not ideally placed in the centre of the UAV, a small force was introduced leading to an error offset that appeared in the x-axis.

3.6.3 Trajectory Accuracy

This experiment characterised and ascertained the dynamic performance of the UAV when manoeuvring around a blade and maintaining a constant distance using a laser scanner. The UAV conducted a photogrammetric inspection of the wind turbine blade and maintained the standoff distance as 600 mm (the camera's

focal point), as shown in Figure 3.21. The details and the NDT inspection results will be discussed in Chapter 4.

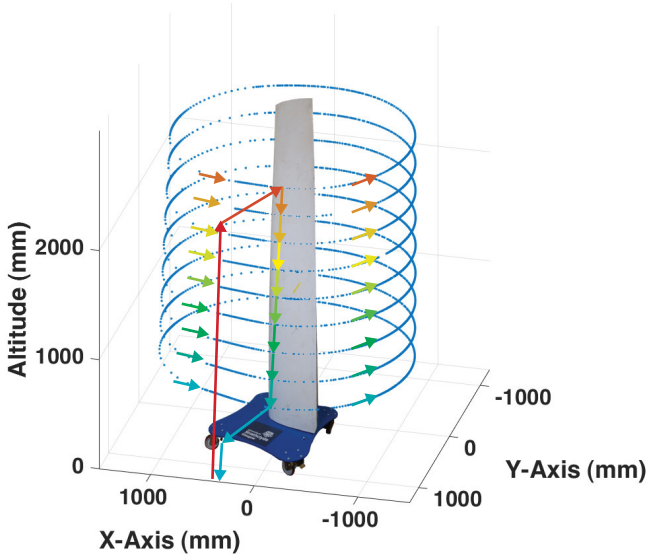

Figure 3.21: UAV flight path used for trajectory accuracy testing

The first experiment was undertaken while the UAV was guided by the hybrid mode controller. The positional accuracy during the entire inspection scheme is shown in Figure 3.22. In comparison, the experiment was repeated with the Height controller maintaining UAV altitude. The altitude errors, as the UAV altitude was maintained by the Height mode controller and the hybrid mode controller, are plotted in Figure 3.23. A dramatic improvement in height errors occurred when utilising the hybrid mode. The mean error and the standard deviation in the z-direction were below 15 mm, which was reduced by a factor of three.

Compared with the distance maintaining experiment results in Section 3.6.2, the standard deviations of the standoff error for both height and hybrid controllers increased from 16.16 mm to 24.55 mm. As shown in Figure 3.22, the distance errors grew from the side of the blade and reached a maximum at the edges, then decreasing until the UAV was near the other side of the blade. The errors in these areas were related to the uncertainties between two flight waypoints. The UAV was adjusting the standoff and orientation while undertaking the inspections. In

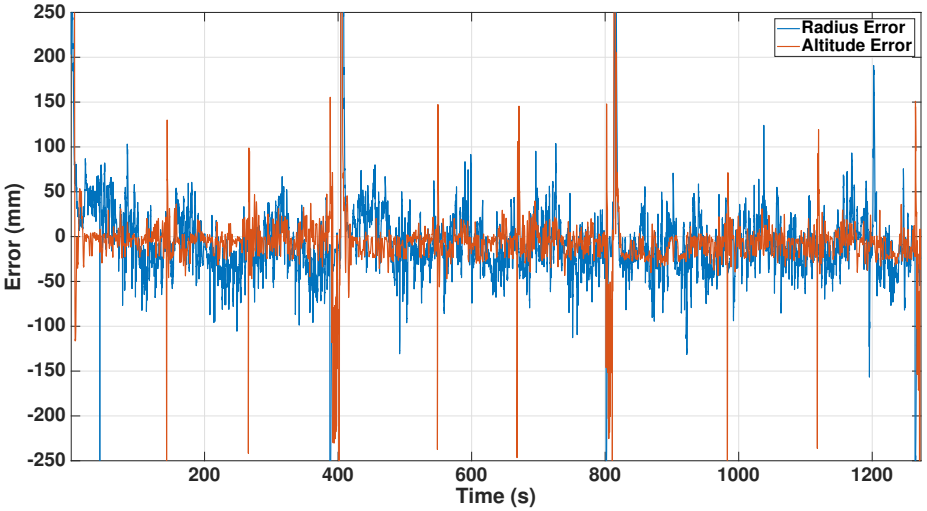

Figure 3.22: UAV distance and altitude errors with the hybrid controller while the laser maintained the standoff

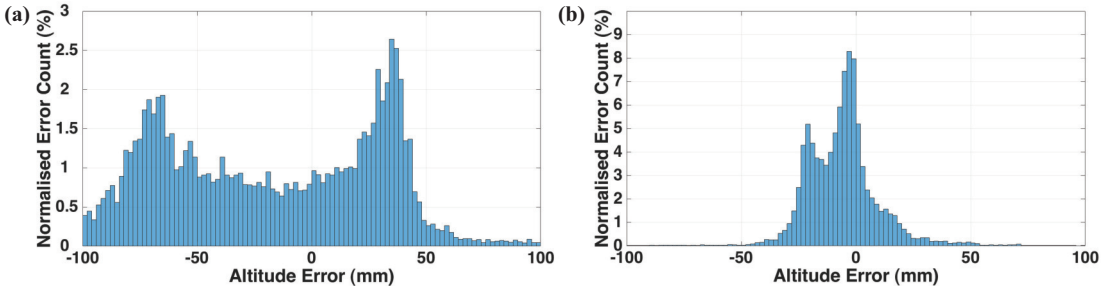

Figure 3.23: Histograms of the altitude errors while the UAV was controlled by (a) Height mode controller (b) hybrid mode controller

addition, as discussed in Section 3.6.1, due to the reduced scanning sweep angle, the output from curve fitting was not accurate enough and caused increments in the standoff uncertainty at the blade edge It should be noted that since the UAV actions in the y-axis were used to maneuverer around the blade, the positional error in this axis was omitted. In addition, the spikes in altitude error in Figure 3.22 represent the procedure while the UAV was changing altitude.

3.7 Conclusions

The main achievement of this chapter was the successful implementation of the PID controller and laser scanner onto the AscTec Firefly UAV. The system was autonomously navigated by the off-board controller workstation, which was the basis of the autonomous NDT inspections, detailed in Chapter 4 and Chapter 5.

The miniature laser range scanner was integrated into the UAV platform to measure the standoff distance and alignment errors relative to the target object's surface. The laser curve fitting procedure improved the accuracy of the distance and alignment offset measurements. This achievement ensured the onboard NDT sensor was positioned at a constant standoff and was perpendicular to the object's surface normal vector. This improved accuracy during the photogrammetric inspection of an object with complex geometry, as detailed in Chapter 4. Such schemes were also utilised to measure the distance and alignment offset versus the inspection sample during the contact-based ultrasonic inspection, as detailed in Chapter 5. The integration also provided the capability to generate adaptive flight paths without prior acknowledge of the target's 3D CAD profile, offering the flexibility of more detailed inspections of in-service, old, and organic infrastructures.

Thus, this UAV platform has the following features:

- The autonomous flight control system navigates the UAV to follow desired trajectories with multiple waypoints.
- The mean trajectory errors are below 30 mm, and the standard deviations are below 15 mm.
- The onboard laser scanner measures the instantaneous standoff distances and alignment errors at 10 Hz.

- The controller can produce an adaptive flight path during the inspections of the object with complex geometry by using the laser scanner mappings of the target asset.
- The standoff distance is maintained by the laser scanner with an error below 30 mm.

Chapter 4

UAV-Deployed Autonomous Photogrammetric Inspections

4.1 Introduction

Photogrammetric inspection is a form of visual inspection, which is a non-destructive testing method that uses one or more cameras to evaluate the surface condition of the assets. The technique and its related algorithms are moving forward, and range of research interests for its NDT applications are growing [4], [151]. The progression can be attributed to the benefits of photogrammetry, such as low cost, fast speed and no requirement for physical contact. Compared with some conventional NDT sensors which measure at discrete points, photogrammetry provides an opportunity to perform a full-field measurement, wherein an informative overview is produced at a relatively rapid speed albeit with no internal structural detail [152].

The application of the photogrammetry technique used on wind turbine blades was started in 1996 by J. Sabel [153]. The researcher deployed two cameras with reflective stickers on the blades to measure the vibration of two 10-metre

diameter blades and the tower whilst the system was still operating. A projector-based system has similarly been applied for turbine blade fatigue testing [154]. Additionally, the photogrammetry technique is utilised to measure the dynamic characteristics of a wind turbine blade [155]. The authors demonstrated a system equipped with two high-speed cameras to capture blade movement.

A UAV with photogrammetric payload enables the technicians to inspect the surface of the large-scale assets [4]. In the existing literature, UAVs have been utilised in various inspection tasks, such as building surveys [12], detecting discontinuities on power cables [13], inspections of a nuclear tank [14] and evaluating structural conditions of bridges [15]. Mansouri et al. describe a UAV swarm approach to inspect an outdoor sculpture where the UAVs were navigated by the stereo camera-based system [16]. The current state-of-art of the UAV inspection of wind turbine blades focuses on improving inspection accuracies, such as developing algorithms to detect defects from offline pictures [156] and investigating mechanical approaches for contact measurements [62, 157]. These conventional photogrammetric approaches typically present inspection results in multiple separate images, which struggle to convey position and location information.

This chapter describes an implementation of a 3D photogrammetry-based NDT inspection method. This method fills the gap of conventional inspections, whereas the current surface evaluations rely on offline images. Compared with inspections from offline images, the 3D photogrammetric inspection provides results with intrinsic position and location information, of great utility in the production of meaningful surface condition evaluations. The reconstruction is a technique whereby multiple 2D images are stitching together to generate a textured 3D model, providing an overview of the target object. The inspections using such a technique require a UAV equipped with a photogrammetric payload to manoeuvre around the target object and take images in different positions and orientations. Such an approach has been utilised on the inspections for bridges, structures and buildings [4]. As documented in [158] and [159], the accuracy of the 3D

photogrammetric inspection results is impacted by the image qualities, UAV movement, environmental brightness condition, motion blur and distance to the object.

This chapter focuses on the implementation of autonomous aerial inspections with the photogrammetric payload. It demonstrates and quantifies the parameters influencing the accuracy of a close-range photogrammetric inspection using an autonomously controlled UAV. A laser scanner based inspection for a wind turbine blade with complex geometry will be presented. The generated 3D profile is more accurate and had more detailed reconstructed features.

This chapter begins by reviewing the principle photogrammetry techniques. Section 4.3 provides an overview of the autonomous UAV inspection system and experimental setups utilised in this chapter. Section 4.4 analyses the impacts of each UAV-deployed image quality parameter. Three parameters impacting inspection accuracy, environmental brightness condition, image motion blur and focal blur, were quantified. These parameters have been identified as the most common sources of the error during UAV inspections and are known to have a direct impact on the image quality and ultimate inspection accuracy [158]. It is found that these impacts can be lessened by appropriate experimental setups and UAV flight paths, which will be demonstrated in the empirical results. Multiple experiments were undertaken with different environmental brightness conditions, different standoff distances and a selection flight paths generated by the laser scanner and are quantified against a manual inspection. Section 4.5 presents an inspection with a laser-based trajectory and describes the impacts of UAV standoff distance. The controller automatically generated real-time adaptive flight path based on the data from the laser scanner to follow wind turbine blade profile. Such laser-controlled flight paths maintained the camera standoff distance and improved image quality when close-range inspecting an object with complex geometry. Section 4.6 describes an algorithm to trim the images and remove the background based on the laser measurements. The results present the importance

of the background features on the camera alignment process. Finally, Section 4.7 presents a prototype image processing algorithm, which detects and highlight the position of the surface imperfections.

The 3D models described in this chapter are reconstructed by a commercial software, Agisoft PhotoScan [160]. GOM Inspection software [161] is subsequently used to quantify the reconstruction accuracies by comparing the reconstructed model with an accurate reference model.

4.2 Principles of Photogrammetry Technique

3D photogrammetric reconstruction is the process of generating a computer model of the 3D profile of an object from a set of 2D images and implicitly displays surface feature locations. This process can be classified into three main categories depending on the type of image acquisition equipment used: single camera-based methods, RGB-Depth sensor-based methods and multicamera network-based methods. An overview of these methods and their respective sub-categories is depicted in Figure 4.1, where the depth of nodes reflects an increasing accuracy. As shown in the figure, Structure from Motion (SfM) [162], Multiview Stereo [163] and Visual SLAM (Simultaneous localization and mapping) [164] are the techniques using a single camera to reconstruct the 3D models. The technique of SfM involves extracting the unique features from a collection of 2D images and matching these features to estimate sparse scene geometry and camera positions. The sparse point cloud and estimated camera positions generated by SfM is further processed by Multiview Stereo technique, which calculates denser point clouds to render an accurate 3D geometry. Visual SLAM reconstructs the large-scale targets and camera surroundings in real-time. However, real-time processing requires enhanced computational power and can come at the expense of reconstruction accuracy. An RGB-Depth sensor outputs a conventional RGB image alongside a depth image.

Depth Fusion [165, 166] uses this information, combined with the traditional RGB image features to reconstruct a 3D model. Similar to the visual SLAM, RGBD SLAM [167] uses the camera outputs to reconstruct the scene. Multicamera based methods [168] use the images captured by multiple cameras placed at various pre-planned positions. Compared with the single camera solutions, the multiple cameras with known camera positions do not require mathematical approaches to estimate camera poses, which improves the reconstruction accuracy. Considering the physical payload mass limitations of the UAV (< 600 g) and submillimetre accuracy requirements of the inspections, SfM and Multiview Stereo are utilised in this research.

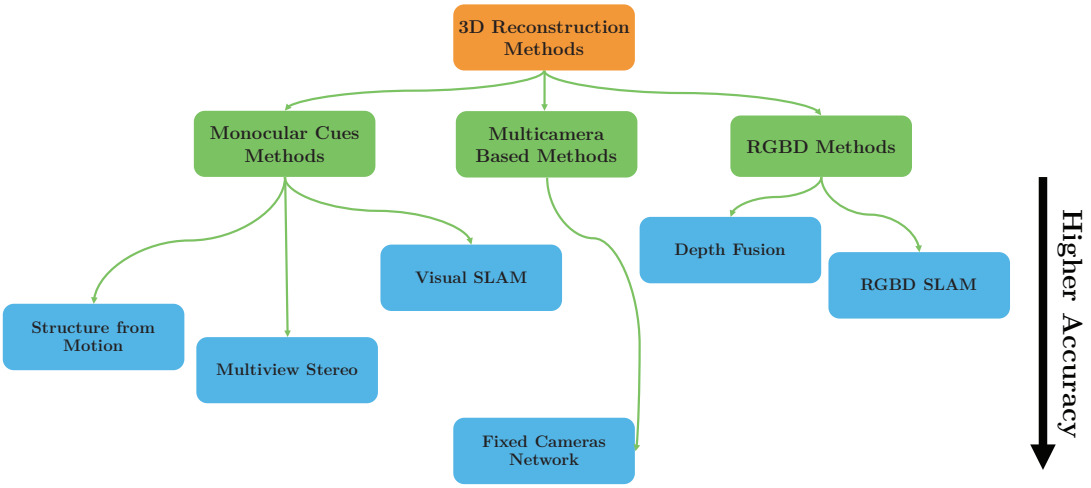

Figure 4.1: Approaches for 3D reconstructions

4.2.1 Structure from Motion and Multiview Stereo

Structure from Motion (SfM) and Multiview Stereo are the photogrammetry techniques, build a 3D model from a sequence of 2D overlapped photographs. These images were captured by a single camera in various positions. The reconstruction process mimics the human vision system, utilising stereoscopic principles to create the 3D scene by observing around the structure [169]. The reconstruction is approached by varying the position of the image sensor to capture a series

of overlapped image frames. The images are typically covered entire three-dimensional scene to build a complete model [170].

The principle of the SfM technique (as per Figure 4.2) is relying on the algorithms to extracting the features from the image sequences. These features are preliminarily matched in various images, captured from different positions and orientations. The matched pairs are then filtered by mathematical algorithms, and valid matches are used to estimate the three-dimensional positions and orientations of images and generate points cloud and 3D model [170]. Due to the lack of alignment distance between the camera and the target object, the 3D model is scale-less and reconstructed in the 'image-space' coordinate system. It can be transferred to an absolute coordinate system by knowing a small number of ground-control points with assets' coordinate [171].

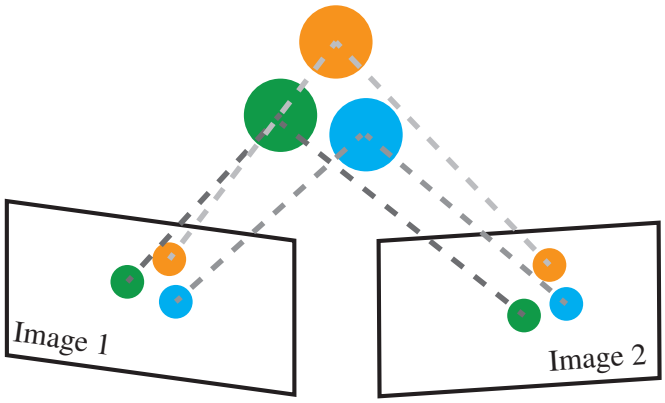

Figure 4.2: Principle of Structure from Motion

During the 3D reconstruction process, the SfM generates the position and orientation estimations of each image frames and offers a preliminary points cloud [163]. The results are not dense enough to provide a detailed 3D model. Hence, Multi-view Stereo technique is utilised to post-processing the sparse cloud. It uses the estimated camera position and the sparse points cloud generated by SfM to create a denser points cloud. The algorithm starts from one of the reconstructed points in SfM results and resamples the neighbour images to insert more surrounding

feature points. The resampling is repeated across the entire sparse cloud so that more points are inserted to reconstruct a more detailed 3D mesh.

These techniques have been commercialised and integrated into many commercial packages, such as Autodesk Recap [172] and Agisoft PhotoScan [160]. Also available on some open-source tools, for example, VisualSfM [173]. Figure 4.4 is a screenshot of PhotoScan, a commercial software for 3D profile reconstruction used in this chapter. The screenshot is an example of the wind turbine blade reconstruction. Relative translations and orientations of UAV images were shown in the image coordinate system. Figure 4.4 is an illustrative example of varying the camera position to capture images for 3D reconstruction.

These reconstruction techniques have been performed and verified the feasibility on the earth measuring [171] and soil water erosion analysis [174]. Furthermore, the technique has been implemented for a user-friendly device, such as the existing mobile phone and webcam [175, 176]. Besides, researchers presented the surface inspection of industrial facility [14] and the infrastructures [177], by using the SfM and Multiview stereo technique with the image acquisitions from UAV.

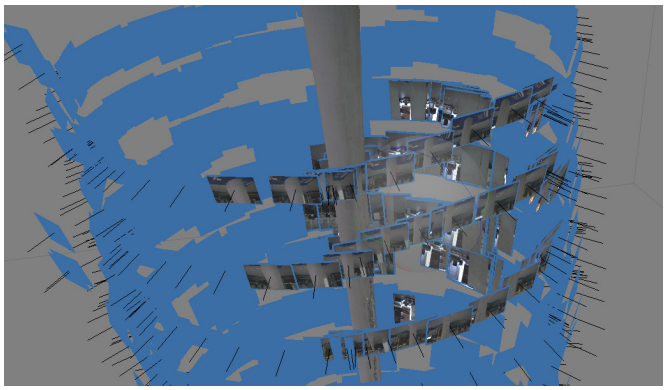

Figure 4.3: An example of the image alignments in the Agisoft software

The SfM and Multiview stereo offer many benefits for the civilian applications, especially non-destructive testing. One of the advantages is that the photogrammetry provides a surface overview of the asset, which enables the defect positions estimation. 3D geometry of the target object is digitised, and deformation can

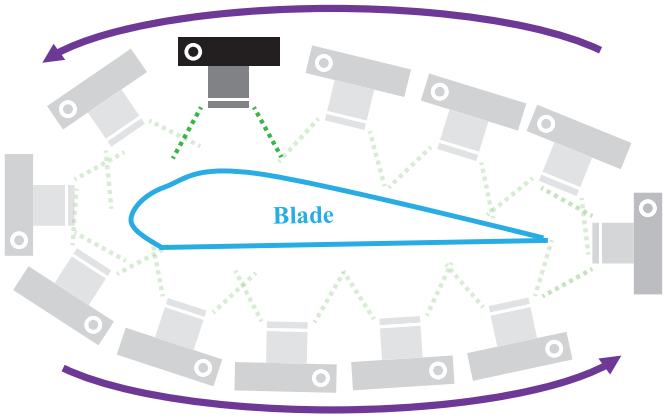

Figure 4.4: Illustrative example of a single camera capturing images for the 3D reconstruction

be detected by the comparison with the previous reconstructed model. Also, non-contact, fast, high-precision grants the benefits of photogrammetric inspection to be competitive to the conventional contact NDT inspections [152, 178].

Although the technique has been commercialised over a decade and algorithm has been improved by many engineers, the limitations and challenges, such as reconstruction for an object with a transparent and glossy surface and sensitivity to the light conditions, still influence the reconstruction accuracy, resulting in the failures or misshapen 3D model [179]. From the NDT perspectives, these limitations and challenges require inspection objects needs to have non-reflective surfaces. The object also needs to be stationary during the inspection. For example, the wind turbine needs to be locked in place prior the inspection. Such challenges, including light conditions and image blurs, will be further discussed in the subsequent sections.

4.2.2 RGB-D Camera

Structured light and Time-of-Flight are two main approaches for RGB-D cameras, which provide the conventional RGB information and the object depth. The principle of the structured light camera (as shown in Figure 4.5) is a triangulation

approach, projecting optical beams with a pre-planned pattern to the target object. The reflected lights from the geometry are captured by a specific camera. The pattern distortions of the reflected beam, caused by the geometry of the object, were processed by the mathematical algorithms and utilised to reproduce the 3D model.

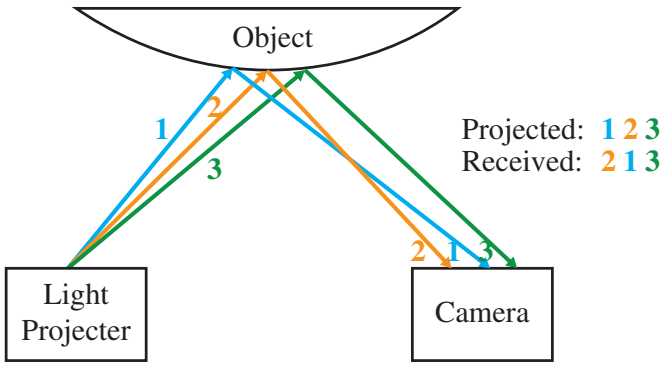

Figure 4.5: Illustration of a structured light camera that results from a structured light projector and a camera in the same scene

Figure 4.5 is an illustrative example of a structured light camera. The beam pattern is simplified to three lights in different colours, whereas actual sensors emerges a ray of lights with a specific pattern to achieve an acceptable resolution. The illuminant projects three light beams with different colours on the object surface. If the target surface is planar, the camera captured pattern is similar to the illuminated. However, if the surface is non-planar, due to the 3D geometry, the camera observed the projected lights with different bearings, and thereby a distorted beam pattern is observed on the camera sensed images. Thus, the 3D mesh of the object can be reconstructed from such distorted patterns captured by the camera [180]. The projected beam pattern can be the lights with varying pattern, sequential projections, grid indexing or stripe indexing [180]. Figure 4.6 shows a specific application, which used a camera based on “de Bruijn sequence” light pattern to reconstruct the 3D mesh of a hand [181].

Such a technique has been seen in the commercialised product, Microsoft Kinect, which reconstructs the volume with game players to improve the gaming experience.

Figure 4.6: 3D reconstruction of the human hand using the structured light camera (a) reference image (b) image with projected structured light (c) image with depth information [181]

The camera reconstructs the 3D scene, whereby projecting infrared lights with many invisible speckles and using an infrared camera to capture a distorted pattern [182]. Intel applies a similar technique on the RealSesnse camera, projecting infrared lights on the object and captures the reflections by a neighbouring camera [183]. These cameras are seen in robotic system researches, such as integrating the Microsoft Kinect into the UAV for 3D indoor mapping [88]; reconstructions of transparent assets [184], and real-time mapping a large-scale scene [185].

Time-of-Flight (TOF) is a technique which utilises the time cost of the lights flighting in the air to retrieve the depth information of the object surface. A typical TOF camera is composed of a conventional RGB camera and an optical depth measurement transducer. The transducer firstly projects a ray of lights (typically a laser beam) to the object surface and then captured the reflection lights. The distance to the surface can be calculated by using the time difference between the transmitted and reflection lights. Figure 4.7 shows the illustration of a Time-of-Flight camera. This technique grants TOF cameras the capability to produce conventional RGB images as well as the depth information [74].

The TOF technique has been applied in commercial products, whereas the camera integrated with the TOF technique recognises the human body, real-time estimates players instantaneous poses, which is aimed to enhance gaming experiences [186]. The tracking algorithm simplifies the human body as a set of skeletal joints so that the system can retrieve the measurement in 200 Hz from a single camera with high accuracy and enhanced tracking throughput. 3D reconstruction for a moving

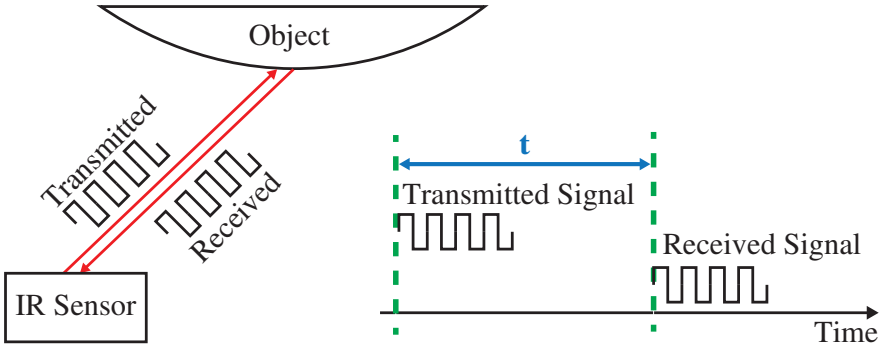

Figure 4.7: Illustration of a Time-Of-Flight camera

object is one of the challenges of the SfM technique. The algorithms described by Y. Cui and others presented the reconstructions for a rotating object and demonstrated the ability to track moving objects by using a TOF camera [187]. The algorithm combines a 3D super-resolution reconstruction and probabilistic scan alignment, which gives the general errors below 1 cm. Anwer et al. performed underwater 3D reconstructions by utilising a TOF camera and demonstrated the capability of TOF camera to overcome the light refraction correction, which is a great utility for the underwater mappings and SLAM [188].

4.3 Overview of the Photogrammetric Inspection System

The inspection system utilised in this chapter (as shown in Figure 4.8) is composed of: an AscTec Firefly UAV [22], a FLIR machine vision camera CM3-U3-50S5C-CS [189] with an 8 mm, F2.4, 57.8° field of view lens [190] and a Hokuyo URG-04LX laser scanner [109]. The photogrammetric payload is mounted on the UAV and captures 4 MegaPixel (MP) raw images at 2 Hz, and the camera lens was manually adjusted for optimum focusing. Sensor communications and image acquisition are processed by the UAV's onboard Intel Core2 Duo Computer (running a Linux-based Operating System). The raw images, captured during the UAV flight,

were saved on this computer, then exported to an offline computer for further reconstruction processing. The increased moment of inertia about the UAV's z-axis introduced by the mass of the payload (listed in Table 4.1) slightly diminish the positional stability. The standard devition on the x-axis growing from 10.40 mm to 16.16 mm, while similar z-axis stability was observed in the flight with and without the payload. The error in y-axis is omitted because the UAV actions in this axis were used to follow the target geometry and so the error is of no consequence during photogrammetric inspection.

Table 4.1: UAV payload mass for the photogrammetric inspections

	Mass (g)
Onboard Computer	369
Laser Scanner	160
Lens	84
Camera	55

As described in Chapter 3, the UAV was autonomously stabilised and guided to follow inspection trajectories by a customised controller running on an off-board, ground-based workstation. The workstation updates the control parameters every 50 ms. The aircraft's flight controller is based on a closed-loop Proportional-Integral-Derivative (PID) architecture and adjusts the UAV attitude depending on the difference between desired and actual pose.

While the UAV described here is designed to undertake outdoor inspections, the experiments demonstrated in this chapter were undertaken within a laboratory environment, wherein GPS signals are unavailable to provide a reliably accurate position for UAV tracking and navigation. Consequently, a high-accuracy photogrammetry-based position measurement system Vicon is used as a replacement for GPS when performing indoor navigation. This system comprises twelve optical cameras and tracks the six degree-of-freedom UAV pose at 100 Hz [97].

The Hokuyo laser range scanner [109] mounted atop the UAV is utilised for mapping the target and other local infrastructure in front of the UAV. Here, the

sensor outputs are used to maintain the UAV standoff distance and generate adaptive flight path during the inspection.

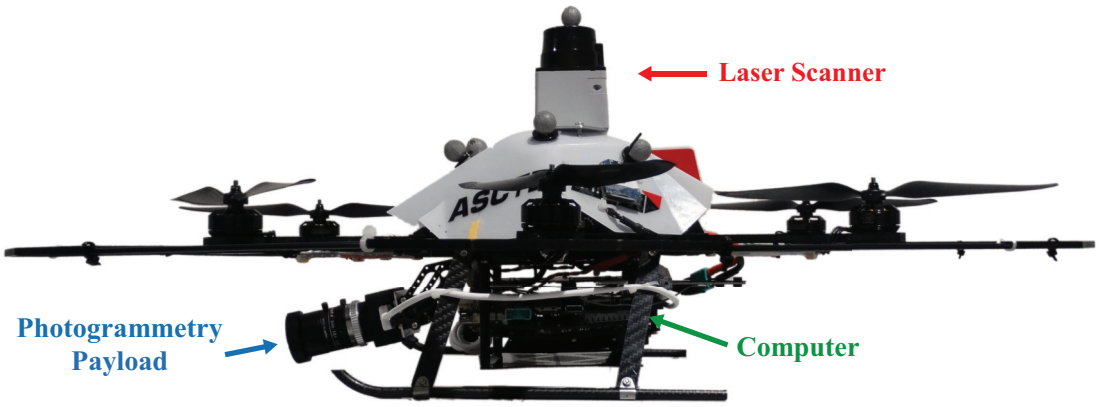

Figure 4.8: AscTec UAV with an onboard computer, camera and laser range scanner

The inspection target utilised in this chapter is a 3.1 m high section of the wind turbine blade, a decommissioned part of a Gaia–Wind turbine [17]. The blade section is mounted vertically and tapers from 619 mm wide at the bottom to 386 mm wide at its highest point. Though the indentations and imperfections are observable on the surface, to better quantify the performance of the 3D reconstruction and adjust the camera focusing, the blade surface has undergone some prior preparation. Ten 6.5 mm dots and a textured yellow 20 mm tape were pasted on the surface, as in Figure 4.9.

The 3D reconstruction is conducted via Agisoft PhotoScan [160], a commercially available stand-alone software product which performs photogrammetric processing of digital images and generates 3D spatial data. The software assumes the images are captured from a series of cameras in various unknown positions. It then calibrates the camera using Agisoft proprietary algorithms [160] before extracting and matching the features from consecutive images to estimate their relative poses. Point clouds, meshes and textured reconstructions are built in sequence to create a detailed 3D profile.

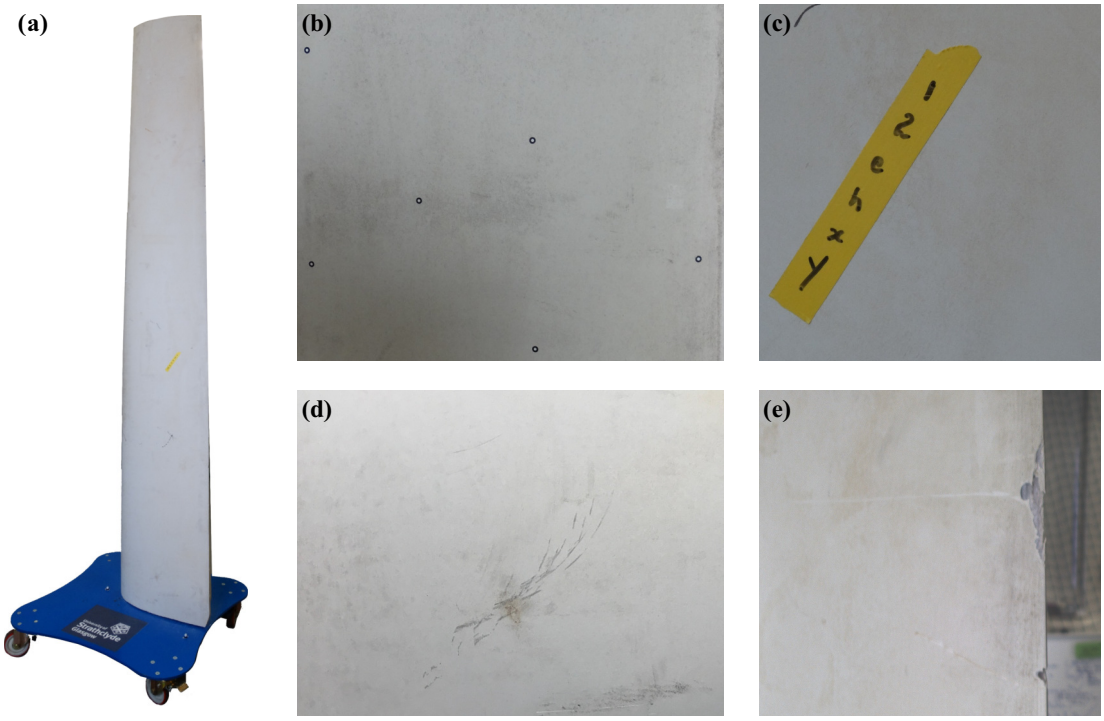

Figure 4.9: Inspection asset (a) wind Turbine Blade for inspection (b)(c) dots and texture features added to the blade surface (d)(e) existing indentations and imperfections on the blade surface

The software is using the Structure from Motion technique, which assumes the images are captured from a single camera in various positions. The marks, defects and discontinuities from the assets as well as the background are the features used as reference points for the reconstruction. The software firstly matches these points from different images and align these images followed by the optimisation algorithms to calculate the estimated camera positions. Then, the preliminary points cloud, denser points cloud, mesh and textured model are built successively to create more detailed 3D objects. During the points cloud generation, the software extracted the features from the background and the asset. The field of interests in the photogrammetric inspection is only the scene where the target object is located, so the background points generated in position estimation stage were removed before producing denser points cloud to save processing time.

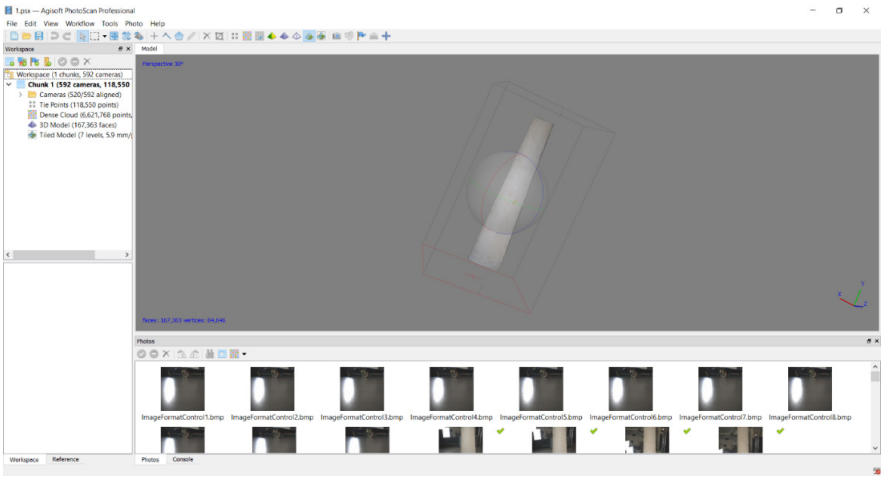

Figure 4.10: Graphical User Interface of Agisoft Photoscan

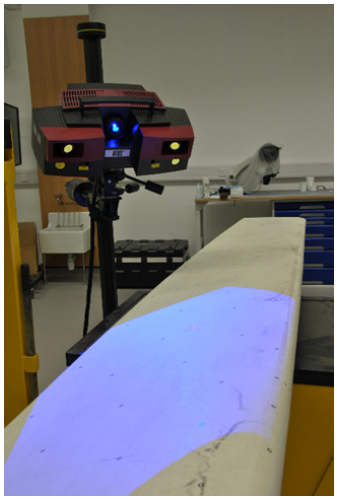

Figure 4.11: Scanning Progress of the blade using GOM ATOS Triple Scan System

To ascertain the accuracy of the inspection results, a reference CAD model was captured using the GOM ATOS Triple Scan system (as shown in Figure 4.11). The model generated by the GOM system has been shown to be highly accurate, with nominal surface deviation below 20 µm [161]. Complete mesh data from PhotoScan was imported into GOM Inspect, software used for comparison with the reference CAD model (as present in Figure 4.12). Note that because monocular photogrammetry is a dimensionless technique and, as such, the scale factor is unknown during the reconstruction process, the output from the software does not contain the absolute sizing of the model [191]. Therefore, prior to comparing the

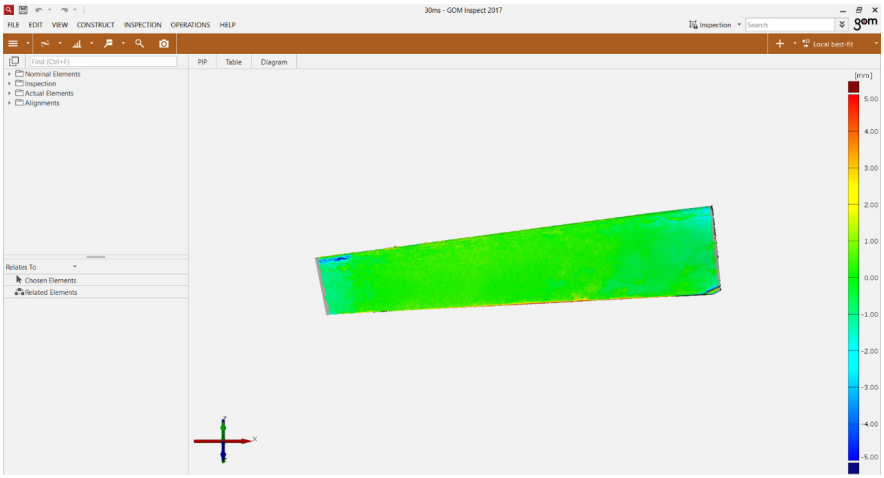

Figure 4.12: Graphical User Interface of GOM Inspect Software

models, a scaling factor for the mesh and coordinate allocation is first required. These were obtained by identifying two distinctive points from the mesh and fine-tuned by minimizing the surface deviations. Applying this factor and conducting the model comparison, the standard deviation, mean error, error range (maximum error minus negative error in the sample) and a deviation map can be obtained from GOM Inspect. The standard deviation represents the noise level on the model surface, while mean error and error range denote the geometric difference.

Figure 4.13 shows the reconstructed model from the Agisoft PhotoScan software. Reconstructions achieved by this UAV system for photogrammetric inspection present with the mean error below 0.25 mm relative to the GOM reference model. error range and standard deviation are below 4.3 mm and 0.92 mm, respectively. Figure 4.14 shows the comparison between textures from the images captured by UAV and the features on the reconstructed mesh. These highlight the textures on the blade surface can be clearly identified in the reconstructed model.

The system diagram of the UAV-deployed photogrammetric inspections are shown in Figure 4.15.

Figure 4.13: Reconstructed 3D model for the wind turbine blade

4.3.1 Experimental Setup

The main considerations during camera selection for remote airborne inspection are the dimensions, mass, resolution, frame rate and the communication interface. Dimensions and mass are restricted by the UAV's hardware payload limitations. Frame rate and communication interface relate to the software application and image processing speed. Higher resolution cameras offer the capability to capture more detailed surface features. There exists a significant repository of institutional experience with the communication interface employed by the Chameleon3 following its deployment within other previous research projects [10, 32]. Hence, the camera with the highest specifications and resolution in the Chameleon3 series has been selected as the photogrammetric payload for the UAV inspections detailed here. The camera nominal sample rate is 35 frames per second. However, due to hardware limitations associated with the data transfer between the camera and the UAV's onboard computer, the actual executed frame rate is 2 Hz. Image

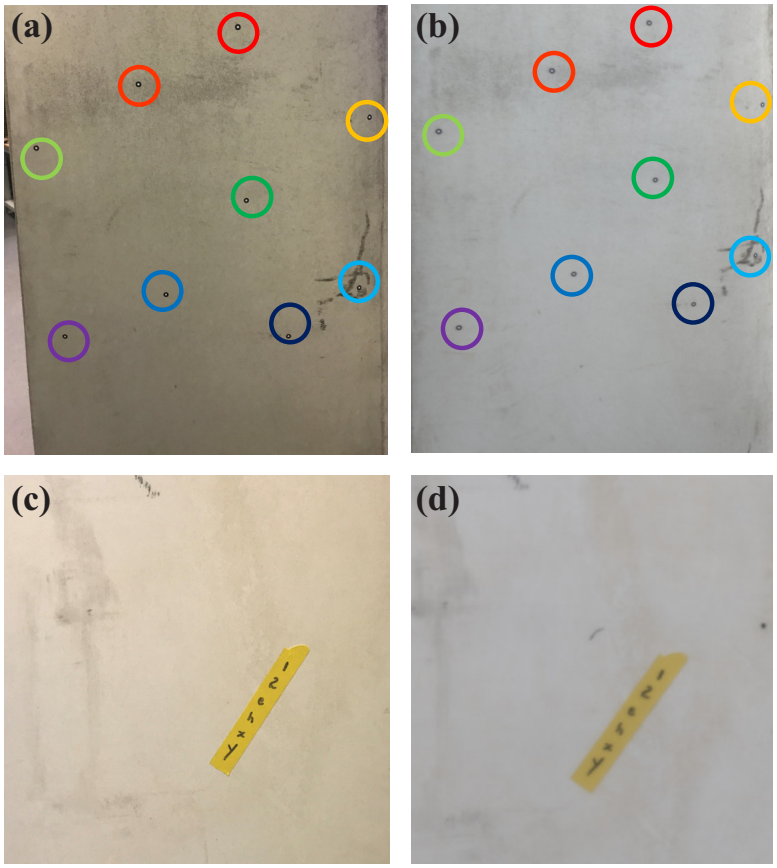

Figure 4.14: Comparison between the reference images and reconstructed model. (a)(c) reference camera captured, (b)(d) reconstructed mesh

compression is disabled during the inspections to prevent image distortions during compression.

The focal length of such a lens dictates the camera field of view and so has a significant impact on the remote visual inspection process. Short focal length provides a wide field of view, reducing the number of images required for covering a given surface but diminishing the ability of the images to accurately resolve small features. Selecting a lens with a wider aperture enables more light to enter the camera, improving the image brightness. The Computar MPW2 lens series is designed for compatibility with cameras using 5 MP and 2/3" sensors. Since the UAV inspections require the imaging of a large area of the structure, M0824-MPW2 (as per in Figure 4.16), the smallest focal length in this series (8 mm), was selected for use and mounted with the Chameleon3 camera on the front

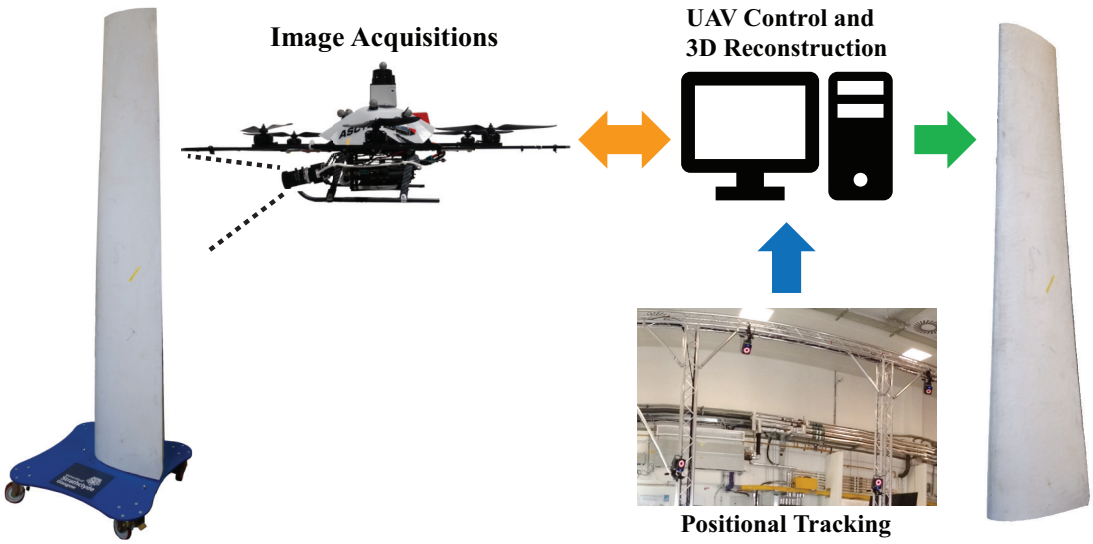

Figure 4.15: System diagram of the photogrammetric inspections utilising the autonomous UAV system

of the UAV. The lens however has no capability for automatic focus adjustment. Therefore, this was set manually by placing the craft at the required standoff distance to the target object and incrementally adjusting focus to acquire the optimum surface texture sharpness.

Figure 4.16: Photogrammetry payload including the lens

4.3.2 Image Acquisition Process

The communication between the computer and the camera is based on Spinnaker SDK provided by the camera manufacturer. The image acquisition is approached

in the customised software running on the UAV onboard computer. The flowchart of the image acquisition part of the software is shown in Figure 4.17.

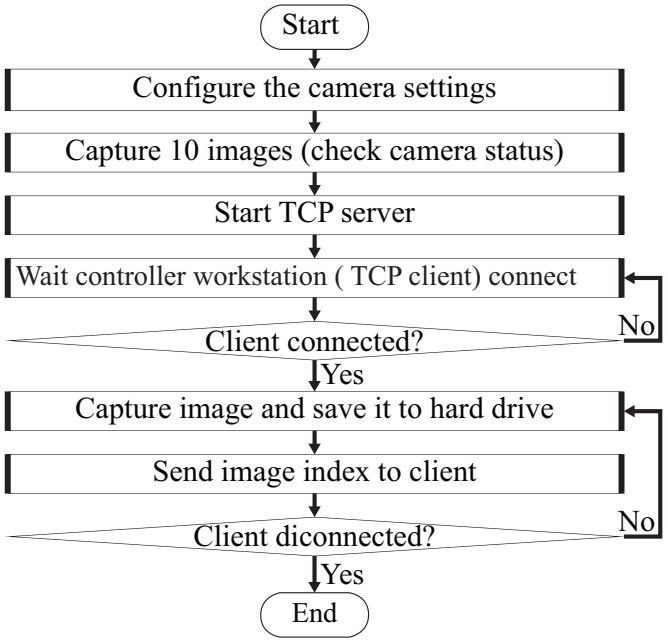

Figure 4.17: Flowchart of the image acquisition

The software application initially configures the camera settings for different experiment requirements, followed by several image acquisition trials to verify the camera availability. The experiments were undertaken within a laboratory environment, the sensor light sensitivity was set to maximum to provide the brightest images. After camera initialised, the software starts a TCP server at port 5050 and waits for the network handshake from the off-board workstation. The image acquisition was started once the workstation connected to the server and finishing after the workstation terminates the TCP connection. Once the software received a new image, it sends the image file name to the laptop for the frame rate calculation. When the software on the controller laptop received a new file name, it records the instant pose of the UAV and laser scanner readings for offline image processing and data analysis. Due to throughput limitation of the Wi-Fi channel, the images are initially saved to the local hard disk on the onboard computer and exported to the higher performance laptop after UAV landing for 3D reconstruction.

4.4 UAV Inspection Image Quality Parameters

4.4.1 Environmental Brightness Condition

Image brightness is one of the parameters influencing image quality and reconstruction accuracy [158]. The images captured under low light intensity lost the detailed features of the target surface leading to the failure of image feature extraction algorithms and hindering the reconstruction process. Undertaking the experiments in a laboratory environment allows the ambient light levels to be fully controllable by the use of diffuse supplementary lighting. Within the laboratory and in the absence of additional illumination, the light intensity was measured by a calibrated lux meter as 65 $\pm$ 5 lx. To quantify the impact of the light intensity on reconstruction accuracy, six additional 135 W lights with a colour temperature of 5500 K were set-up at suitable locations around the wind turbine blade, as shown in Figure 4.18. These external lights introduce additional illumination of the blade surface and permit increase in environmental light levels by a factor of three, from 65 lx to approximately 200 lx. By comparison, the ambient environmental light measured by using the lux meter outdoors on a cloudy day is around 2000 lx. This laboratory lighting environment, therefore, provides a good facility to investigate the impact of the environmental brightness parameter on reconstruction in such conditions as may be encountered in practice during markedly poor weather.

Operating within an environment with poor light intensity, increasing the camera shutter time allows more light to fall onto the camera sensor and so produces brighter images. However, slower shutter speed introduces more motion blur to the images owing to small motions of the UAV platform. In contrast, decreasing shutter time can reduce the blur but sacrifices image brightness. Motion blur is also a source of reduced image quality and strongly influences the inspection accuracy, obscuring visual features and hindering the functionality of algorithms for feature detection employed in the reconstruction progress. Further details of

Figure 4.18: External lights setup

these effects will be provided in Section 4.4.2. However, because of the brighter light conditions outdoors, the shutter time can be reduced to 1 ms during these inspections to mitigate the motion blur issue.

This experiment is designed to quantify the impact of the lighting conditions and shutter speed on the reconstructed models. The UAV flight path in the experiment was a pre-planned circular path, taking the UAV a complete rotation around the wind turbine blade section before dropping down and performing the next loop all while capturing images at regular time intervals. In this scenario, the camera shutter time was set to be 30 ms, representing the time that the camera captured the best image quality in the presence of the additional lighting. The first image sequence was captured under the environment with six additional lights, the second and third were captured without these lights. In the third trial, to demonstrate the impact of shutter time on reconstruction accuracy and create similar image brightness to the well-lit trial, the camera shutter speed was changed to 60 ms. Figure 4.19(a)-(c) displays raw images taken at similar locations for comparison between the three image sequences, captured under different light intensity and varying shutter speed. The deviation maps and the errors of reconstruction models under each of the three setups are illustrated in Figure 4.20 and Table 4.2. The quality of the images from the inspections with

three setups are plotted in Figure 4.21. The image qualities from each trail are quantified by using the matching feature density metric, as explained below.

Image feature matches are the key factors to the 3D reconstruction process. More feature matches will provide a better quality of reconstructed model. The percentage of image overlap influence the number of feature matches. The matching feature density is introduced as a comparative metric to represent the number of the matched features in an overlap region and quantitatively assess how this impacts the quality of the final reconstruction. It is calculated by dividing the number of the matched features between two subsequent images by the percentage area of their overlap. Using the matching feature density to quantify image quality during the autonomous UAV inspections, image sequences captured with different optical setups can be directly compared and evaluated. Higher density implies that the image had more matching features and is thus indicative of better image quality.

A forth image sequence using the 60 ms exposure time and additional lighting is not conducted as this leads to overexposed images (as shown in Figure 4.19(d)) from which no meaningful results may be extracted. In this instance, the reconstruction result may be worse than the 30 ms shutter without lights, because the features are unrecognisable in overexposed images.

Unlike indoor inspections, the light conditions during outdoor inspections are not controllable. For example, situations involving a backlighting phenomenon, where the target object is located between the lighting source (the sun) and the camera, may occur. In attempting to set an expose time in this scenario, a slow shutter speed will overexpose the background (similar to Figure 4.19(d)) while a faster shutter speed will underexpose the target surface (similar to Figure 4.19(b)). Both extremes will reduce the number and quality of features visible in the image owing to the limited dynamic range of the camera. However, since the background

features are less important than the features on the target, the shutter speed can be optimised for the exposure of the target object.

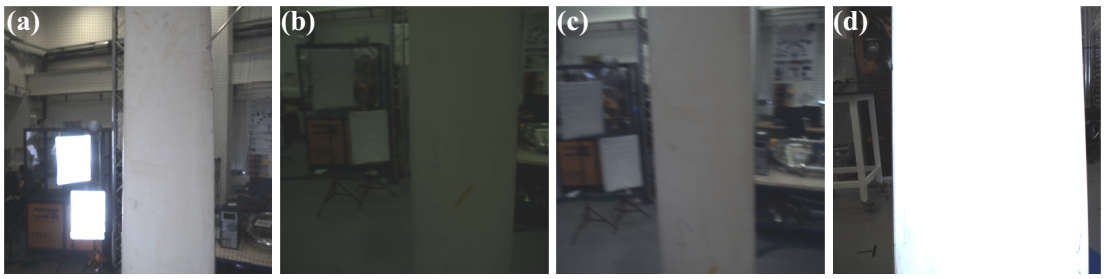

Figure 4.19: Images captured under (a) 30 ms shutter with lights (b) 30 ms shutter without lights (c) 60 ms shutter without lights (d) 60 ms shutter with lights

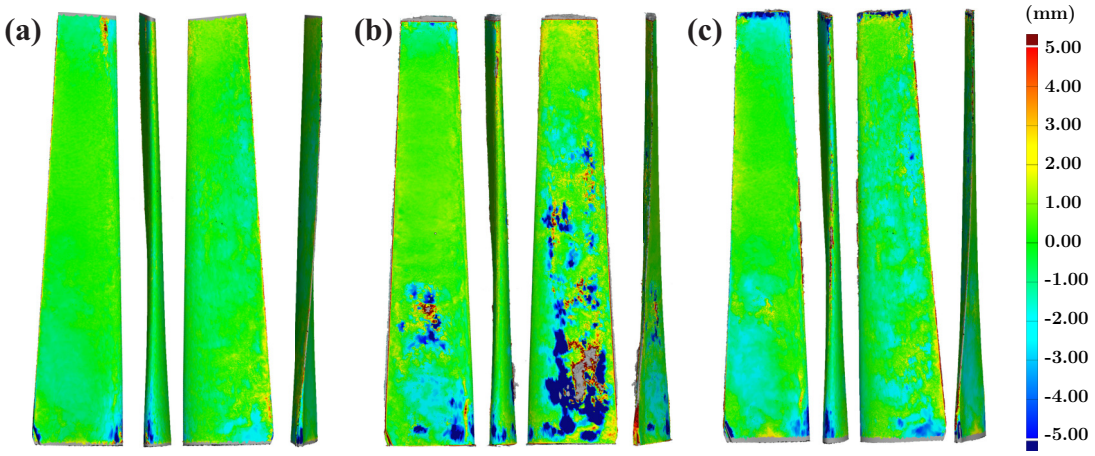

Figure 4.20: Deviation maps of the reconstruction model captured in different parameters, refer to the GOM model as described in Section 4.3 (a) 30 ms shutter with lights (b) 30 ms shutter without lights (c) 60 ms shutter without lights

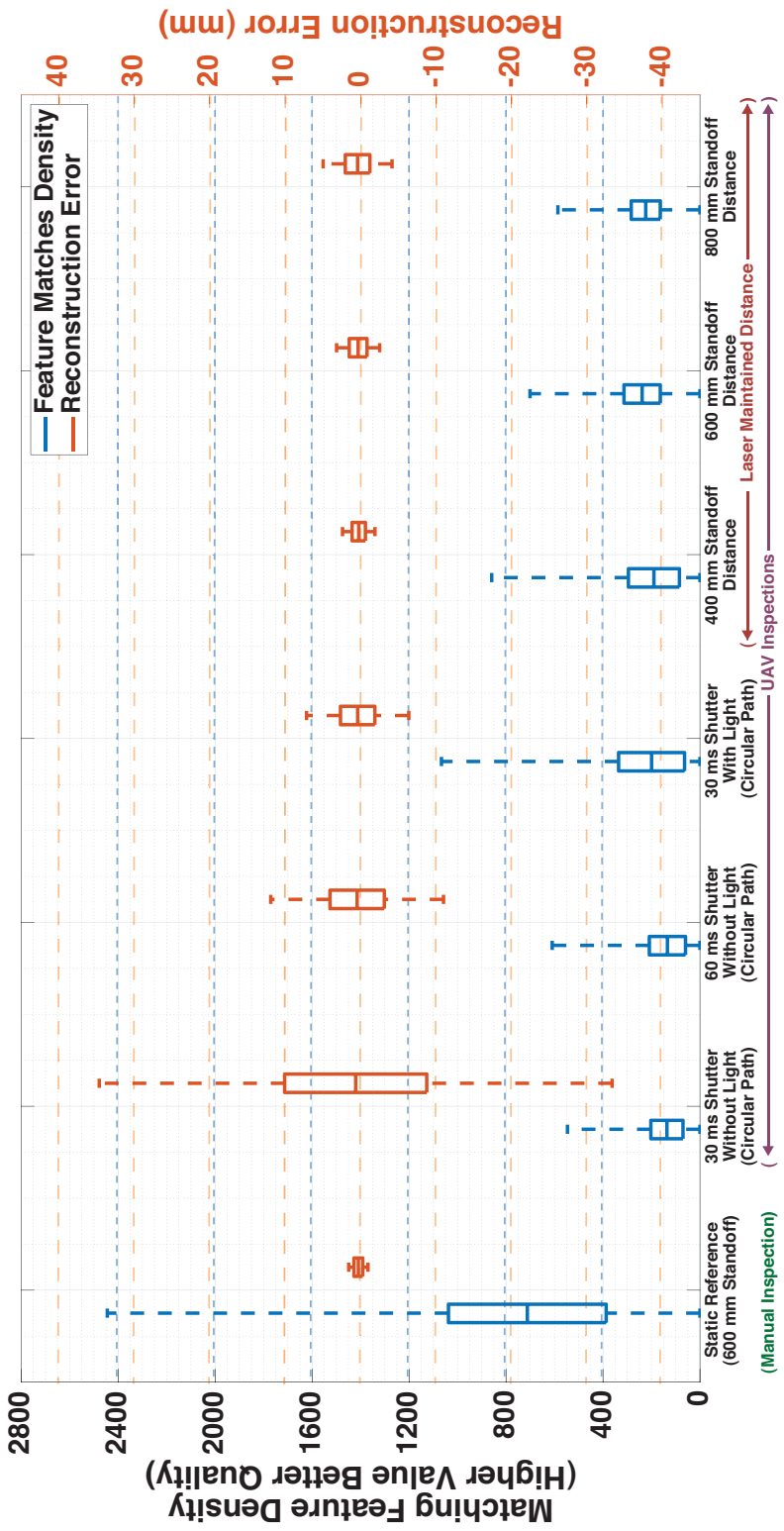

Figure 4.21: Image quality and reconstruction error under different experimental setups. The reconstruction errors were plotted by using the mean errors and standard deviations. Box and whisker stand for the standard deviation and the full sample range, respectively.

Table 4.2: Reconstruction errors from the inspection with different environmental brightness conditions, refer to the GOM model as described in Section 4.3

	Mean Error (mm)	**Standard Deviation (mm)**	**Error Range (mm)**
30 ms shutter with light (Light = 200 lx)	0.3853	1.56	13.56
30 ms shutter without light (Light = 65 lx)	0.6493	2.46	68.00
60 ms shutter without light (Light = 65 lx)	0.4571	1.97	22.91

The image quality (as presented in Figure 4.21) shows the images captured under the low light intensity and without external lights had the worst quality. The quality was improved with the increment of the shutter speed and increased environmental light intensity.

As presented in Table 4.2, the model reconstructed from the images captured under 30 ms shutter speed, in relatively dark conditions, had 70% worse geometry alignment and around 60% larger standard deviations than the model from the images captured in bright condition. Compared with the model acquired in bright conditions (Figure 4.20(a)), the mesh acquired in dark condition had a large discontinuity (Figure 4.20(b)). Discontinuities and misalignment were seen at the bottom section of the mesh due to the loss of image features in the low light environment and inability of the reconstruction algorithms to accurately extract the blade structure in these regions.

Under the same lighting conditions, the increased shutter time of the third data set improved the image brightness by 40%, leading a 30% reduction on the mean error (from 0.65 mm to 0.46 mm) and 20% reduction on standard deviation (from 2.46 mm to 1.97 mm). Additionally, as presented in Figure 4.20(c), the PhotoScan software generated a complete mesh for the wind turbine blade. However, the

model errors are still over 20% larger than in the case using the images with shorter shutter time in a brighter environment. As described previously, the error is identified as a result of additional motion blur, caused by the UAV movements and compounded by the slower shutter speed. These effects coupled with feature distortions, manifest as a change in error range of 9.35 mm.

4.4.2 Motion Blur

Motion blur appears from the UAV movement during the camera exposure. During the UAV inspections, the motion blur is related to the UAV flight stability and velocities in all six degrees of freedom, rotational and translational [159]. To investigate the impact of the motion blur on the reconstruction accuracy, the inspection was initially undertaken by the UAV operating with full autonomous control. By comparison, data set was acquired with the camera statically mounted on a tripod and positioned at a standoff of 600 mm to the blade surface to provide the best-case images capturing in the absence of the UAV movement and motion blur. These experiments were undertaken with enhanced illumination from the external lights allowing the camera shutter time to be set at 30 ms.

As shown in Figure 4.21, the images captured during the manual inspection had better qualities than the images taken during the UAV flight with the same standoff. The reconstruction accuracies listed in Table 4.3 show the motion blur from the autonomous UAV slightly increased the mean alignment error. The addition of motion blurs leads to the increase of the standard deviation and error range by a factor of two. Motion blur causes distortions in the image and so induces error in the reconstruction results. However, due to the nature of UAV flight, these motion blur effects cannot be fully eliminated, only compensated for by the informed selection of camera settings, such as faster shutter speed.

Table 4.3: Reconstruction errors from the UAV inspection and manual inspection, refer to the GOM model as described in Section 4.3

	Mean Error (mm)	**Standard Deviation (mm)**	**Error Range (mm)**
Manual Inspection Using Tripod (600 mm Standoff Maintained by Laser Scanner, Light = 200 lx)	0.2956	0.71	2.55
UAV Flight (600 mm Standoff Maintained by Laser Scanner, Light = 200 lx)	0.3098	1.29	5.09

4.4.3 Focal Blur

The depth of field, or focus depth, is the distance between the nearest and furthest positions relative to the camera at which an object located will begin to exhibit an unacceptable loss of sharpness in its captured image [192]. The remainder of the scene behind and in front of these two positions is distorted and exhibits focal blurring. In the context of photogrammetric inspections, focal blur appears when the camera is positioned such that the target object is located outside the depth of field. This distorts the appearance of the image features relied upon during reconstruction and so produces a malformed 3D representation, degrading the inspection quality and increasing the possibility of errors when examining discontinuities [159]. The camera utilised to conduct photogrammetric inspections presented here is adjusted to be focused on the blade surface to achieve the best sharpness at a given standoff distance. Conventional UAV-based photogrammetric inspections are performed using a high-resolution camera with large standoff distance to avoid the risk of collision. The width of the depth of field is incremented with the camera standoff distance [192]. Therefore, cameras in conventional inspections have a broader depth of field and the ability to capture

images with less focal blur. However, inspections with a close proximity grant opportunities to capture more detailed surface features.

The depth of field relates to the camera sensor dimensions, aperture, focal length and working distance. The mathematical representations of this relationship (as shown in Figure 4.22) is given by Eq. (4.1) [192].

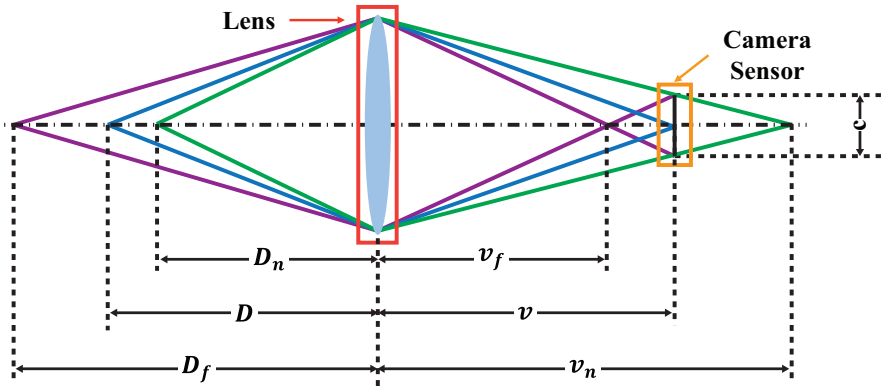

Figure 4.22: Mathematical representations of depth of field, focal length, aperture, sensor dimensions and working distance, adapted from [192].

$$\begin{aligned} \frac{v_n - v}{v} &= \frac{c}{\frac{f}{N}} = \frac{v - v_f}{v_f} \\ \frac{1}{v} + \frac{1}{D} &= \frac{1}{f} \\ \frac{1}{v_n} + \frac{1}{D_n} &= \frac{1}{f} \\ \frac{1}{v_f} + \frac{1}{D_f} &= \frac{1}{f} \end{aligned} \tag{4.1}$$

where c is the camera circle of confusion diameter limit (0.008 mm), f represents the camera focal length (8 mm), D denotes the working distance between the camera and assets and N is the lens aperture f-number (2.4). v is the image distance. v_n, v_f are the distances of the image plane where the objects are in focus.

Objects located at D_n and D_f are focused at the image distances, v_n and v_f. These objects are captured as blur spots at the image distance v. D_n and D_f

stand for the distance between the lens and nearest, farthest objects, which can be captured with acceptable sharpness by the camera. Thus, the depth of field (δ) can be calculated by the formula [192]:

$$\delta = D_f - D_n = \frac{f^2 D}{f^2 - Nc(D-f)} - \frac{f^2 D}{f^2 + Nc(D-f)} \tag{4.2}$$

Since the value $D \gg f$, the equation can be simplified to:

$$\delta \approx \frac{f^2 D}{f^2 - NcD} - \frac{f^2 D}{f^2 + NcD} = \frac{2cND^2\ f^2}{f^4 - c^2 N^2 D^2} \tag{4.3}$$

During the close-range inspections (D <1000 mm), $\frac{f^4}{c^2 N^2 D^2} > 10$. In this instance, Eq. (4.3) can be simplified to:

$$\delta \approx \ \frac{2cND^2 f^2}{f^4} \approx \frac{2cND^2}{f^2} \tag{4.4}$$

It is also worth to note that the depth of field is asymmetrical respect to the focal point. This is because the lens reflections, causing the light from the near distance D_n converges behind the camera sensor, while the light from the far distance D_f converges in front of the camera sensor, as shown in Figure 4.22 [193, 194].

The applications presented in this chapter were examples of such close-range inspections, wherein the UAV on which the camera was deployed was positioned at a standoff distance of 600 mm to the blade surface. This leads to a comparatively shallow depth of field. The depth of field is around 319.7 mm with 600 mm UAV standoff distance. Thus, the UAV is required to maintain within the closest distance of 470 to 790 mm to the surface of interest in order to capture images with acceptable sharpness.

To demonstrate the impact of standoff distance on image quality, photographs of an ISO 12233 Test Chart [195] were taken at various standoff distances using the Chameleon3 camera and Computar lens. The test chart has abundant textures and is designed specifically to test the camera resolution and focal point. In the

experiment, the camera is focused at 600 mm UAV standoff and then displaced to a range of positions along the surface normal vector. Images are captured from a standoff of 300 mm to 1000 mm in 100 mm increments. Figure 4.23 depicts the test chart images, taken from 300 mm and 600 mm standoff distance. Compared with the image captured at 600 mm standoff (as in Figure 4.23(b)), the image from 300 mm distance is much blurrier and out of focus.

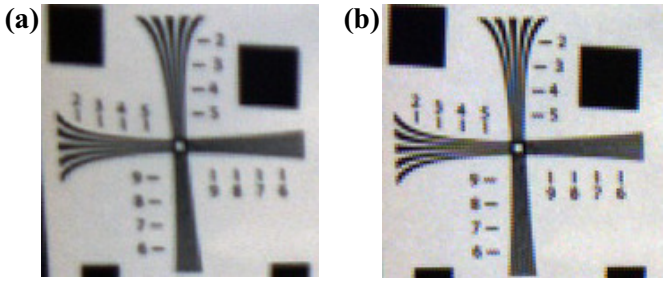

Figure 4.23: Captured Test Chart (cropped to show the area of interest), while the camera is focused on 600 mm standoff distance (a) camera was placed at 300 mm standoff (b) camera was placed at 600 mm standoff

An open source blur metric function, evaluated within the MATLAB data processing software environment, was utilised to quantify the degree of blur present in the captured images. This blur metric function described by Crete-Roffet et al. [196] is based on a percentage similarity comparison between the original image and image after passing through a low-pass filter and function as a relative comparison between two images of the same subject. The quality of the images captured at different standoff distances evaluated using this metric is plotted in Figure 4.24. A higher value of blur index implies poorer image quality. As expected, the camera captured the best quality in the focal point and quality became worse with the standoff distance away from the focal point.

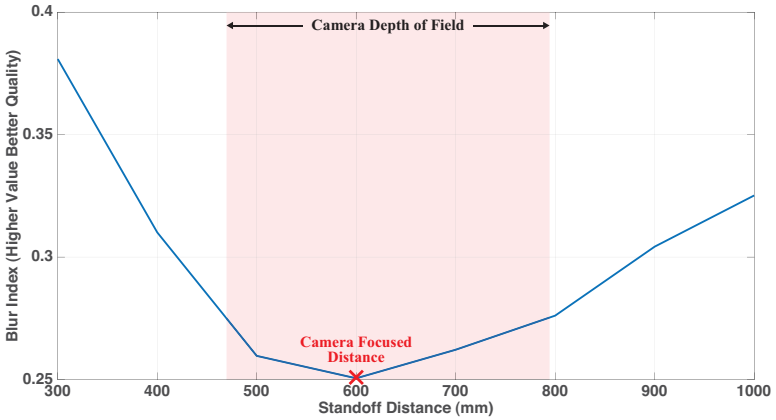

Figure 4.24: Image qualities at various standoff distances (camera is fixed focused at 600 mm)

4.5 UAV Flight Path Parameters

4.5.1 Laser-based Flight Path

The results presented in Section 4.4.3 illustrate the relationship between the standoff distance and image quality. To acquire precise photogrammetric inspection results, the target object in the images is required to be resolved with sufficient sharpness to extract features and structures. Therefore, the UAV standoff distance needs to be maintained at a level that places the inspection target within the camera lens' depth of field. The flight trajectory is thus required to track the asset's geometry so as to maintain appropriate standoff distance and ensure the camera focal point lies as close as possible to the asset surface.

There are two methods to maintain the standoff distance and guide the UAV to follow the target geometry. Firstly, a pre-planned path can be programmed and assigned by utilising an existing 3D mesh of the inspection scene [197]. However, this method is less robust because the flight trajectory is hardcoded and so relies on both an accurate 3D model and strong disturbance rejection in the UAV controller. In a laboratory environment, the target object can be moved to a known place for inspection, typically the centre of the measurement volume, and

a flight trajectory generated accordingly. Difficulties associated with locating the planned flight trajectory relative to the physical structure and an increased likelihood for environmental disturbances mean that this method is not suitable for inspection of in-service assets. It is insufficiently robust to provide safe and reliable inspections when flying under autonomous control and in close proximity to industrial plant items.

The second method entails applying a miniature laser scanner to provide real-time feedback control. The laser scanner is equipped aboard the UAV to measure the displacement to its surroundings and the target object. A curve fitting algorithm is utilised to process the raw data output and compute the standoff and orientation errors in real-time. Compared with the pre-planned path, this method does not require knowledge of the target model and represents a much more feasible approach to avoid collisions during close-range inspections. In this method, measured distances are fed into the UAV controller to maintain the standoff distance. Alignment errors between the UAV yaw angle and surface normal vector are calculated to adjust the UAV orientation in real-time. This can guide the UAV to follow the object geometry and maintain the position of the target object within the camera's depth of field. To demonstrate the minimisation of the impacts of focal blurring, the inspection path was compensated to follow the adaptive trajectory, computed in real-time using data from the laser scanner.

The inspection with pre-planned circular path was utilised for comparison with the adaptive path. The circular path comprises nine circumferences with fixed distances to the blade centre varying in accordance with altitude, owing to the tapering of the blade profile along its length and its vertical mounting. The UAV starts circular manoeuvring around the top of the blade and finishes at 0.7 m above the ground to ensure complete coverage the whole blade's surface area. Upon completing each circumference, the altitude is decreased by 300 mm, and the UAV commences travel around the next layer. This vertical separation is

selected to ensure sufficient vertical image overlap, which is depending on the vertical camera field of view, as shown in Figure 4.25.

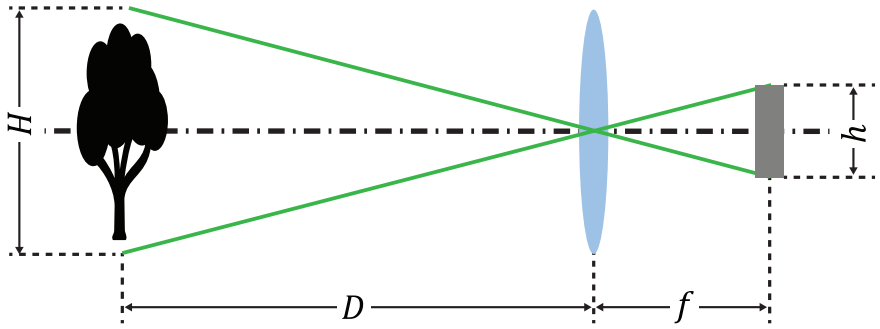

Figure 4.25: Diagram to calculate the height of the object reflected on the sensor

The vertical field of view is calculated from [192]:

$$H = \frac{h}{f} \times D = \frac{6.9}{8} \times 730 = 629.6\ mm \tag{4.5}$$

where h, f and D stand for sensor height, focal length and working distance.

Similarly, the horizontal field of view is about 771 mm. The calculation result shows the camera can capture $771 \times 630\ mm^2$ of the blade surface, with 600 mm UAV standoff distance. The sufficient image overlap is 50% of the field of view, as described in [198]. Hence, the altitude difference between two circumferences was selected as 300 mm. The horizontal field of view is naturally guaranteed since the UAV was slowly manoeuvring around the blade, and the camera was configured as continuous acquisition mode. The average image overlaps in the entire inspection, calculated by MATLAB, were around 80%. Because of the geometry of the blade, the radius of the top circle is 1100 mm, and the rest of the circles are increased 50 mm progressively.

Using this circular path planning method, the standoff distances vary between 522 mm and 1045 mm, owing to the aerofoil cross-section of the blade. Comparatively, the camera focal range is between 470 mm and 790 mm. Therefore, some focal blur is unavoidable in the images captured using this path when deploying a fixed

focus camera. Both the inspections with a pre-planned path and laser-based path were undertaken with the additional external lighting, permitting the camera shutter time to be set at 30 ms.

To demonstrate the accuracy of the laser scanner maintained distance, a flight path is generated in MATLAB based on the highly accurate reference model. The path is generated by slicing the mesh of the turbine blade at regular height intervals, forming a perimeter at each interval and expending the parameters to the correct standoff distance. This defines the ideal flight trajectory with 600 mm standoff distance to the blade surface. The actual UAV executed path (plotted in Figure 4.26) is recorded utilising the Vicon tracking system. The errors are calculated between the desired path and executed path and plotted in Figure 4.27, demonstrated the blade was inside camera's depth of field during the inspection. The distribution of error magnitudes demonstrates that the UAV equipped with a laser scanner successfully placed the camera within the depth of field and was able to retain this positioning while encircling the component under examination.

The raw images shown in Figure 4.28 were captured when UAV was inspecting similar areas of the blade with pre-planned trajectory and laser-based trajectory. The differences between these images demonstrate how the inspection with laser-based path was able to better maintain focus on the blade surface. More focal blurring is found on the images captured on the pre-planned circular path, the source of which is identified as the varying standoff distance during the inspection. Compared with the images from the pre-planned circular path, the textures and features on captured images during the laser-based inspection are sharper and more detailed leading to better image qualities, as shown in Figure 4.21.

The deviation maps of the model reconstructed with the pre-planned path and laser-based path are shown in Figure 4.29. The reconstruction errors from each of the two trajectories are listed in Table 4.4.

The comparison of results shows that the inspection with laser scanner had more accurate alignments and smaller measurement error than the pre-planned circular trajectory. The disparity between errors in different paths highlights the result from the laser scanner path granted a smoother surface and more precise reconstructed mesh.

The standard deviation and mean error were improved by approximately 20%, while the error ranges were reduced by a factor of 2.7. Compared with the pre-planned circular flight path, the laser scanner path-adaptation ensures that the UAV was deploying the photogrammetric measurement at a proper standoff distance in accordance with the camera's focal length. The path with the laser scanner provides better focusing on the camera so that more detailed features are resolved within the images.

Additionally, some differences are notable in the textures of reconstructed models from the two flight paths. The reconstructed model from a pre-planned path has more distorted features on the mesh (as shown in Figure 4.30(a)-(d)) because the raw images contain distortions, caused by focal blurs. Figure 4.30(e)-(h), by comparison, display the textures on the model as reconstructed from the images during the inspection that used the laser-based path. The textures on the laser-based model contain sharper and more detailed features. Discontinues and indentations were clearly reconstructed in the 3D model and are visible to varying degrees in both cases.

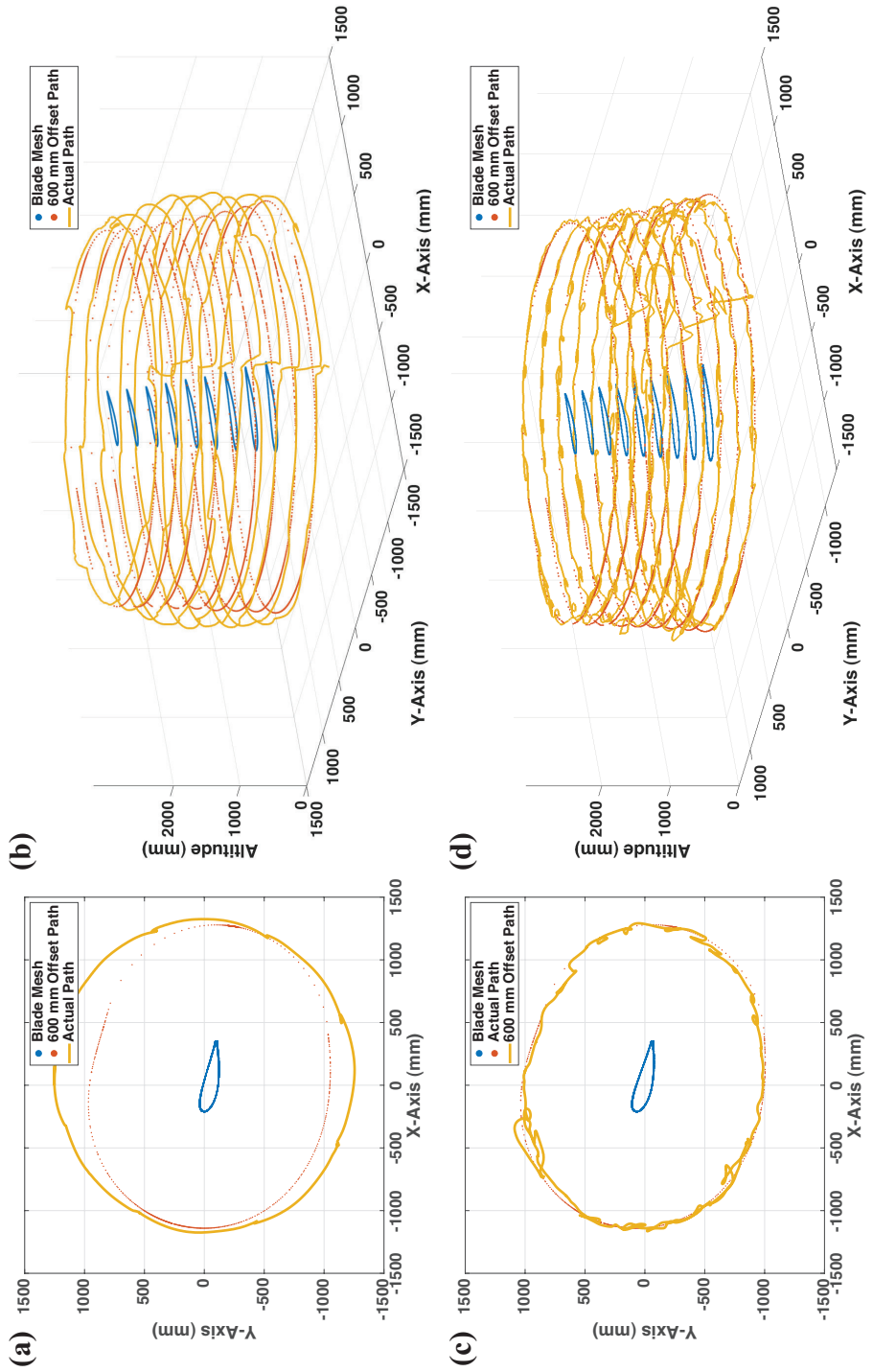

Figure 4.26: Slices of the blade mesh (blue), a MATLAB generated path with minimum 600 mm standoff distance (red) and executed path (orange). (a)(b) pre-planned trajectory (c)(d) laser-based trajectory

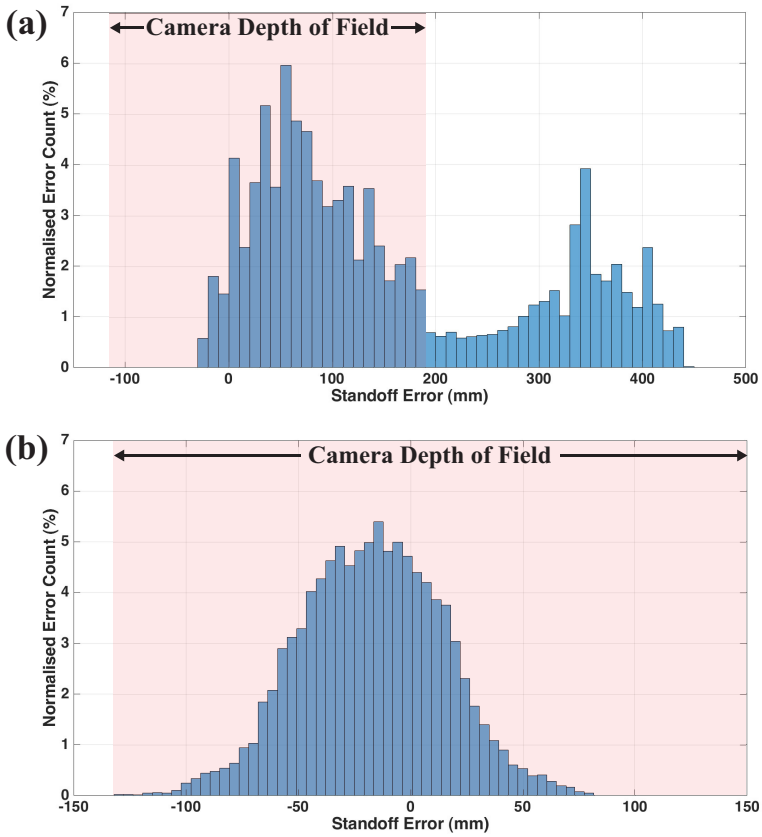

Figure 4.27: Histograms of the error between MATLAB generated path and UAV executed path (a) pre-planned trajectory (b) laser-based trajectory. The camera depth of field is asymmetric with reference to the zero standoff error, as described in Section 4.4.3.

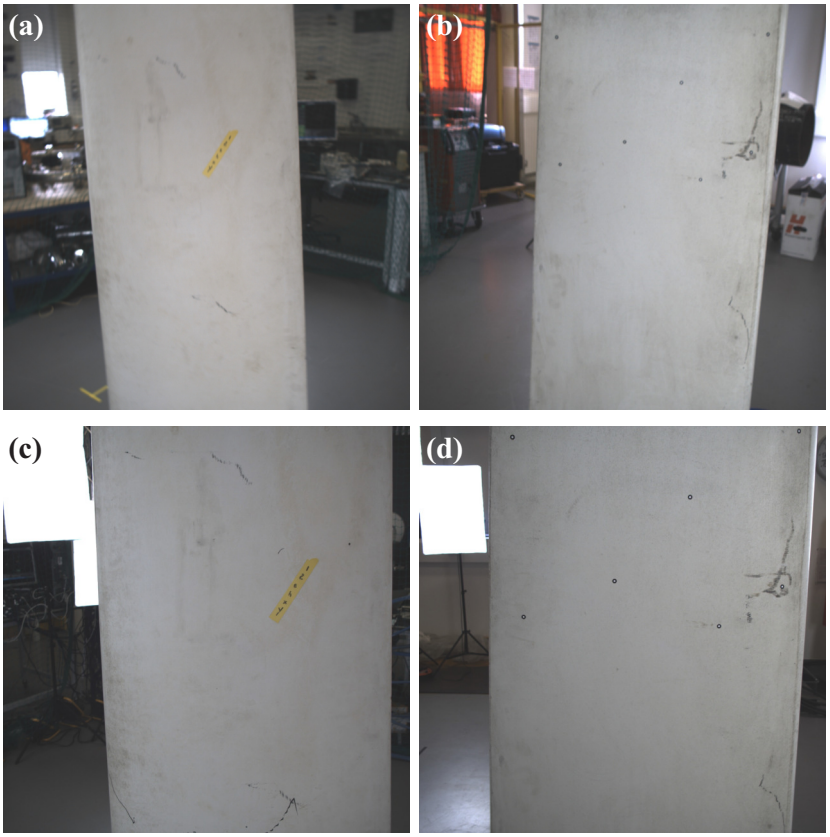

Figure 4.28: Raw images captured during the inspections. (a)(b) are captured during the inspection with the circular path. (c)(d) are captured during the inspection with the laser-based path

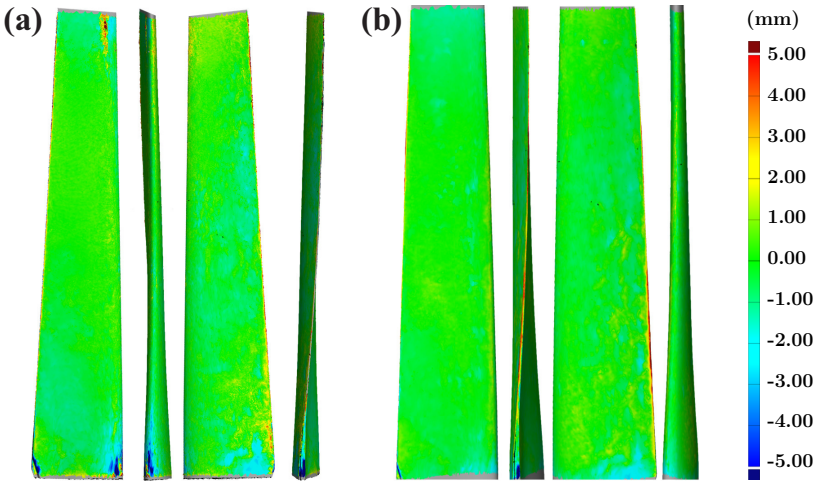

Figure 4.29: Deviation maps of the model reconstructed based on the images captured from (a) circular path (b) laser-based path, refer to the GOM model as described in Section 4.3

Table 4.4: Reconstruction errors from the inspection with the circular flight path and laser-based path, refer to the GOM model as described in Section 4.3

	Mean Error (mm)	**Standard Deviation (mm)**	**Error Range (mm)**
Circular (30 ms shutter time, Light = 200 lx)	0.3853	1.56	13.56
Laser-based Path (600 mm laser-controlled standoff distance, Light = 200 lx)	0.3098	1.29	5.09

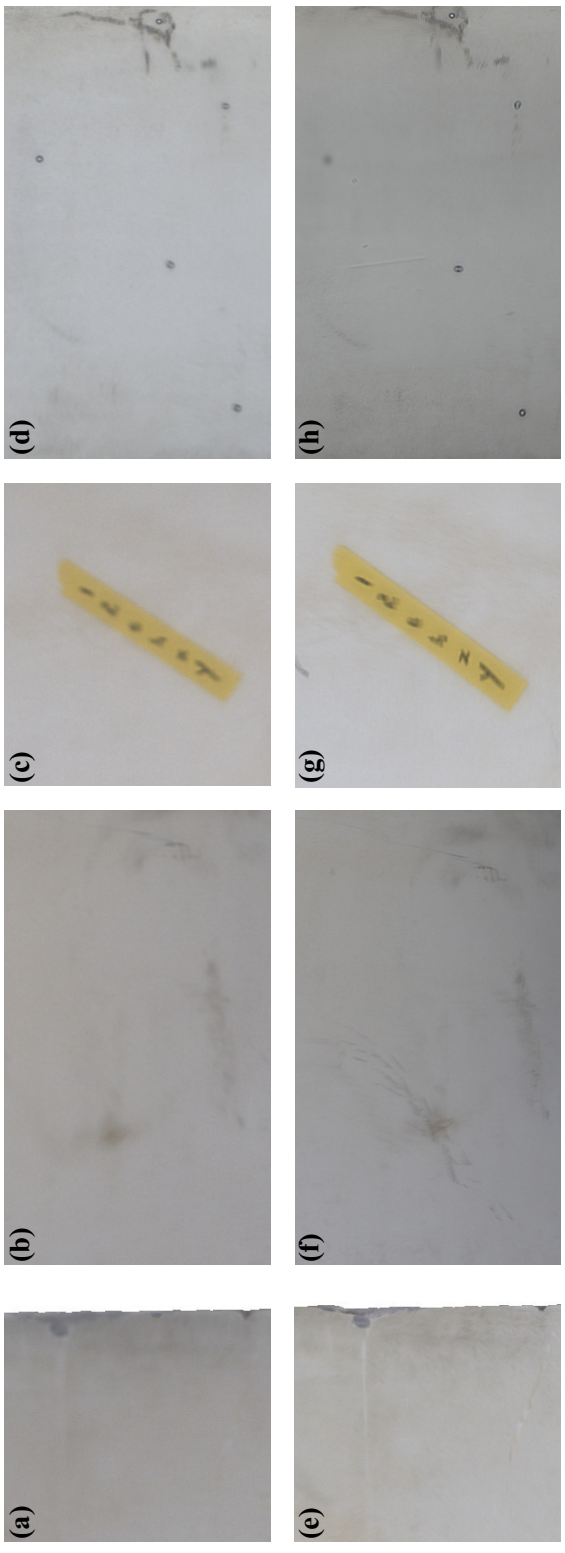

Figure 4.30: Textures on the reconstructed model (a)-(d) 3D model is reconstructed based on the images captured with circular flight path (e)-(h) 3D model is reconstructed based on the images captured with the laser-based path

4.5.2 Standoff Distance

Standoff distance between the target object and UAV onboard camera impacts the details of texture, depth of field and image quality. These parameters relate to the reconstruction process and model accuracy. During the inspection, a greater standoff distance provides a larger depth of field wherein the object remains more suitably in focus. In turn, the greater standoff distance also offers the camera a broader field of view to capture larger areas of a structure's surface in a single image. Thus, the UAV requires a shorter time to inspect the complete structure, saves flight time and increases inspection efficiency. Additionally, the image processing time during reconstruction is reduced because fewer images are generated during the shorter inspection. However, compared with an inspection conducted with a small standoff, the texture details are sacrificed as the result of lower pixel density and diminished ability to spatially resolve features.

To directly quantify the impact of standoff on reconstruction accuracy, successive inspections were undertaken at three standoff distances (400 mm, 600 mm and 800 mm), with the camera focusing optimised according to the corresponding distance. In all cases, the standoff distance was maintained utilising measurements from the laser scanner. The scanner measures the distance between the UAV and the turbine blade, generate real-time adaptive UAV flight path. The experiments were undertaken with the supplementary external lighting, permitting the camera shutter time to be set at 30 ms. The resultant reconstruction accuracies from the models generated at each of the three standoff distances are listed in Table 4.5. The image qualities attainted at the three standoff distances are plotted in Figure 4.21.

The reconstruction errors from different standoff distances highlight the trade-off between the reconstruction accuracy and UAV standoff distance. As shown by the error range, standard deviation and mean error respectively, the model using 400 mm standoff distance is more accurate, smoother and better aligned with

Table 4.5: Reconstruction errors from the inspection with three standoff distances (distance maintained by the laser scanner), refer to the GOM model as described in Section 4.3

	Mean Error (mm)	**Standard Deviation (mm)**	**Error Range (mm)**
400 mm standoff distance (Light = 200 lx)	0.2442	0.92	4.30
600 mm standoff distance (Light = 200 lx)	0.3098	1.29	5.09
800 mm standoff distance (Light = 200 lx)	0.3962	1.30	9.13

the GOM reference model (described in Section 4.3) than that using the 800 mm standoff. The mean error and error range were reduced by a factor of two. The standard deviation shows how the reconstructed surface became smoother with the reduction of standoff distance.

Additionally, the results present the mean alignment errors were approximate to the Object Space Resolution in the corresponding standoff distances. The values are 0.2286, 0.3148 and 0.4010 mm with 400, 600 and 800 mm standoff distance respectively, calculated by [192]:

$$\rho = \frac{d}{f} \times D \tag{4.6}$$

where ρ, d, f, D denote Object Space Resolution, pixel size, focal length and working distance, respectively.

Smaller Object Space Resolution correlates to better and more detailed textures captured by the camera. Tuning three parameters in Eq. (4.6) can reduce the value of objection space resolution and reconstruct a more precise 3D profile. Changing the pixel size and focal length requires to purchase new inspection hardware. The working distance can be reduced while the UAV flying closer to the

target object. This approach does not require new hardware, but it will increase the risk of the collisions and destabilise the aircraft as the results of near-surface aerodynamic challenges.

Figure 4.21 demonstrates the image sets taken from 400 mm standoff distance exhibited large variation in image quality expressed in terms of the matching feature density metric. It highlights the trade-off between the variation and UAV standoff distance. The shorter standoff distance entails that more details are taken from the surface of the inspection object. However, it also causes a narrower depth of field of the camera, requiring a tighter control of UAV position and leading to additional focal blurring, as discussed in Section 4.4.3, manifesting in Figure 4.21 as increased variation in image quality. Furthermore, the UAV was observed to be unstable when flying at 400 mm standoff owing to near-structure aerodynamic effects, causing further motion-based blur to appear in the images. In progressing from 800 mm to 600 mm and 400 mm standoff distance, the standard deviation of error in the flight path changed from 23.96 mm to 24.55 mm and 29.87 mm. Again, this indicates an exponential degradation that imposes limits on the minimum standoff distance where at a UAV photogrammetric inspection can be safely and practically conducted.

4.6 Image Background Features

The camera captured images of the entire measurement volume, whereas photogrammetric inspection only interests the assets located at the centre of the volume. During the outdoor inspections, the background is the sky so that the images contain fewer background features. Unique features are known as the critical component during the Structure of Motion, as described in Section 4.2. To demonstrate the contributions of the background features in the current reconstruction process and mimic the images from the outdoor inspections, the

images captured indoors were pre-processed to remove these backgrounds before the reconstruction.

The UAV onboard laser scanner gives the 2D boundary of the asset in the laser field of view. Presume the camera and the laser scanner have the same orientation so that the sensor data can be integrated to estimate the boundary of the asset in the camera field of view. Therefore, the background outside the boundary can be removed based on the laser scanner. The system schematic is shown in Figure 4.31.

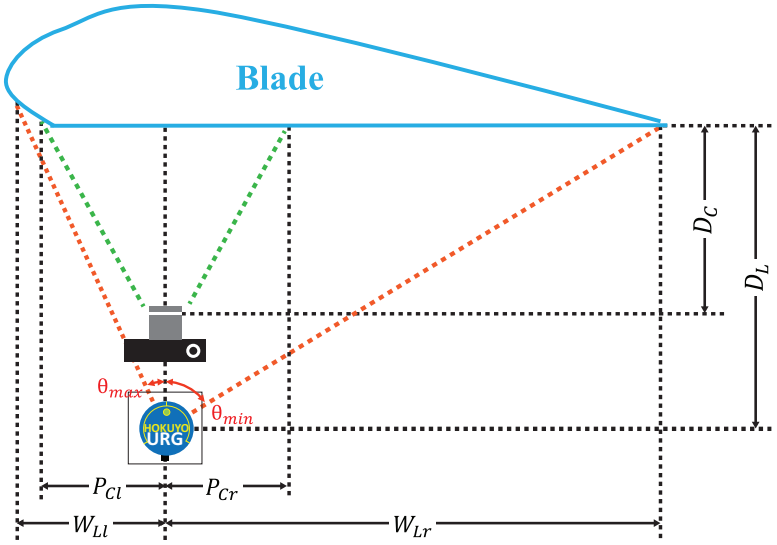

Figure 4.31: Schematic diagram of background feature removal based on the laser scanner outputs

Firstly, the system is split into two parts from the laser centre. The widths of the target on the right and left of the UAV are calculated from the equation:

$$\begin{aligned} W_{Lr} &= \tan(\theta_{min}) \times D_L \\ W_{Ll} &= \tan(\theta_{max}) \times D_L \end{aligned} \tag{4.7}$$

where two angles θ_{min} and θ_{max} are the degrees of angles reflecting the edges of the asset (described in Chapter 3) and D_L is the standoff distance between the laser scanner and the asset. The widths W_{Lr} and W_{Ll} are in mm and converted to the number of pixels P_{Cr} and P_{Cl} by the camera's Object Space Resolution (as

described in Eq. (4.6)):

$$P_{Cr} = W_{Lr}/\rho$$
$$P_{Cl} = W_{Ll}/\rho \tag{4.8}$$

where D_C denotes the distance between camera and assets. When the UAV standoff is 600 mm, the Object Space Resolution (ρ) is 0.3148 mm.

The rectangular boundary of the asset captured by the 4 MP camera is assumed as $(1000 - P_{Cr}, 0)$ to $(1000 + P_{Cl}, 2000)$, calculated by the combination of the pixels on both sides of the images. Since the scanner is physically mounted above the camera and 2D maps the blade in a horizontal plane, its output cannot fully represent the boundary of the target object in the vertical plane. Therefore, the boundary is extended by 400 pixels to avoid feature lost at the edge of the laser boundary. An illustrative example of the image cropping is shown in Figure 4.32. The process is composed of two steps: (1) the algorithm created a rectangular boundary (green box) based on the laser distance measurement (red line). (2) Extend the boundary by 400 pixels and remove the pixels outside the new boundary (blue box). The result image is shown in Figure 4.32(b).

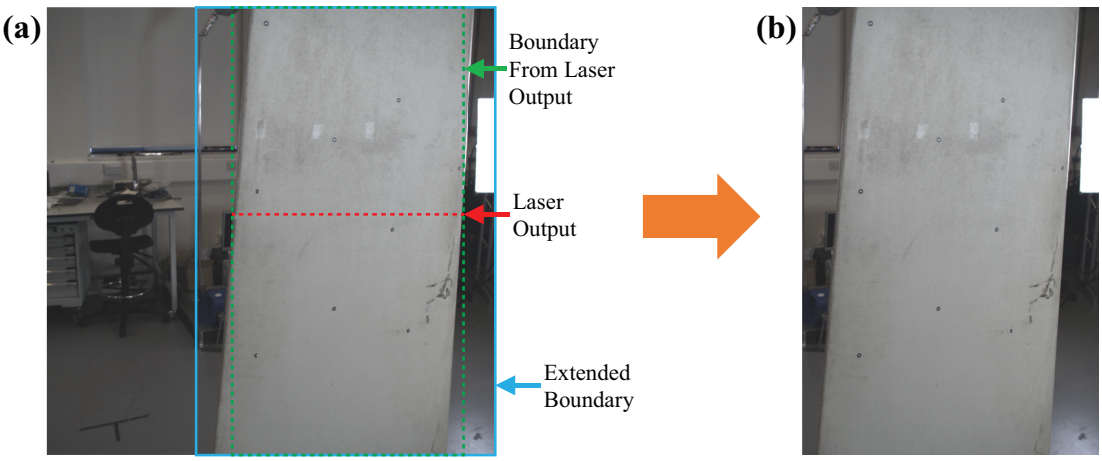

Figure 4.32: Process of image crop (a) raw image (b) post-processed image

The cropped images were processed in Agisoft software to reconstruct a 3D profile. However, the reconstruction was not completed, as a result of circa half of the

images were misaligned. The top section of the wind turbine blade was misaligned, while the software failed to estimate the image position captured at the bottom section of the blade.

The algorithm for camera alignments in the software relies on the feature matches from two images, as described in Section 4.2. Figure 4.33(a)(c) are the feature matching pairs from two cropped images, produced by the Agisoft software. By comparison, Figure 4.33(b)(d) present the matching pairs from two raw images. Red lines in Figure 4.33 are the invalid pairs after passing through the feature matching validation algorithm, which is intended to remove the biased matching pairs. Blue lines are valid matches for camera position estimation. It is apparent from Figure 4.33, cropped images and original images have similar amounts of primary matches (1199 features from post-processed images versus 1432 features from original images). However, the original images include more valid matches, whereas the algorithm completely filtered the matches from cropped images. Additionally, as shown in Figure 4.33(d), the feature matches on the side of the turbine blade are using more features from the background. Since these backgrounds were removed, the number of the valid matches significantly reduced, as shown in Figure 4.33(c). This presents the constraint of the current reconstruction algorithm and pipeline. Therefore, it should be concerned that the inspection accuracy might be influenced while conducting the photogrammetric inspections at a place without abundant background features. Further researches were conducted to demonstrate the impacts on further reconstruction procedures. To isolate the impacts on the alignment stage, the original images were initially utilised in alignment stage to estimate the image positions. Then, these images were replaced by the cropped images for denser points cloud and mesh generation. The resultant mesh demonstrated the software successfully built the same accuracy level of the 3D mesh, whereupon the background features only impact the alignment stage.

Therefore, the impacts of background features can be managed by integrating image positional information into the alignment estimation. However, since the Agisoft is commercial software, its source files are not open-access, and thereby this work is not straightforward in the Agisoft. This integration work is investigating in an on-going research project, which will deliver a more precise and more robust reconstruction pipeline.

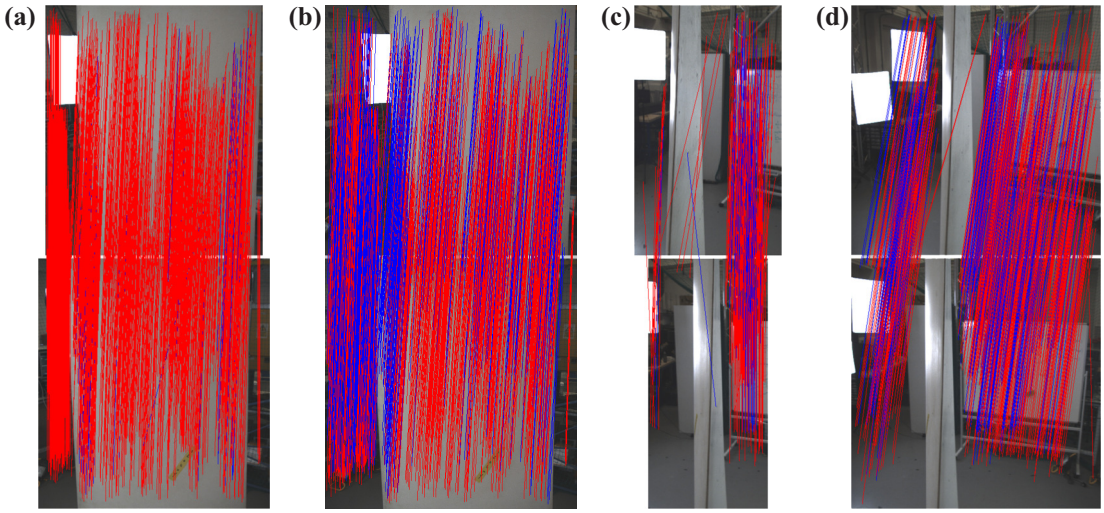

Figure 4.33: Agisoft features matches of the images captured at the side of the blade (a) cropped images (b) raw images, and the images captured at the trailing edge (c) cropped images (d) raw images. Red and blue lines denote invalid and valid feature matches, respectively

4.7 Texture Processing for NDT

The photogrammetric inspection presented in this chapter provides a 3D overview of the target object, a grateful utility to reduce the inspectors' workload. Deformation can be quantified by the mesh comparison versus the ground truth model. Scuffs and defects on the surface can be quickly located from the textured mesh. However, the identification of these discontinuities is still relying on a human expert to visually review the reconstructed model and manually mark the positions. To further build an autonomous inspection system, it is useful to

implement an autonomous and classification algorithm to highlight the scruffs and discontinuities on the 3D mesh, which will further reduce inspectors' workload, lessen the impacts of the human errors and improve inspection accuracy.

Figure 4.34: The image processed in MATLAB. The algorithm highlighted the areas having large standard deviations

Autonomous feature extraction and classifications have been presented in many literature. Hutchinson et al. implemented crack identification on the concrete bridge using the wavelet transform and Bayesian decision [199]. A threshold segmentation method is demonstrated by Wu et al., which detects the surface defects on the rail tracks from the UAV images [200]. Wang et al. deployed a Haar-Like feature extraction, coupled with Cascading Classifier to automatically classify the cracks from the images captured during the wind turbine blade inspections [156]. These approaches successfully detected and classified the discontinuities from the offline images. But these methods are complicated and designed for conventional inspections, which evaluate the structural health condition from multiple offline images. Therefore, each image is required to be carefully analysed to achieve sufficient inspection accuracy.

Figure 4.35: Enhanced 3D reconstruction model while the potential discontinuities were highlighted in red

Environment lights, image blurring and backgrounds can bias the extraction algorithms leading to the error on the inspections. To address this problem, Wang et al. manually picked a set of images and trained an artificial intelligence system to preliminary identity the cracks [156]. Similar approaches are seen in [201], using a neural-network to enhance evaluation reliability. These solutions provide accurate identification results but requiring computational resources for image processing.

The inspection results herein are 3D profiles, reconstructed and rendered from multiple images. Thus, the discontinuities identification on a single image can be simplified with a small level of error tolerance. Presume the defects are visible in

various camera views. If the algorithm incorrectly identified the discontinuities on a single image, these discontinuities are still visible and can be identified in the subsequent images. The final inspection results are presented in a 3D reconstructed model, which is produced by a rendering algorithm to mix the features from the images captured in different poses. The texture rendering algorithm in Agisoft utilises the mean value from corresponding images. Thus, the incorrect identifications were naturally filtered during the texture rendering.

The progress of the extraction algorithm utilised in this section is demonstrated in the following. Firstly, the algorithm decomposes a single image into four hundred 100×100 pixels sub-images. Then, the standard deviations in three colour channels are calculated. The sub-image with large standard deviation is considered as the region potentially containing discontinues, and will be highlighted in red. Figure 4.34 shows an example of the processed image, including the highlighted discontinues. The post-processed images were imported into the Agisoft software for texture rendering, shown in Figure 4.35. As shown in the figure, the artefacts and indentations were successfully marked on the textured model.

4.8 Discussions

The main contributions of this chapter are the implementation of a photogrammetric payload on the aerial platforn and quantifying the parameters influencing the photogrammetric inspection accuracy. The autonomously controlled UAV system successfully deployed the camera with the pre-planned trajectory and the adaptive flight path generated by the miniature laser scanner. The integrated system was deployed to undertake photogrammetric inspection of a wind turbine blade section within a laboratory environment. Inspection results are presented as a 3D reconstructed model generated from the images taken during the UAV flight. Using this system, the mean error of the reconstructed model under optimised

conditions is below 0.25 mm, the error range is less than 4.3 mm, and the standard deviation is below 0.92 mm when compared with a ground-truth, metrology grade reconstruction.

This chapter further analysed and quantified the impacts of different factors on the photogrammetric inspection accuracy when carried out using the UAV agent. It has been shown that the lighting conditions, motion blur and focal blur are parameters that negatively impact the accuracy of UAV based photogrammetric inspection. The detrimental effects of these parameters, however, can be lessened by the use of appropriate experimental setups. External lighting and longer shutter time introduce more illuminance to the camera, which improves image brightness and quality. As presented in Figure 4.21, these improvements increased the reconstruction accuracies and significantly reduced the model errors. The comparisons between manual inspection and autonomous inspection show the motion blur increased the reconstruction error by a factor of two. Focal blur is introduced due to the narrow depth of field during the close-range inspections. The laser scanner maintained the standoff distance and significant error reductions are observable in the reconstructed models and associated data. With the laser scanner, the inspection was successfully conducted while maintaining the position of the object's surface within the camera's depth of field. Here, captured images were sharper and had better quality under the proposed matching feature density metric, as shown in Figure 4.21. The reconstructed model in this case is more accurate than the pre-planned path and has better-detailed textures.

As described in Section 4.5.2, the reconstruction error was found to reduce with the shorter standoff distances, which improves the resolution and provide the capability for the camera to capture more detailed surface. Although the inspection with 400 mm standoff distance had the most accurate reconstruction model in this chapter, the UAV flight was seen to be unstable during the inspection due to the near-surface aerodynamic effects from the wind turbine blade structure. Compared with the inspection at 800 mm, the model from 600 mm standoff was

more accurate and had a smaller error range. Therefore, 600 mm is identified as the optimal standoff distance for the UAV photogrammetric inspections conducted in the manner described herein.

During outdoor inspections, a better environmental brightness can be leveraged to extend the camera depth of field via utilisation of a smaller camera aperture, resulting in the images with less focal blur. However, as shown in Figure 4.24, the image had the best quality at the camera focal point (in that case 600 mm). The reduced aperture size only serves to widen the depth of field wherein acceptable images may be captured. While it is still necessary to perform the inspection with a smaller standoff to obtain the spatial resolution required for more detailed features even with an extended depth of field, a smaller aperture will reduce the level of UAV position control required and make better allowance for environmental position disturbances commonly induced by wind outdoors. Maintaining a relatively constant standoff is, thus, still necessary for outdoor inspections but presents additional challenges. Typical outdoor navigation systems employed are less accurate than the indoor system. The position noise in such sensors can lead to flight instability and introduce the motion blur without proper compensation, further increasing the limit on minimum standoff distance. As described in Section 4.4.2, such impacts can be lessened by the use of shorter camera exposure time, since daylight can introduce more illumination on the camera in certain conditions. Such camera setting adjustments require the balance between the camera shutter speed and aperture size. Hence, the findings from this paper may be applied during the outdoor inspections and used to inform inspection configuration and planning in the presence of poorer environmental conditions. In addition, the laser scanner herein offers real-time adaptive corrections of less accurate navigation systems, and thereby represents a means through which the standoff to the target object can be maintained within the camera depth of field during outdoor inspections.

In Section 4.6, the algorithm based on laser scanner data was demonstrated to remove the background features from the raw images. The reconstruction process was incomplete in the Agisoft software by using these cropped images without background features. Further analysis shows these background features were only impacted the Agisoft software in the alignment procedure. The same level of accuracy was achieved by using these background removed images with the image positions calculated by their original images. Thus, the laser scanner data and Vicon position data should be considered to be integrated into the alignment procedure in future research. This will help to estimate image positions while conducting the outdoor inspections with fewer background features.

The texture extraction was presented in Section 4.7 to demonstrate the future potentials for more efficient NDT inspections. The images were processed through the discontinuity detection algorithm, which highlighted the areas with large standard deviations. The indentations and discontinuous as well as the artefacts were successfully highlighted on the rendered 3D mesh. This provides an approach to enhance the texture on the 3D model and assist inspectors in making decisions. It can be cooperated with neural-network based classification algorithms to highlight defects on the mesh with different colours based on defect categories, and thereby further reduce human errors.

Chapter 5

UAV-Deployed Autonomous Ultrasonic Inspections

5.1 Introduction

Chapter 4 presented a UAV-deployed photogrammetric inspection, which positioned the camera at a small standoff distance to avoid collisions and near-surface aerodynamic challenges. Such non-contact measurements can identify visible discontinuities and other prominent surface-exposed defects rapidly. However, these non-contact measurements are only capable of identifying prominent surface-exposed defects. Additionally, the accuracy of visual inspection is influenced by environmental conditions and inspection setup.

Structural health conditions, such as internal support material corrosion and fatigue crack formation beneath an outer surface coating, require contact-based measurement technologies. This remains problematic, as current UAVs fly only at comparatively large standoff distances from the target object. It is also highly challenging to manually pilot a UAV with sufficient accuracy to perform a close-range inspection, whilst maintaining appropriate contact force and alignment

for a conventional transducer to operate successfully. To this end, Mattar et al. demonstrated a prototype wall-sticking, manually piloted UAV for ultrasonic corrosion mapping of metallic storage tanks [202]. An ultrasonic transducer, accompanied by an electromagnet, were mounted at the tip of an extended arm. The pair utilised an onboard microcontroller for the electromagnet and generated 530 N of adhesive force to ensure the ultrasound probe remained in stable contact and acoustically coupled to the tank wall. However, the system was only capable of conducting thickness measurements of ferromagnetic structures. Other non-magnetic materials, such as aluminium, could not support the required adhesive force. A further attempt at UAV-deployed ultrasonic inspection was presented by Jarvis et al., with an EMAT (Electromagnetic Acoustic Transducer) placed onto two industrial samples (a ferromagnetic plate and pipe) with a manually piloted UAV [203]. The wall thicknesses of these two samples were measured with a limited success rate: 65% in the case of the plate, dropping to 60% for the pipe. Unsuccessful deployments occurred when the landing trajectory was not perpendicular to the target surface. Currently, UAV-deployed ultrasonic thickness measurement systems are being prototyped by a selection of industrial inspection companies [204, 205]. Most current literature is focused on the measurement of ferromagnetic structures, whereas the industrial world contains significant infrastructure composed of non-magnetic materials (e.g. aluminium, titanium, and a variety of composites). These materials lack the susceptibility to magnetic force necessary to ensure the transducer remains on the inspection surface.

This chapter presents the UAV platform, as described in pervious chapters, equipped with an ultrasonic thickness measurement payload. The system was autonomously stabilised and guided for ultrasonic inspection of large metallic storage vessels and other non-magnetic industrial assets. A laser scanner onboard the UAV determined the craft's standoff distance and alignment offset relative to the inspection surface, while measurements were obtained using a 5 MHz split-crystal ultrasonic transducer and on-board ultrasonic transceiver circuitry.

To enhance the transmission of ultrasonic energy into the sample, a small quantity of couplant gel was applied between the transducer and inspection surface, as is common in conventional inspection. The transducer itself was held in a spring-loaded mounting structure to ensure appropriate contact was maintained while the UAV manipulated its thrust to provide the force that coupled the probe with the surface. Employing this strategy, the UAV autonomously measured thickness at pre-planned locations on the surface.

Ultrasonic thickness measurements aboard the UAV were attained by a conventional split-crystal transducer, utilising piezoelectric materials to generate and receive the ultrasonic pressure waves. The transducer operated in a "Pitch-Catch" configuration, which helped to minimise the near-field dead-zone and improved resolution when measuring thin plates [206].

However, as is discussed in greater detail below, a number of factors mitigated the performance benefits offered by this configuration when applied in the context of UAV-based inspection. Transducer alignment errors and UAV instability can cause poor acoustic coupling, resulting in high attenuation of the returned ultrasonic signals. The impact of this weakened signal amplitude was compounded by the electromagnetic noise introduced by interference from UAV motors. This raised the noise floor and caused additional reduction of the SNR, further diminishing the inspection accuracy.

Increasing the excitation voltage applied to the piezoelectric element helped to mitigate this challenge. Doing so propagated more energy into the test sample and in turn ensured that the system received stronger reflected waves. In this context, however, the increased voltage increased the challenges for transceiver circuity design, which was required to handle a kilovolt power supply. Therefore, a more elegant solution was sought through coded excitation to increase the SNR within the UAV thickness measurement system. Coded excitation has previously been demonstrated within medical and laser ultrasound applications [207, 208]. It

consists of a series of bits coded as ± 1, where the priority of the excitation voltage is varied in the excitation sequence. Coded excitation improves the received SNR by increasing the time-bandwidth product without increasing the amplitude of the excitation voltage applied to the piezoelectric material, which is suitable for the UAV system. The Golay and Barker encodings are two types of binary sequence commonly applied to ultrasonic excitation [208, 209]. Golay code excitation contains a pair of sequences, coded with two different polarity patterns. The two complementary signals received after the transmission of the coded sequences contain different wave patterns, such that the sidelobes present in the resultant signal can be suppressed by summation. An approach using the Golay excitation schema requires two measurements to be conducted in the same position and with similar coupling, which may be impractical given the challenges associated with the UAV control system and environmental disturbance rejection. Barker coded excitation is more easily implemented in this context, as it executes only one coded sequence, eliminating issues associated with small systemic changes during measurement at the expense of the sidelobe cancellation property present in Golay codes. Thus, the Barker excitation sequence was implemented in the system to improve the acquisition SNR. Details of the coded excitation will be discussed in Section 5.7.

This chapter presents a prototype UAV system for ultrasonic thickness mapping of a large-scale industrial sample and quantifies the UAV deployment parameters that influence inspection accuracy. Particular attention is paid to the detrimental effects of the aerodynamic challenges, transducer alignment constraints, and electrical interference from the craft's motors. These experimental results provide the benchmarks for the current ultrasonic inspection system, which will be crucial for future research.

The structure of this chapter is as follows. Section 5.2 and 5.3 review the prinicples and techniques of the ultrasonic inspections. Section 5.4 demonstrates the implementation of a UAV system with an integrated ultrasonic inspection

payload and details the experimental setup used to assess its performance. Section 5.5 quantifies and analyses the parameters influencing the system's SNR and inspection accuracy. Section 5.6 illustrates the results of the UAV-deployed ultrasonic inspections. Section 5.7 describes a coded ultrasound excitation, which improved the SNR of the A-scan signals. In Section 5.8, the chapter is concluded with a discussion of results and the insights gained from the work.

5.2 Principles of Ultrasound

5.2.1 Modes of Ultrasonic Wave Vibration

Ultrasound is a form of high-frequency inaudible sound, vibrating in elastic materials with a frequency between 20 kHz and 20 MHz. Depending on the material and boundary, ultrasound waves can propagate inside materials in many modes, such as longitudinal, shear, surface, and plate waves. The longitudinal waves and shear waves are most commonly seen in the ultrasonic NDT inspections [206].

A longitudinal wave is a vibration in the longitudinal direction. Since the longitudinal wave contains compressional and dilatational forces, it is also called a compressional wave [206]. It can propagate in liquids, gases, and solids. The velocity of the longitudinal wave is 6350 m/s in aluminium, 330 m/s in air, and 1900 m/s in water [210].

A shear (or transverse) wave vibrates perpendicular to the propagation direction. Because a shear wave requires an acoustic medium for effective propagation, it only exists in a solid. Based on Hooke's Law, the signal strength of the shear wave was weaker than that of a longitudinal wave.

A surface wave vibrates along the boundary between a solid and a sufficiently rarefied medium, such as air [211]. It combines the longitudinal and transverse motion, becomes elliptical motion and only vibrates within the one wavelength from the boundary. This type of wave is typically utilised to detect surface discontinuities.

A Lamb wave, also called a plate wave, is a form of surface wave, except it only exists in plates with a thickness less than several sound wavelengths [206]. The Lamb wave is a combination of the longitudinal and shear wave and propagates parallel to the injection angle, phase matching at the boundary.

5.2.2 Refraction and Mode Conversion

Refraction is a phenomenon at the boundaries of two different materials. These two materials have different acoustic impedances and wave propagation velocities. During the refraction, some parts of the waveform convert to another form, such as longitudinal waves converting to shear waves. Such a phenomenon is also called Mode Conversion. As shown in Figure 5.1, when the sound waves enter the boundary with an injection angle θ_{L1} from material 1 to material 2, part of the wave enters material 2 with refraction and the remainder of the energy is reflected. Mode conversion occurs in the reflection portion and the refraction portion. Based on Snell's Law, the relationship between the wave angles and velocities is represented by [212]:

$$\frac{\sin\theta_{L1}}{C_{L1}} = \frac{\sin\theta_{S1}}{C_{S1}} = \frac{\sin\theta_{L2}}{C_{L2}} = \frac{\sin\theta_{S2}}{C_{S2}} \tag{5.1}$$

where C_{L1} and C_{L2} are the longitudinal velocities, and C_{S1} and C_{S2} are the shear velocities in material 1 and material 2, respectively.

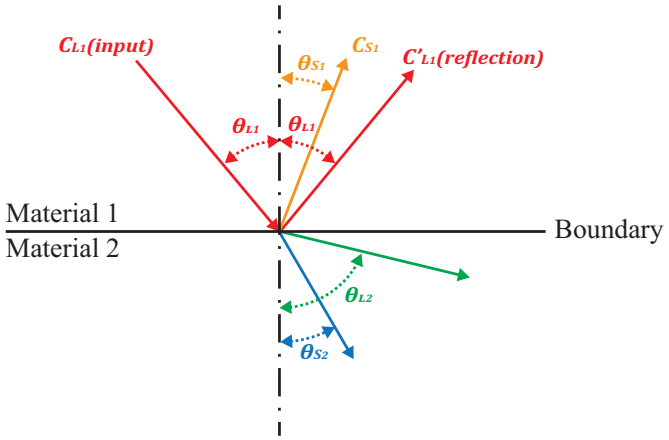

Figure 5.1: Ultrasonic wave reflection model

The shear wave angle and longitudinal wave angle in material 2 can be obtained from:

$$\begin{aligned} \theta_{L2} &= \sin^{-1} \frac{\sin C_{L1} \times C_{L2}}{C_{L1}} \ (longitudinal\ wave) \\ \theta_{S2} &= \sin^{-1} \frac{\sin C_{L1} \times C_{S2}}{C_{L1}} \ (shear\ wave) \end{aligned} \tag{5.2}$$

Assume the wave propagation velocities in Eq. (5.2) are fixed values. The longitudinal (θ_{L2}) and shear angle (θ_{S2}) are increased with the increment of the wave incident angle (θ_{L1}).

When θ_{L2} reaches 90°, the longitudinal wave becomes an interference wave or reflects into material 1. Only the shear wave propagates inside material 2. The incident angle in this scenario is:

$$\theta_{L1}{}' = \sin^{-1} \frac{C_{L1}}{C_{L2}} \tag{5.3}$$

As the incident angle θ_{S2} was increased up to 90°, all of the energy was either reflected or became the interference wave and no wave propagated into material 2. The injection angle in this scenario is expressed as:

$$\theta_{L1}{}'' = \sin^{-1} \frac{C_{L1}}{C_{S2}} \tag{5.4}$$

5.2.3 Reflection and Transmission

Boundary reflection is a phenomenon during ultrasound wave propagation between two materials with different acoustic impedances, defined as [206]:

$$Z = \rho C_L \tag{5.5}$$

where ρ is the density of the material and C_L is the longitudinal wave speed in the material. At room temperature, the acoustic impedance of air is 400 Rayl and for steel it is 46.7 MRayl. For a piezoelectric material, it is 35 MRayl [206].

The coefficient of reflected power is defined as:

$$\alpha_{R(power)} = {\alpha_{R(amplitude)}}^2 = \frac{(Z_1 - Z_2)^2}{(Z_1 + Z_2)^2} \tag{5.6}$$

The coefficient of the transmitted signal is:

$$\alpha_{T(amplitude)} = 1 - \alpha_{R(amplitude)} = \frac{2Z_2}{Z_2 + Z_1} \tag{5.7}$$

where Z_1 and Z_2 represent the acoustical impedance of material 1 and material 2, respectively.

During ultrasonic measurements, transmitting more energy into the target object can enlarge the amplitudes of the reflections, resulting in an enhanced SNR and a more accurate inspection.

5.2.4 Ultrasonic Inspection

Ultrasonic inspection is one of the NDT approaches. Detecting discontinuities under surface coatings, thickness measurements, and material characterisation are the typical applications of ultrasonic inspection.

"Pulse-Echo" and "Pitch-Catch" are two transducer configurations used during ultrasonic inspections. Figure 5.2 shows longitudinal wave testing with the corresponding A-scan time domain results.

The "Pulse-Echo" configuration, as shown in Figure 5.2(a)(b), utilises a single element probe placed on one side of the test sample, and the transducer acts as both transmitter and receiver. It converts electrical signals to mechanical sound waves and propagates the energy into the test sample. The ultrasonic echoes, reflected at the back wall and internal defects, return to the transducer. In this case, the crystal operates as a receiver, identifying and converting reflections into electrical signals.

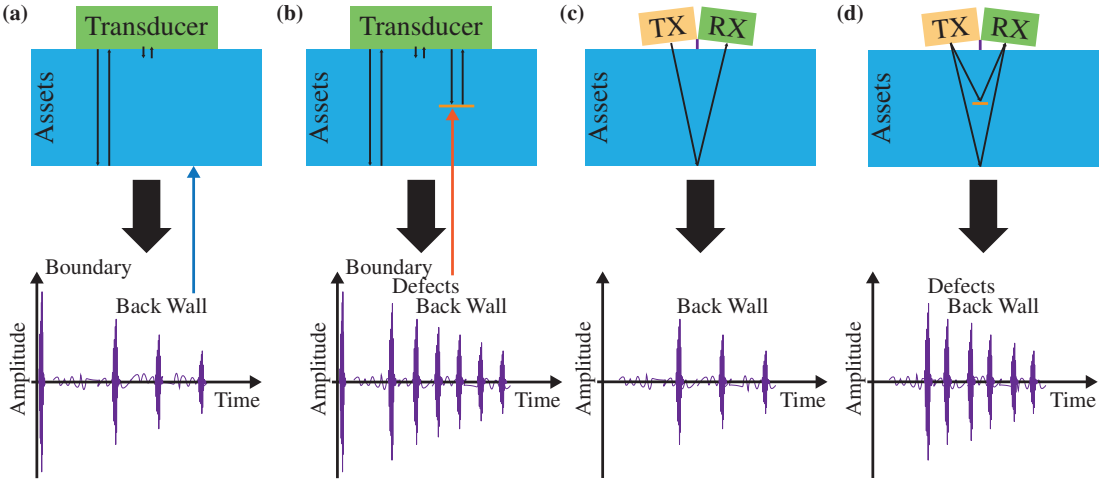

Figure 5.2: A-scan results with two typical ultrasound testing configurations: (a) Pulse-Echo configuration without a defect (b) Pulse-Echo configuration with a defect (c) Pitch-Catch configuration without a defect (d) Pitch-Catch configuration with a defect

In this configuration, defects and the back wall inside the sample reflect the ultrasonic waves, which appear as multiple echoes on the A-scan signals. The depth of the reflections can be calculated using the sound wave Time-Of-Flight as:

$$d = \frac{c \times t}{2} \tag{5.8}$$

where d is the depth of the reflections, c is the wave speed in the target object (e.g. about 6350 m/s in aluminium at room temperature), and t represents the sound wave flight time.

Additionally, the amplitudes of the echo signals are utilised to inspect the integrity of the target object. A strong back wall reflection appearing on the A-scan signals indicates that no defect was located in the wave path.

"Dead zone" is a constraint of the "Pulse-Echo" configuration. The reflection from near-surface defects and the back wall of a thin plate will arrive close to the reflection from the transducer boundary. Since the boundary reflection typically contains large energy and the transducer is still ringing when the reflections arrive, the defects located in such a zone and echoes from the backwall are hidden inside the boundary reflections and difficult to identify [206].

Figure 5.2(c)(d) shows alternative "Pitch-Catch" ultrasonic transducer configurations. The transmitter and receiver were separated into two elements. The transmitter pitched the ultrasonic signals, which were caught by the receiver. Inspection with this configuration can be achieved by two elements placed on the same side with orientation offsets for sound wave focusing (typically seen on split-crystal probes). Similar to the "Pulse-Echo" configuration, this configuration can utilise Time-of-Flight to measure the depth of the reflections. Compared with a single element transducer, this configuration has fewer impacts from the "dead zone", because the receiver and transmitter are separated. Therefore, this configuration can be utilised to locate near-surface defects and to measure the thickness of a thin plate. Additionally, it makes signal conditioning simpler in the absence of large amplitude echoes from the surface boundary. In such a configuration, the locations of two elements must be placed in the wave path with an appropriate alignment angle to catch the echoes.

5.3 Ultrasonic Transducers

5.3.1 Piezoelectric Transducer

The piezoelectric effect allows certain materials to generate mechanical vibrations in response to an applied electrical field. The electrical signals applied to piezoceramics accumulate electron movements, resulting in energy conversion from electrical signals to tension or compression force, thereby producing mechanical movements. Therefore, transducers made of piezoelectric materials, such as lead zirconate titanate (PZT), can be used as a transmitter to produce the ultrasonic waves. The transducer can also be utilised as a sound wave receiver, with the converse piezoelectric effect. The materials can be charged and discharged by an applied mechanical force, and thus the sound waves can be converted to electrical signals [206].

Conventional piezoceramics have a relatively large acoustical impedance, compared with the materials utilised during NDT inspections, such as aluminium and water. Therefore, some extra materials, including a backing layer or a matching layer, are added inside the ultrasonic transducer to provide a wider bandwidth, increased sensitivity, and improved energy transmission efficiency. Figure 5.3 shows an example of a single-element piezoelectric transducer, made by a piezoelectric element, backing layer, and matching layer [213].

Dual-element or split-crystal transducers contain two independent piezoelectric elements in a single housing, split by an acoustic barrier. One element is utilised for sound generation and the other one is used as a sound receiver. Thus, the dual element transducer is naturally configured as “Pitch-Catch”, which is less impacted by the “dead zone”.

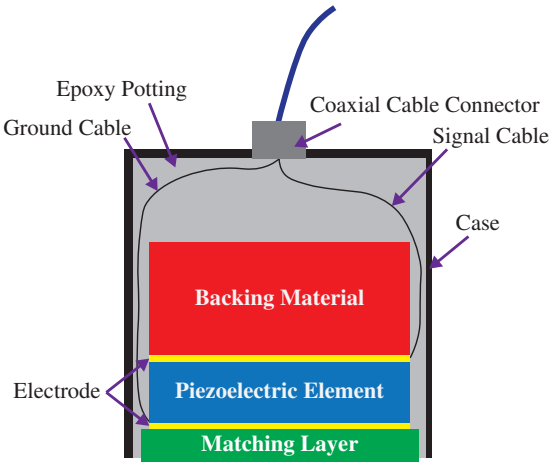

Figure 5.3: Internal structure of a single-element piezoelectric transducer

5.3.2 Air-Coupled Transducer

A traditional piezoelectric transducer requires a couplant-gel placed between the asset and transducer surfaces to eliminate any air gap, because the impedance of air is over 100,000 times smaller than that of steel. From the UAV-deployed NDT prospective, the couplant increased the aircraft's payload mass, influencing flight time. Additionally, a conventional ultrasonic inspection transducer typically requires an appropriate contact force, precise alignment angle, and a layer of couplant to conduct an accurate measurement, which is problematic in the UAV control system.

Air-coupled electrostatic and piezoelectric are two types of air-coupled transducers. Piezoelectric transducers are similar to those described in Section 5.3.1, composed of a piezocomposite disk, electrodes, and a well-designed matching layer. The piezoelectric effect inside the transducer produces the ultrasound wave and uses air as a couplant to transmit the wave into the test sample. Because air has a relatively small acoustic impedance, most of the energy is reflected at the boundary between the air and the transducer. Therefore, to maximise the transmission efficiency and propagate more energy through the air, the matching layer is placed in front of the transducer.

An electrostatic transducer, or capacitive micromachined ultrasonic transducer, is a capacitive ultrasonic transducer, composed of a conductive layer, a membrane, and a metal backplate [206]. The membrane is placed between the conductive layer and the metal backplate, working as a capacitor. The biased voltage applied to the membrane attracts the membrane to the backplate. Applying a reversed signal polarity moves the membrane to the conductive layer. Therefore, the alternate electrical signal with a desired frequency vibrates the membrane between the backplate and the conductive layer. This creates the ultrasonic wave vibrations in the air. Conversely, the sound wave vibrations in the air can be captured by the membrane and converted to an electrical signal. Therefore, the transducer can be used for signal transmitting and receiving.

Electrostatic transducers produce ultrasound waves in the air. Sound wave transmission between the air and a transducer does not suffer from impedance mismatches. Therefore, such transducers are often seen in air-coupled measurements [214].

The non-contact and dry-coupled nature of an air-coupled transducer provides flexibility ideal for remote inspections of targets with water-incompatible materials [215]. However, air-coupled ultrasound often suffers from poor SNR, due to the impedance mismatch at the air boundaries. Compared with a conventional ultrasonic transducer, the air-coupled transducers inevitably attenuate the signals by as much as 168 dB, whereas the coupling loss was calculated as 31 dB in water [216]. Moreover, the transmitter and receiver require precise alignment to ensure a suitable SNR for accurate measurements [9].

5.3.3 Laser-Generated Ultrasound

A laser-generated ultrasound transducer utilises a laser source to first heat or ablate the sample surface [206]. The absorbed optical energy is then converted

to an elastic wave on the surface and propagated into the sample by thermal expansion. The thermoelastic and the ablative regime are two typical regimes of laser-generated ultrasound. If the laser power is below the melting point of the surface, the generation regime is called the thermoelastic regime. Conversely, if the surface temperature is heated to above the material's melting point, the generation regime is called the ablative regime. To conduct non-destructive testing, laser power must be controlled to prevent material ablation. It typically requires two separate laser transducers, one to ablate the surface and produce the ultrasonic wave, and the other as a laser interferometer, detecting the surface movements as the results of the reflections from internal structures.

Since the laser-generated ultrasound does not require a transducer contact surface for generation, such transducers can be deployed at a relatively large standoff distance from the target object, providing speed inspections and minimising the near-surface challenges of UAV control. However, the mass of laser-generated ultrasound transducers cause unsuitable conditions for the aerial platform, as described in this thesis [217].

5.3.4 Electromagnetic Acoustic Transducer

An Electromagnetic Acoustic Transducer (EMAT) uses the electromagnetic acoustic effect to transmit and receive ultrasonic waves. A typical EMAT contains two major parts: a permanent magnet and a coil, located between the magnet and the sample surface. When the electrical signals with a specific frequency pass through the coil, an oscillating magnetic field with an eddy current is produced near the asset surface. A static magnetic field, generated by a permanent magnet inside the transducer, creates the Lorentz forces to vibrate electrons on the sample surface. Such electron vibrations lead to mechanical vibrations inside the asset. The reverse effect is used to convert ultrasound waves to electrical signals.

Such transducers are capable of performing rapid inspections under high-temperature conditions [218]. However, EMAT is limited to conductive materials. Non-metal materials, such as concrete or glass fibre, cannot produce the required magnetic fields for inspection. The coil inside the transducer requires significant power to generate a sufficient magnetic field on the test sample, which is not efficient for UAV-deployed inspections.

5.3.5 Ultrasound Wheel Probe

Ultrasound wheel probes are pulsed-echo dry-coupled ultrasound transducers, which do not need liquid couplant placed between the probe and the sample surface. There are two forms of ultrasound wheel probe: dry-coupled [219] and liquid filled arrays [220], shown in Figure 5.4. The ultrasound transmitter and receiver are placed inside the wheel probe and kept perpendicular to the test surface. The sound waves are generated by the transmitter inside the probe and pass through a well-designed rubber tire. The reflected wave traverses the rubber tire and is captured by the receiver inside the probe.

The wheel probe's flexibility lends itself to autonomous inspection. Eddyfi offers two industrial dry-coupled wheel probes, TWP25 and TWP40, installed on many autonomous industrial inspection robots [219]. The wheel probe installed on Scorpion2 was utilised to conduct remote inspections of the tank shell. To perform an accurate inspection, the wheel probe required a relatively large contact force applied to it in order to eliminate the gap between the transducer and the rubber wheel. Compared with a single element probe, an array ultrasonic wheel probe [220] covers a larger area.

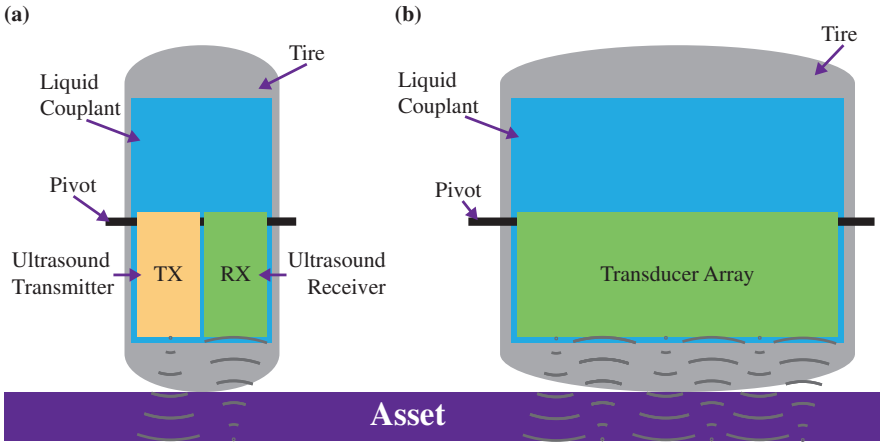

Figure 5.4: Two types of wheel probe (a) single channel, dry-coupled wheel probe (b) liquid-filled, array probe

5.3.6 Summary

The primary considerations during transducer selection for the UAV-deployed ultrasonic inspections were the dimensions, flexibility, mass, power consumption, and SNR. Laser-generated ultrasound, EMAT, and dry-coupled transducers provides flexibility in the absence of a liquid couplant placed between the surface and transducer face. However, the added mass negatively impacts UAV flight time. Additionally, the magnetic field generated by such electromagnetic transducers could introduce interference to the UAV flight control system.

Although the dry-coupled wheel probe does not require a liquid couplant, an appropriate contact force is required to eliminate the air gap for sufficient SNR. More than 20 N force is required, while the probe is ideally aligned to a bright-polished surface (surface roughness $R_a = 0.19$ µm). The required force is increased by a factor of two, while inspecting a satin-polished surface (surface roughness $R_a = 0.47$ µm) [221]. This is a significant challenge from a UAV control perspective. SNR is also a constraint in an air-coupled transducer, due to the impedance matching and precise alignment requirements [9]. Therefore, the conventional piezoelectric probe is the best choice of transducer payload for the current UAV-deployed ultrasonic inspections.

5.4 Overview of the Ultrasonic Inspection System

The inspection system described in this chapter (as shown in Figure 5.5) is composed of: the aerial platform presented in Chapter 2 and Chapter 3, a custom manufactured ultrasonic transceiver circuitry and a 5 MHz, 10 mm diameter spilt-crystal ultrasonic transducer [20] installed at the tip of the spring-loaded arm.

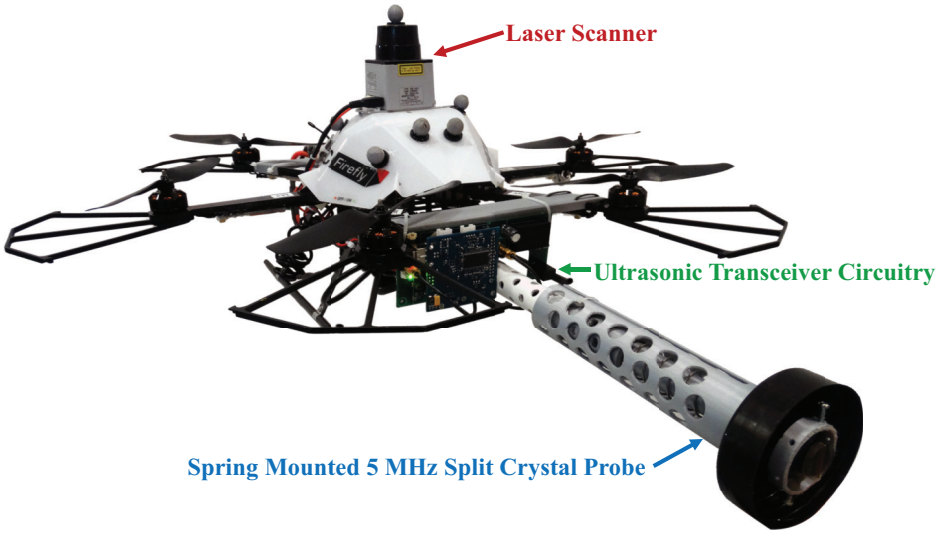

Figure 5.5: AscTec Firefly UAV equipped with ultrasonic payload

Ultrasonic thickness measurement is attained by deploying a 5 MHz, 10 mm diameter, split-crystal transducer, accompanied with customised ultrasonic transceiver circuitry. The transducer is commercially available, manufactured by GB Inspection with an optional plastic cladding that reduces its mass to 17 g [20]. Like most hard-face transducers, it requires appropriate angular alignment and utilises acoustic couplant gel, placed between the asset and transducer surfaces, to eliminate any air gap.

The customised ultrasonic transceiver circuitry is a 76 g, light-weight system, specifically designed to minimise the mass of the hardware necessary to oper-

ate split-crystal ultrasonic probes within small robotic platforms. The system contains a pulse generator; a Variable Gain Amplifier (VGA); an Analogue to Digital Converter (ADC) for digitising A-scan echo signals and a high-speed Field-Programmable Gate Array (FPGA) controller for data acquisition and buffering the A-scan signals before sending to the onboard computer.

The ultrasonic payload offers the capability to generate ± 12 V bipolar or 180 V unipolar rectangular pulses, stimulating the piezoelectric element inside the transducer, and thus effects the transmission of ultrasound waves. Empirical trials with both the low voltage bipolar and high voltage unipolar excitations demonstrated the same SNR with transducers positioned at the optimal alignment angles. A transimpedance amplifier, coupled with the VGA, forms the receiver front end to pre-process the ultrasonic echo signal so that it will be compatible with the ADC. The amplified signals are then digitised at a sampling rate of 100 MHz by the ADC and initially stored in the FPGA memory to reduce computer processing requirements. The system resolution depends on the speed of sound in material. The resolution is 0.03 mm while inspecting an aluminium asset. These signals are then wirelessly transmitted via the UAV's onboard computer to a ground-based workstation for further processing to provide the final quantitative A-scan thickness measurement. Additionally, the FPGA offers the capabilities to adjust the gain of the VGA and vary the excitation pulse width without manual hardware modification. The software running within the UAV onboard computer fires the transducer and ultimately controls the acquisition process, providing a 20 Hz pulse repetition frequency.

The AscTec Firefly is designed as a research platform for non-contact evaluations, particularly for photogrammetric inspection with a lightweight camera. However, unlike photogrammetry, ultrasonic inspection is a contact-based measurement, which requires the transducer to meet the inspection surface with appropriate force and alignment to ensure adequate coupling of the transmitted and received acoustic energy. Because of aerodynamic challenges and concerns regarding collisions, the

UAV is required to maintain a small distance between the propeller swept area and the inspection surface. Therefore, the ultrasonic transducer is held at the tip of a spring-loaded arm extending from the centre of the UAV.

This is not without compromise. The presence of this arm and transducer act to increase the UAV mass and its distribution, introducing a significant pitching moment (the product of force and distance to the UAV's centre) and so act to destabilise the aircraft. Thus, the mechanical mounting structure was designed to minimise the increase in payload mass and turning moment. The structure (depicted in Figure 5.5) is composed of a central tube, a spring-loaded head, a UAV mounting manifold and a battery carriage. Components including the spring-loaded head, UAV mounting, and the battery carriage were 3D printed to keep the overall mass low. The battery carriage is placed at the back of the UAV, providing the flexibility to adjust battery position and thereby distribute mass to counterbalance the additional turning moment of the arm, aiding flight stability. Additionally, as shown in Figure 5.5, unnecessary material has been removed from the structural components, recognising the sensitivity of UAV flight performance to the payload's weight. These holes saved around 50% of the original mass, bringing the total UAV payload mass to 791 g, detailed in Table 5.1.

Table 5.1: UAV payload mass for the ultrasonic inspections

	Mass (g)
Onboard Computer	369
Laser Scanner	160
3D Printed Structures	126
Ultrasonic Transceiver	76
Ultrasonic Transducer with Signal Cables	60

The UAV actual payload mass was exceed 31.8% (191 g) of the datasheet nominal capacity, which sacrificed part of the aircraft's maneuverability. However, due to the UAV's six onboard rotors can generate 36 N of thrust in total, the aircraft still has the capability to undertake the inspections.

5.4.1 Experiment Setup

A 1 m^2 aluminium plate of 15 mm nominal thickness was fabricated and vertically mounted in the laboratory to mimic an industrial inspection scenario as presented in Figure 5.6. Rectangular and circular step blocks were machined into the rear surface of the plate to simulate the measurement of different thicknesses and corrosions with complex geometry. Additionally, fifteen flat-bottomed holes were also drilled in the plate with different depths and diameters, representing different sizes and depths of the sub-surface defect.

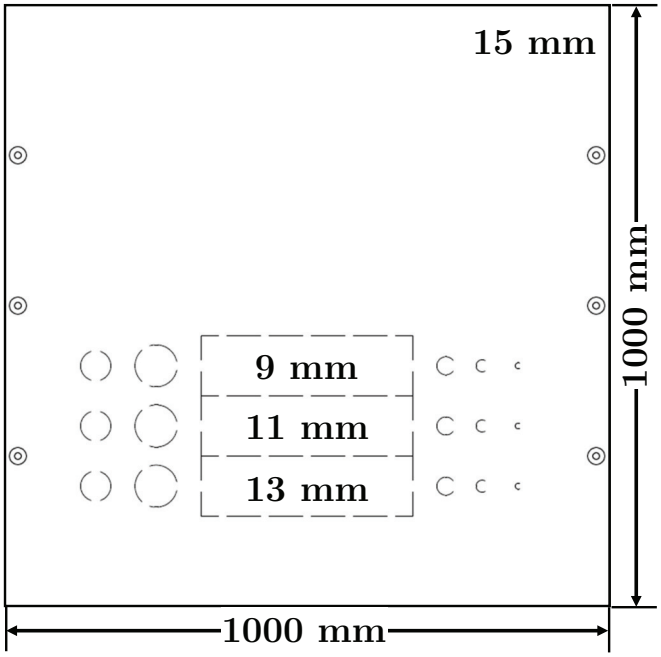

Figure 5.6: Aluminium sample schematic diagram

As shown in Figure 5.7 and Figure 5.8, when conducting the airborne inspections, the UAV initially rises to a certain height and stabilises itself at a distance from the asset. After achieving this pre-planned attitude, the controller guides the UAV closer to the asset until the ultrasonic probe at the front of the arm contacts the surface and measurements may be taken. Thereafter, the controller retracts the UAV waypoints to a standoff distance of 800 mm to prevent collision damage from forward movement induced by environmental disturbances. The UAV thereby

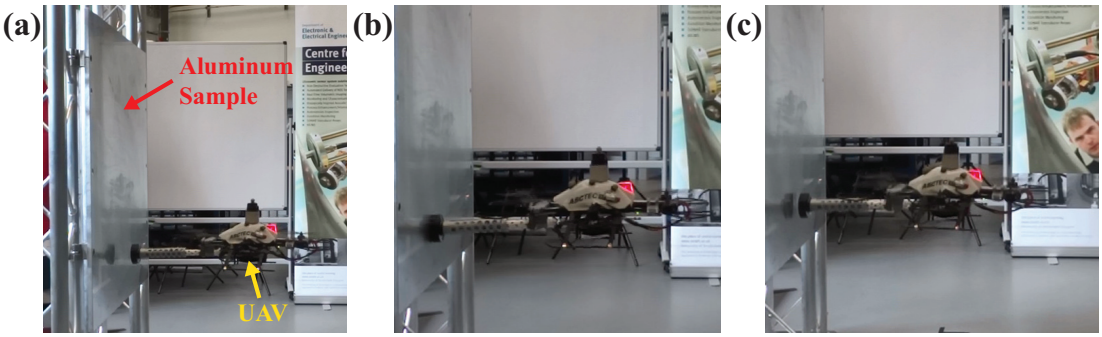

Figure 5.7: Still images taken from a video of the inspection process when UAV was: (a) close to the surface, (b) undertaking ultrasound inspection and (c) retracting to leave the surface

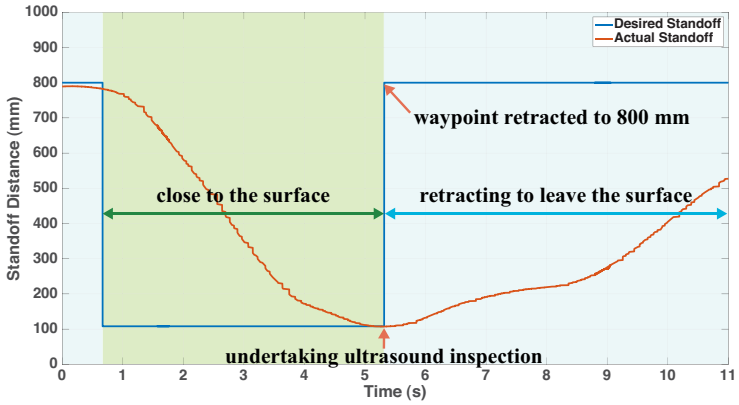

Figure 5.8: Desired UAV standoff and actual standoff recorded by the Vicon system when the UAV was undertaking the ultrasonic inspection,

leaves the inspection surface and makes ready for the next point measurement. After finishing the inspection process, the controller guides the craft to a designated safe area and performs an automatic landing.

5.5 Factors of Ultrasonic Measurement Accuracy

5.5.1 Signal-to-Noise Ratio

Herein, all thickness measurements are conducted by evaluating the time difference between two back-wall echoes observed in the A-scan results. An increased

noise level and weakened signal strength are noted to negatively influence the measurement's accuracy. In order to investigate such effects, the relative strength of the signal versus the accompanying noise is defined by the Signal-to-Noise Ratio (SNR), calculated by dividing the peak amplitude of the reflected signal by the noise amplitude and expressing the result in decibels:

$$SNR\ (dB) = \ 20log_{10}\frac{A_{signal}}{A_{noise}} \tag{5.9}$$

In this case, the noise is taken as the maximum amplitude of the signal within the regions where the reflected echo is not observed, ignoring the initial pulse transmission. To quantify the relationship between the SNR and inspection accuracy, over 2000 measurements were conducted using the ultrasonic circuity and transducer described in Section 5.4. The SNR was varied from 12 dB to 27 dB, in increments of 1 dB, by adjusting the amplifier gain. Measurements were repeated over 100 iterations at each SNR level, with the recorded errors versus the known sample dimensions then averaged over all trials and plotted in Figure 5.9.

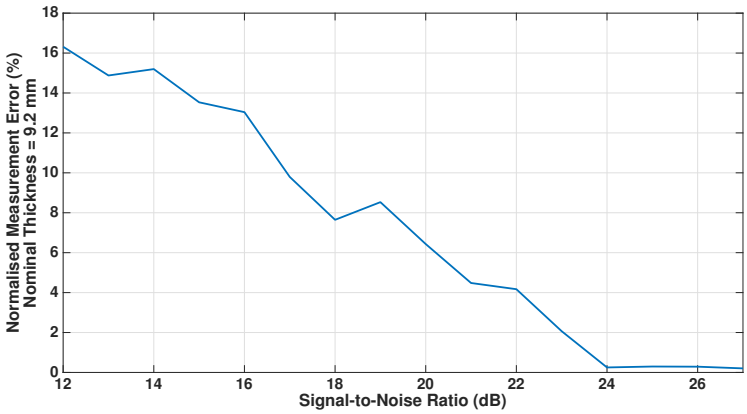

Figure 5.9: The relationship between the SNR and measurement error (averaging of 100 iterations)

It is clear that the measurement error was reduced with higher the SNR. While conducting the measurements of a 9.2 mm thickness sample, average errors were below 0.6 mm provided the SNR was larger than 20 dB. The further error

reductions were observed while he SNR was over 24 dB, where the error was below 0.03 mm.

5.5.2 Probe Alignment Angle

The transducer utilised in this chapter is a split-crystal ultrasonic probe. It may be readily realised from practical experience that probe alignment error causes signal attenuation when the transducer face is not parallel to the target surface. This experiment is thus designed to measure the alignment constraints of the transducer and quantify their impact on inspection accuracy in the larger context of the UAV deployment. Existing UAVs are focusing on photogrammetric inspections, which are not designed to precisely deploy an ultrasonic transducer. Hence, the ultrasonic transducer was mounted on the end of a KUKA KR6 R900 sixx: an industrial, six-degree of freedom, robotic manipulator arm [222]. Utilising the internal pose feedback, the robot pitch, roll and yaw angles and (x, y, z) translations, measured with 0.01° angular and 0.01 mm translational resolution respectively, were manually adjusted to move the ultrasonic probe through a range of poses. Compared with the transducer vibration when mounted on the UAV, the KUKA robot can deploy the transducer to much more precise positions granting the experiment repeatability and providing more accurate quantification results. Additionally, the measurements under this setup are not influenced by interference from the UAV motors, which is further described in Section 5.5.3.

In conducting the assessment, the transducer is triggered and its output signal digitised by the customised ultrasonic transceiver payload described in Section 5.4. The robot arm is manually controlled to adjust the transducer through a range of ± 6° in pitch and ± 9° in roll angle while maintaining contact with the inspection target via a layer of couplant gel. As demonstrated in Figure 5.10, an aluminium sample of 9.2 mm thickness is horizontally attached to the robot inspection platform and constitutes the inspection target for this scenario.

This sample is approached vertically by the robotic manipulator, using the same transducer and circuitry as on the UAV platform. So as to ensure that the maximum usable range of transducer orientations is determined, the amplifier gain of the ultrasonic acquisition board was set to its maximum value (47 dB) for the duration of these trials.

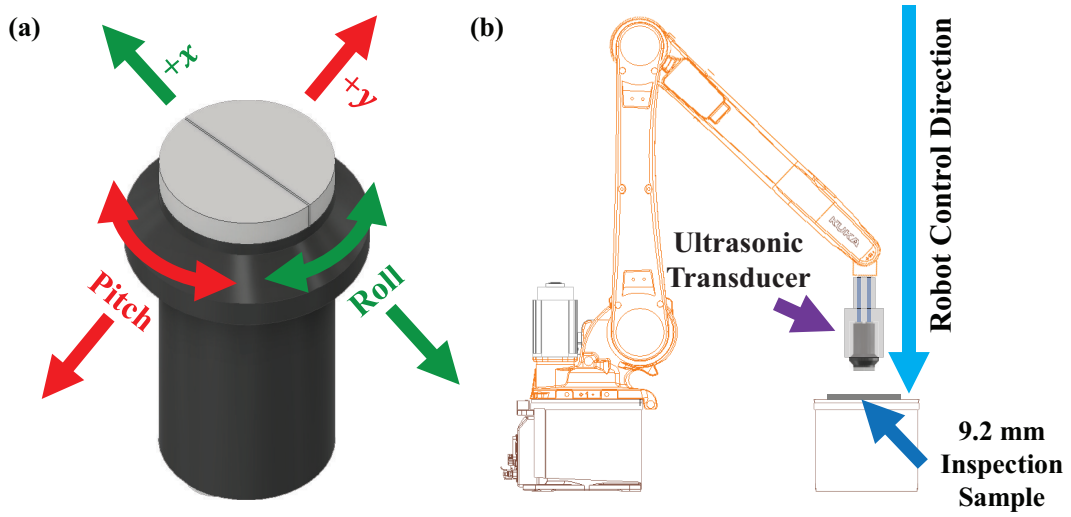

Figure 5.10: Experiment setup (a) transducer orientations (b) robotic manipulator setup for the quantification of alignment constraints

The A-scan signals of the transducer with different alignment errors are presented in Figure 5.11. These received signals have been digitally post-processed utilising a bandpass filter with a centre frequency of 5 MHz and bandwidth of 2 MHz. Table 5.2 and Table 5.3 list the measurement errors with different roll and pitch alignment errors, respectively, relative to the surface normal vector. Due to echoes cannot be recognised in the A-scan signals captured with -7°, -8°, 9° roll angle, ± 4°, ± 5° and ± 6° on pitch angle, the measurement errors at these angles were not calculated and listed in Table 5.2 and Table 5.3.

As shown in Figure 5.11, the reflection signals had the largest amplitude while the transducer was displaced to the position along the sample's surface normal vector (pitch and roll angles were 0°). In this case, a total of nine repetitions of the back-wall echo are identifiable in the A-scan signals. The increased signal

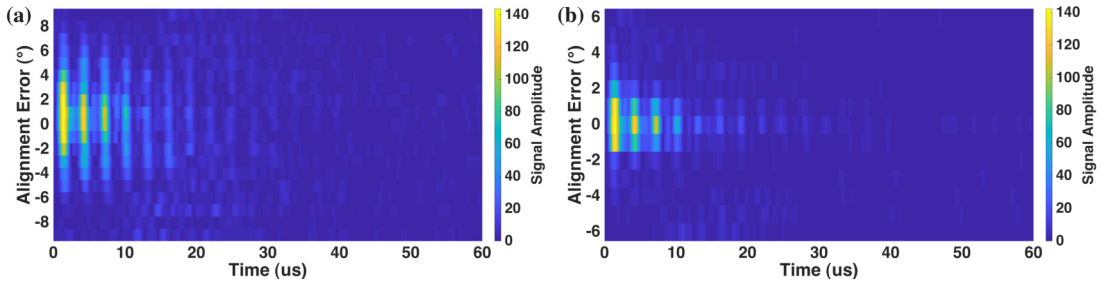

Figure 5.11: Single excitation A-scan signals with different transducer alignment errors (a) the transducer roll angle was adjusted between ± 9° (b) the transducer pitch angle was adjusted between ± 6°

attenuation at orientations diverging from normal and accompanying growth in measurement error highlights the relationship between the transducer alignment and inspection accuracy. As such, the back-wall reflection cannot be visually identified within the A-scan signal in the case where the transducer roll and pitch offset are larger than 6° and 3° respectively. Thus, the bounding constraints for alignment offset that may be tolerated while obtaining recognisable reflections are ± 6° on roll angle and ± 3° on pitch angle. It should, however, be noted that the reflection signals can be recognised in one direction of the movement about the roll axis up to 6° but 8° in the other. This phenomenon occurs owing to the alignment error's influence on the sound propagation path. Specifically, the transmitting and receiving piezoelectric elements are offset from the probe's longitudinal axis within the housing and so are tilted slightly towards this axis, to focus at a specific depth and achieve better signal transduction when properly aligned with the surface. This mounting choice means that the returning energy diverges more slowly from the receiver element when movement occurs in the direction of positive roll than in the negative, for a consistent angular increment.

5.5.3 Electrical Noise

The unwanted presence of electrical noise represents the last of the major factors considered to be influential in terms of inspection accuracy when using a UAV

Table 5.2: Mean errors and standard deviations of thickness measurements with different roll angle alignment errors using a single excitation (averaging of 20 iterations)

Alignment Error	-6°	-5°	-4°	-3°	-2°	-1°	0°	
Measurement Error ($\times 10^{-1}$ mm)	3.2±2.2	2.8±1.4	1.2±0.6	0.9±0.6	0.6±0.2	0.3±0.1	0±0.1	

Alignment Error	8°	7°	6°	5°	4°	3°	2°	1°
Measurement Error ($\times 10^{-1}$ mm)	3.2±1.8	2.8±1.5	2.8±1.4	2.4±1.2	2.4±0.7	1.5±0.7	0.6±0.4	0.3±0.1

Table 5.3: Mean errors and standard deviations of thickness measurements with different pitch angle alignment errors using a single excitation (averaging of 20 iterations)

Alignment Error	-3°	-2°	-1°	0°	1°	2°	3°
Measurement Error ($\times 10^{-1}$ mm)	8.2±2.4	7.3±1.2	0.6±0.3	0±0.1	0.3±0.2	3.8±3.2	7.3±4.3

based system. A potential source of interference within the inspection hardware is identified in the electric motors that provide the thrust during the multirotor UAV's flight. The raising of the noise floor as a result of the high-current electrical switching and magnetic field induction when the motors are activated may be expected to cause reduction of the signal-to-noise ratio, negatively influencing the accuracy of thickness measurement.

In this experiment, ultrasonic thickness measurements were undertaken from a stationary UAV that had been mounted rigidly in contact with the inspection surface and had its motors deactivated, so as to isolate the effects of electrical interference. To provide a comparison, the measurements were then repeated while the rotating UAV's six motors at speeds matching those required for flight. With the transducer having been optimally aligned manually and the amplifier gain set to maximise SNR, the rigid mounting structure acted to eliminate the effects of inconsistent alignment across the comparative trials. The raw signals recorded with deactivated stationary motors and with rotating motors are shown in Figure 5.12(a)(c), respectively. The digitally post-processed signals returned from the bandpass filter are similarly presented in Figure 5.12(b)(d).

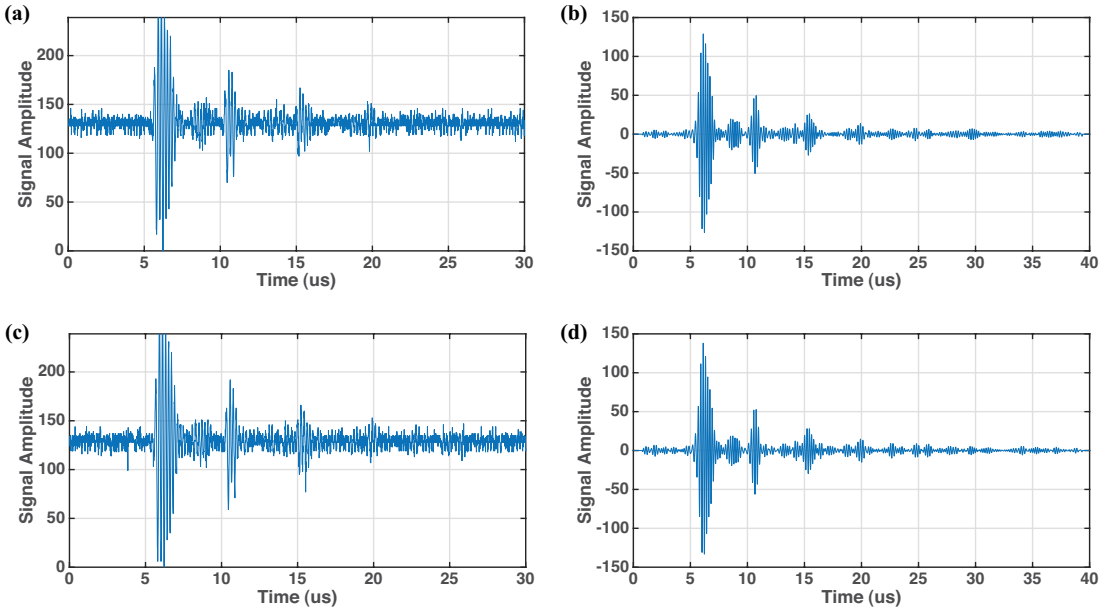

Figure 5.12: Thickness measurement signals (a) raw A-scan when the motors were stationary (b) processed A-scan when the motors were stationary (c) raw A-scan when the motors were rotating (d) processed A-scan when the motors were rotating

As presented in Figure 5.12, the rotating UAV motors slightly increased the power density of the noise: discrete flickers are observed in both raw signals, retaining a consistent amplitude but increasing in frequency upon activation of the motors. However, this effect does not remain observable in the bandpass filtered signals. Although the electrical interference increased the level of the noise, the SNR in the post-processed signal is reduced less by than 1 dB (from 25.13 dB to 24.22 dB) and did not influence the measurement accuracy. Hence, the presence of the electrical noise did not negatively impact the measurement accuracy.

5.5.4 UAV Positional Accuracy

As described in Section 5.5.2, the ultrasonic transducer requires the alignment error to be maintained below 3° on the roll and 6° on the pitch angle. This translates to a tolerance of ± 3° and ± 6° on the pitch and yaw angles expressed in the UAV's orientation frame. Due to the nature of multirotor kinematics and

aerodynamic effects arising from near-surface flight, these boundaries for alignment error of the probe represent a significant challenge from a UAV control perspective. Additionally, the mass of the ultrasonic measurement payload is close to the upper limits of feasibility, which affects the craft's controllability and stability and further influences the transducer alignment and positional accuracy. Unlike the alignment error, the positional error will not attenuate the signal amplitude as long as surface contact can be maintained. Such positional error may represent an obstacle in terms of repeatability, but a meaningful inspection may be conducted so long as the precise deployment position can be accurately recorded.

In attempting to quantify the flight stability performance of the current hardware, the UAV's full pose was tracked by the Vicon motion capture hardware and the positional accuracy relative to the desired point of inspection determined across flights with and without the ultrasound inspection payload. The results demonstrate the impact of the payload mass on the UAV's positional accuracy. Additionally, to evaluate the influence of near-surface aerodynamic effects, the position and alignment accuracy was quantified while the UAV was flying at distances of 200 mm and 800 mm from the aluminium plate. These two distances represent examples of a relatively small standoff, where the aerodynamic effects are prevalent, and the far distance, where the craft experiences free flight. These results therefore present the impact of the near-surface aerodynamic challenges and that of payload mass. Table 5.4 through Table 5.7 contain the standard deviations of the UAV pitch angle, yaw angle, y-axis position and z-axis position respectively. The positional error in x-axis is omitted because the UAV actions in this axis were used to approach the surface and so the error is of no consequence during contact inspection.

The results illustrate that the ultrasonic payload mass increased the standard deviation of the UAV yaw angle by 50% (from 1.82° to 2.61°), while the pitch angles were similar on both configurations. The increased moment of inertia about the UAV's vertical axis introduced by the mass of the transducer and extended

Table 5.4: Standard deviation of the UAV pitch angle

	Without Ultrasonic Payload	**With Ultrasonic Payload**
Free flight	0.49°	0.48°
Near-surface	0.50°	0.37°

Table 5.5: Standard deviation of the UAV yaw angle

	Without Ultrasonic Payload	**With Ultrasonic Payload**
Free flight	1.19°	2.61°
Near-surface	1.82°	2.71°

Table 5.6: Standard deviation of the UAV y-axis position

	Without Ultrasonic Payload	**With Ultrasonic Payload**
Free flight	24.01 mm	36.54 mm
Near-surface	54.47 mm	63.26 mm

Table 5.7: Standard deviation of the UAV z-axis position

	Without Ultrasonic Payload	**With Ultrasonic Payload**
Free flight	12.37 mm	16.83 mm
Near-surface	17.91 mm	17.48 mm

arm, coupled with the limited yaw authority when using differential motor reaction torque to turn the UAV, lead to a situation where negative effects were observed more readily in the yaw stability. The positional stability was also diminished with the standard deviation on the y-axis growing from 54.47 mm to 63.26 mm. Similar z-axis stability was observed in the inspections with and without payload. Of all the directions considered in terms of the decrease in UAV stability during the close-range inspections, the y-axis was most affected. The presence of the inspection payload increased the UAV total mass to a value approaching the upper limits of the UAV's capability, leading to challenges when utilising a PID controller to stabilise the aircraft in the horizontal plane. This effect is not present to the same extend in the z-axis as the craft may use all six motors to concretively correct for disturbances in this direction, reducing the sensitivity to increased payload.

In spite of the increase in alignment and positional error observed when carrying the additional ultrasonic payload and moving into close proximity with the inspection surface, it is possible to maintain the UAV alignment errors in pitch and yaw angle within the transducer's identified limitations such that contact-based inspection readings could be taken.

5.6 Inspection Results

The UAV successfully delivered the ultrasonic probe to the sample surface. Figure 5.13(a) shows one such ultrasonic A-scan signal captured during the thickness measurement deployed by the UAV using 180 V unipolar excitations to stimulate the transducer. At the time of signal acquisition, the pitch and yaw angle errors were 1.21° and 0.07°, while the errors on the y-axis and z-axis relative to the desired inspection position were 25.41 mm and 41.90 mm respectively. In this instance, the SNR of the filtered signal is 30.05 dB and the error in the thickness measurement is

0.03 ± 0.01 mm (on average of 11 iterations) versus the independently ascertained thickness of 12.92 mm as measured when the UAV was manually positioned and oriented in the optimal pose with its motors disabled. It is worth to note that ten iterations were measured from the stationary UAV with the same pose.

By contrast, Figure 5.13(c) shows an A-scan signal captured with poorer alignment, having angular errors of 1.61° and 2.01° in the pitch and yaw axes of the UAV frame and translational errors of 46.73 mm and 20.11 mm in the y-axis and z-axis, respectively. The presence of the alignment error attenuated the signal amplitude by 22 dB and increased the error to 0.26 ± 0.11 mm (on average of 11 iterations).

The UAV-deployed measurement results can be correlated to the alignment quantification results, as described in Section 5.5.2, which indicated the consistency between the KUKA-deployed measurements and the UAV-deployed measurements.

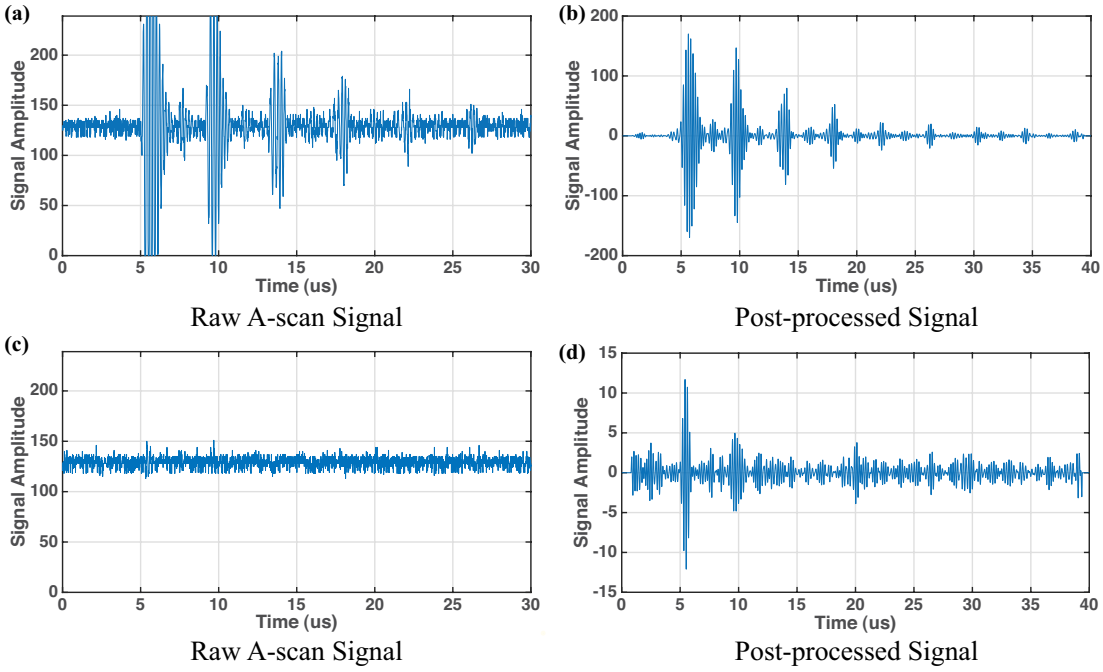

Figure 5.13: Thickness measurement acquired from the autonomous UAV deployed inspection (a)(b) with relative good alignment (c)(d) with relative large alignment error

Thickness mapping can be retrieved from a collection of the thickness measurements in various known positions. Despite the limited ability of the current system to

deploy the sensor precisely, recording the craft positional data while conducting the measurements were using the Vicon tracking system allows results of repeated flights to build up an image of component thickness across its surface area. Figure 5.14 presents an inspection result as an example of this, intended to simulate inspection in an industrial scenario. The inspection is composed of six measurements acquired by the autonomous controlled UAV system in different locations on the sample.

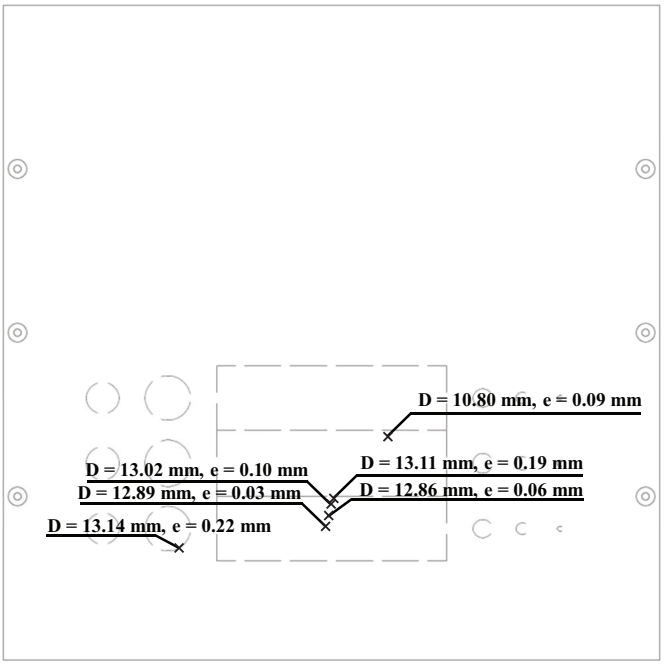

Figure 5.14: Inspection result of the UAV measurements conducted in six different positions

5.7 Coded Ultrasound Excitation

The experiment results presented in Section 5.5 show the alignment constraints of the conventional ultrasound transducer. Although the alignment error can be lessened by tuning the craft's flight controller, the current UAV mechanisms cannot ideally align the transducer parallel to the object surface. The signal reflections are attenuated and hidden inside the noise band, reducing the SNR and impact

the measurement accuracies. Therefore, a coded excitation sequence is utilised to trigger the transducer with a sequence of varying signal polarities and improve the SNR without the increment of the transducer excitation voltage. The sequence is coded as ± 1 on each bit, whereby the priority of the excitation voltage is varied in the sequence. The utilisation of coded sequence is a well-established method that has been shown to be effective for the improvement of SNR in ultrasonic systems. In particular, Golay code and Barker code are two approaches, seeing on the medical ultrasound applications [207], [223], EMATs [224], laser-generated ultrasound measurements [208] and air-coupled NDT measurements [209].

5.7.1 Golay Code

The Golay code is a sequence composed of a pair of complementary excitations, $g_1(t)$ and $g_2(t)$, each with a length of $L = 2n$ bits, where n is a positive integer [225]. These two coded excitations are transmitted in series before autocorrelation is utilised to decode the returning waveforms. The autocorrelation functions of the two excitations are denoted by $c_1(t)$ and $c_2(t)$, while the sum of these two functions, $c(t)$, is zero except at the point of zero lag, where the autocorrelation amplitude is maximised. The complementary sidelobes near the echoes appearing in $c_1(t)$ and $c_2(t)$ are suppressed in the final result, $c(t)$. As described by the Golay code definitions [226], the amplitude of $c(t)$ at zero lag and the corresponding frequency spectrum, $G(\omega)$, have the constant value of 2L.

Figure 5.15 is the autocorrelations of each coded excitation and the sum of the autocorrelation of an 8-bit complementary Golay pair (i.e. +1, +1, +1, -1, +1, +1, -1, +1 and +1, +1, +1, -1, -1, -1, +1, -1).

The sum of the Golay pairs at the frequency domain is given by:

$$G(\omega) = fft(c(t)) = fft(c_1(t)) + fft(c_2(t)) = 2L \tag{5.10}$$

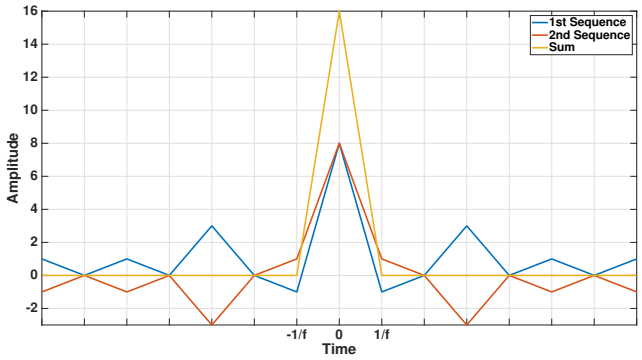

Figure 5.15: The autocorrelation function of an 8-bit Golay code pair and the sum of two autocorrelation function ($f = 5$ MHz)

where $fft()$ represents the fast Fourier transform. The Fourier transform of the autocorrelation functions $c_1(t)$ and $c_2(t)$ are defined by:

$$\begin{aligned} fft\left(c_1\left(t\right)\right) =& G_1\left(\omega\right) G_1^*\left(\omega\right) = \left|G_1\left(\omega\right)\right|^2 \\ fft\left(c_2\left(t\right)\right) =& G_2\left(\omega\right) G_2^*\left(\omega\right) = \left|G_2\left(\omega\right)\right|^2 \end{aligned} \tag{5.11}$$

where $G_1(\omega)$ and $G_2(\omega)$ are the frequency spectrum of the Golay pairs. $G_1^*(\omega)$ and $G_2^*(\omega)$ are the imaginary parts of the Fourier transform [208]. Hence, the sum of the Golay pairs in the frequency domain becomes:

$$G\left(\omega\right) = \left|G_1\left(\omega\right)\right|^2 + \left|G_2\left(\omega\right)\right|^2 = c\left(\omega\right) = 2L \tag{5.12}$$

Therefore, the amplitude of its frequency spectrum is:

$$\left|G\left(\omega\right)\right| = \sqrt{\left|G_1\left(\omega\right)\right|^2 + \left|G_2\left(\omega\right)\right|^2} = \sqrt{2L} \tag{5.13}$$

Considering the ultrasonic signal, $u(\omega)$, system transfer function, $H(\omega)$, and environmental noise, $n(\omega)$, expressed in the frequency domain; the outputs of each coded excitation, identified by their numerical subscripts, are given by:

$$\begin{aligned} Y_1\left(\omega\right) =& u\left(\omega\right) H_1\left(\omega\right) \left|G_1\left(\omega\right)\right|^2 + n_1\left(\omega\right) \left|G_1\left(\omega\right)\right| \\ Y_2\left(\omega\right) =& u\left(\omega\right) H_2\left(\omega\right) \left|G_2\left(\omega\right)\right|^2 + n_2\left(\omega\right) \left|G_2\left(\omega\right)\right| \end{aligned} \tag{5.14}$$

If the system responses in the first and second excitation are the same (i.e. $H_1(\omega) = H_2(\omega)$), the sum of the output signals becomes [226]:

$$Y_1(\omega)+Y_2(\omega) = u(\omega)\,H(\omega)\left(|G_1(\omega)|^2 + |G_2(\omega)|^2\right)+n_1(\omega)\,G_1(\omega)+n_2(\omega)\,G_2(\omega) \tag{5.15}$$

The noise added to the results is assumed as a zero-mean stochastically independent Gaussian white noise, while $|n_1(\omega)| = |n_2(\omega)| \approx 1$[210, 224]. Hence, the output signal is given by:

$$Y_1(\omega) + Y_2(\omega) \approx u(\omega)\,H(\omega)\,2L + \sqrt{2L} \tag{5.16}$$

Thus, the signal-to-noise ratio of the Golay code is increased by a factor of $\sqrt{2L}$ in noisy condition and improved by a factor of $2L$ in noiseless environments.

However, two sequence reflections might be executed and acquired with differing transducer alignments and positions during the UAV-deployed ultrasonic measurements due to the near-surface aerodynamic challenges and flight controller limitations. This will result in discrepancies between two transfer functions and introduce errors to the summation of the complementary signals. Therefore, the Golay code is of limited practicality with the current UAV platform.

5.7.2 Barker Code

A Barker code is a coding approach only require one coded excitation, $g(t)$, comprised of $L \in \{2, 3, 4, 5, 7, 11, 13\}$ bits with values of $\pm$ 1 [227]. Similar to the Golay code, autocorrelation is used to recover the Barker coded waveform. Its autocorrelation function is denoted $c(t)$ and presents with amplitude L at zero lag, while the rest of the amplitude coefficients are defined as $c \in \{-1, 0\}$. Figure 5.16 shows the autocorrelation of a Barker code sequence with the length of 13.

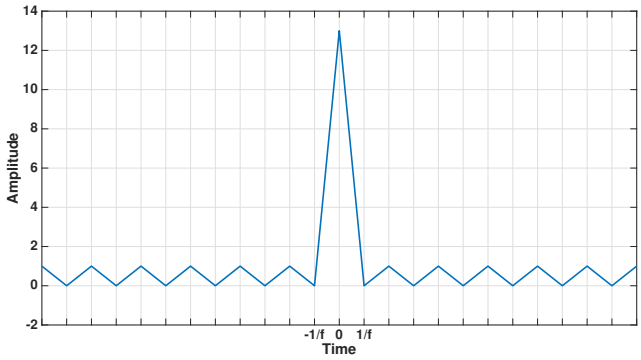

Figure 5.16: The autocorrelation function of a 13-bit Barker code sequence (f = 5 MHz)

However, unlike the Golay coded sequence, the Barker schema requires only one excitation sequence. This mitigates issues associated with systemic changes during acquisition but, in doing so, the sidelobes in the autocorrelation function cannot be cancelled. Therefore, the SNR increase generated is impacted by this coded excitation approach, in turn offering a lesser enhancement of the transducer's resolution. In spite of this, using only one excitation provides the Barker code with sufficient robustness function in the presence of minor systemic changes during and so allows its benefits to be applied to the current UAV-deployed ultrasonic technologies. In selecting which of the Barker codes would be most effective here, it is noted that the impact of sidelobes is defined by Peak-to-SideLobe level (PSL), calculated by the ratio of the amplitude at zero lag to the largest amplitude of the sidelobes [227]. Since the 13-bit Baker sequence (i.e. +1, +1, +1, +1, +1, -1, -1, +1, +1, -1, +1, -1, +1) contains the smallest PSL, the transducer was excited using this coded sequence.

The use of this specific sequence is well established in ultrasound. Zhang et al. presented a simulation which explored the 13-bit Barker code excitation of ultrasonic guided waves to assess fractures in long bones [207]. Zhou et al. also presented a hybrid approach utilising the 13-bit Barker code sequence and wavelet filtering to improve the received signal SNR and signal strength from an air-coupled ultrasonic transducer [209].

5.7.3 SNR Improvement and Sidelobes

To quantify the improvements offered by the Barker code sequence and the effects of the sidelobes in the context of UAV application, the transducer was fired using the 13-bit coded excitation with ideal alignment, positioned by the robotic manipulator, and in the absence of the electrical noise, as described previously in Section 5.5.2. For comparison, a single, un-coded excitation was also applied to the transducer using the same hardware. Both returning A-scan signals were digitised by the ultrasonic transceiver circuity and are shown in Figure 5.17. The system amplifier gain was set to 32 dB to prevent the signal saturation, however, the amplitude of the A-scan signal from coded excitation was reduced to match the amplitude of the first echo in the standard excitation signal.

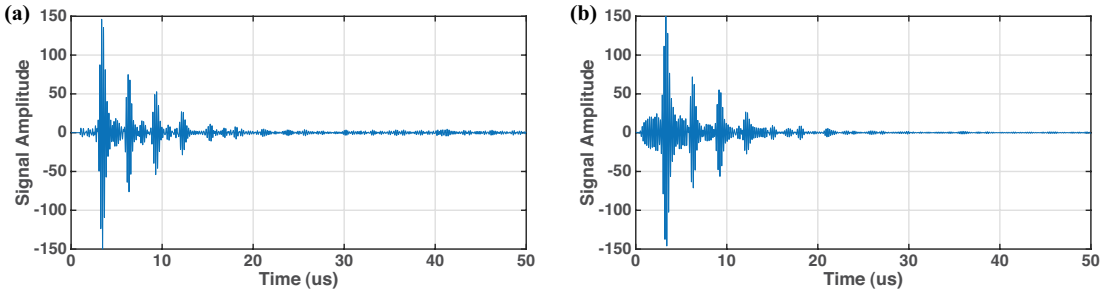

Figure 5.17: A-scan signals with different firing sequence (a) single excitation (b) 13-bit Barker coded excitation

As shown in Figure 5.17, the amplitude of the noise (after 30 ms) was substantially reduced by utilising the coded excitation. The SNR was increased by 10.93 dB, from 27.98 dB in the single excitation to 38.91 dB in 13-bit Barker coded excitation. This improvement was also observed while the UAV motors were rotating and generating the higher density electrical noise.

However, some harmonic noise can be observed in the signal regions close to the back-wall echoes in the A-scan signal with coded excitation. These harmonics are known as the sidelobes. As described in Section 5.7.2, these are intrinsic to the Barker coded excitation and may not be trivially extracted.

5.7.3.1 Signal Saturation

The gain of the amplifier in the ultrasonic transceiver circuit should be maximised to ensure the signals captured with large alignment errors are visible to the transceiver ADC. However, if care is not taken, the high amplitude signals returned by a system with small alignment errors may be overamplified to the point of saturation, resulting in significant distortion of the echo signals. These distortions create additional noise, the high frequency harmonics, which further impacts the waveform decoding.

This effect is demonstrated by the following simple experiment highlighting the impact of signal saturation in the presence of coded excitation. Here, the transducer was excited with the single, non-coded stimulus and then the 13-bit Barker sequence. The returned A-scan signals were amplified by 32 dB to ensure no saturation appears on the signal and the maximum gain, 47 dB, for both excitations, with the resultant amplified and processed signals being shown in Figure 5.18.

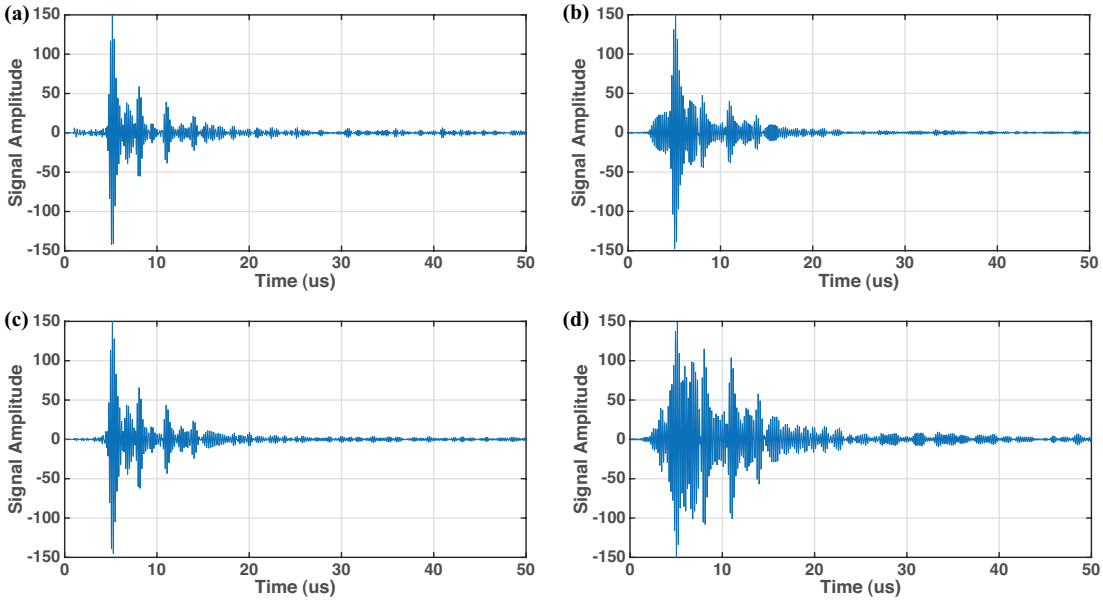

Figure 5.18: A-scan signals with different amplifier gain and firing sequence (a) single excitation amplified by 32 dB (b) coded excitation amplified by 32 dB (c) single excitation amplified by 47 dB (d) coded excitation amplified by 47 dB

Compared with the single excitation, the coded sequence amplified by the smaller gain demonstrated a reduced noise level but sidelobes were observed near the back-wall echoes. With the increase in the amplifier gain, the standard excitation presented a smaller noise amplitude and the echoes were still recognisable. However, as shown in Figure 5.18(d), the coded signal was overamplified at this maximum gain, leading to the distortions and the increased noise level when compared to the standard excitation. Additionally, the second echo is hard to identify in the A-scan signal, owing to its masking by the presence of sidelobes and other phenomena appearing between the backwall echoes. Despite this, it is notable that thickness can be calculated by using the time difference between the first and third echoes, so indicating that, while the scenario is far from ideal and should be avoided, the results may still be somewhat useful.

5.7.4 Measurement Accuracy Improvement

To investigate any improvements in thickness measurement accuracy, the experiments described in Section 5.5.2 were repeated with the improved SNR of coded excitation. Again, the robotic manipulator arm precisely positioned the transducer with different alignment errors before the amplifier gain was adjusted to prevent signal saturation. Corresponding results are listed in Table 5.8 and Table 5.9.

Table 5.8: Mean errors and standard deviations of thickness measurement with different roll angle alignment errors using coded excitation (averaging of 20 iterations)

Alignment Error	-6°	-5°	-4°	-3°	-2°	-1°	0°	
Measurement Error ($\times 10^{-1}$ mm)	2.3±1.8	0.9±1.3	0.9±0.8	0.6±0.2	0.2±0.1	0.1±0.1	0±0.1	

Alignment Error	8°	7°	6°	5°	4°	3°	2°	1°
Measurement Error ($\times 10^{-1}$ mm)	2.7±1.4	0.6±0.4	0.6±0.3	0.5±0.3	0.3±0.2	0.2±0.1	0.1±0.1	0.1±0.1

As shown in Table 5.8, the majority of the inspection errors when conducting the measurements with alignment errors were, under this scheme, below 0.1 mm.

Table 5.9: Mean errors and standard deviations of thickness measurement with different pitch angle alignment errors using coded excitation (averaging of 20 iterations)

Alignment Error	-3°	-2°	-1°	0°	1°	2°	3°
Measurement Error ($\times 10^{-1}$ mm)	6.6±3.7	4.3±0.2	0.3±0.1	0±0.1	0.2±0.1	0.9±0.4	4.1±3.4

Compared with the results listed in Table 5.2 and Table 5.3, the measurement errors were markedly decreased using the coded excitation.

5.8 Discussions

This chapter reviewed the principles of ultrasound and evaluated several ultrasonic transducers. It presented an autonomous, UAV-deployed, contact-based, ultrasonic measurement system for the inspection of vertical structures and detailed how measurements were conducted by utilising a commercial split-crystal probe with customised transceiver circuity. The UAV was able to successfully navigate an indoor laboratory environment under direction of the flight controller, utilising additional information from a planar laser scanner and acting without manual intervention. As such, the system conducted measurements in a region of the aluminium sample with 12.92 mm nominal thickness, reporting the thickness with 0.03 mm error owing to non-ideal conditions intrinsic to the nature of the system. At one point of inspection the pitch and yaw errors were 1.21° and 0.07°, while the errors on the y-axis and z-axis were 25.41 mm and 41.90 mm respectively relative to the desired inspection position.

Two parameters, probe alignment angle and electrical interference from the UAV motors are considered as potential constraints on inspection performance, influencing the ultrasonic measurement accuracy in terms of a reduction in SNR. Their isolated impacts on the overall accuracy were quantified and analysed. Despite the increased power density of system noise conferred by the electrical interference

of the active brushless motors, the noise contribution from this source is much less than that arising from the probe alignment error. Experimental analyses show that the probe's roll and pitch angle are required to be within 6° and 3°, respectively, of the surface normal vector to receive any identifiable back-wall echoes in the A-scan signal.

In its role governing the transducer orientation, the UAV's positional accuracy, including the surface alignment accuracy, is crucial to producing a meaningful inspection and as such the accuracies of the current inspection system were evaluated and discussed. Due to the aerodynamic challenges and the payload mass restrictions, the performance levels presented are taken as the intrinsic limitations of the current system.

Therefore, coded ultrasound excitation was proposed to improve the ultrasonic measurement accuracy, and its implementation evaluated. Under the 13-bit Barker sequence excitation, a 10.93 dB SNR improvement was observed. Additionally, the coded sequence also reduced the measurement errors in scenarios where the transducer was sub-optimally aligned.

Future work will consider methodologies to improve UAV stability and reduce its positional and alignment error in a manner that would grant enhanced inspection accuracy. The six motors of the UAV system are currently positioned within a single horizontal plane and with the same orientation and so struggle to produce an appropriate force to maintain contact with the surface in a manner decoupled from the manoeuvring of the aircraft. While the UAV is conducting the measurements, such mechanism also causes the transducer alignment error, whereby a pull-off force is produced between the probe and the target surface. Hence, alternative UAV mechanical designs will be investigated to lessen the probe alignment issues and further improve the inspection accuracy beyond current efforts. Moreover, a novel ultrasonic transducer topology with a wider angular coupling capability, is

identified as a strategy to offer greater redundancy against alignment error caused by the non-ideal UAVs positioning.

Finally, it is worth noting that, as a conventional transducer, the ultrasonic probe utilised in this system requires a small quantity of couplant gel to be applied between the transducer and inspection surface, which is of limited practicality in real inspection scenarios. Thus, a dry-coupled ultrasonic transducer (e.g. wheel probe), making use of a rubber wheel instead of liquid couplant, will be considered as part of future work.

Chapter 6

Conclusions and Future Work

6.1 Conclusions

This thesis presented an autonomous aerial platform for Non-destructive Testing inspections. The platform was composed of a modified AscTec Firefly UAV for indoor experiments, a miniature planar laser scanner, and an inspection payload for different NDT tasks. The UAV was autonomously stabilised and guided to follow the desired trajectory by an off-board workstation in the laboratory. The UAV onboard computer acquired sensor data and wirelessly communicated with the offboard workstation through Wi-Fi. The GUI on the off-board workstation monitored the instantaneous sensor readings and the UAV flight status.

A PID-based controller was implemented in this aerial platform for autonomous UAV navigation. The mean trajectory errors and the standard deviations were measured as below 30 mm and 15 mm, respectively, which quantifiably demonstrated the stability of the UAV control system. The laser scanner mounted atop the UAV mapped the surroundings, providing the standoff and alignment offset measurements versus the surface normal vector of the target object. The curve fitting procedure improved laser scanner accuracy, providing more precise align-

ment offset measurements. The standard deviation of the distance measurement was reduced from 2.70 mm to 1.20 mm, accompanied by a significant reduction in the standard deviation of the alignment measurement, from 4.68° to 0.32°. The off-board workstation utilised the standoff distance and alignment error from the laser scanner to produce adaptive flight trajectories during inspections. Such flight trajectories maintained the UAV's standoff to the target with an appropriate orientation angle, improving inspection accuracy. The implementations and evaluations of the flight controller and the laser scanner were documented in Chapter 3.

In this thesis, two UAV-deployed NDT inspection approaches, namely photogrammetric surface evaluation and contact-based ultrasonic thickness mapping, were presented. The photogrammetric inspection provided an overview of the general surface integrity and discontinuities on the surface coating, offering a rapid inspection albeit with no detailed structural information. Contact-based ultrasonic inspections conducted thickness measurements at multiple discrete points to evaluate the internal structural condition of the target.

The airborne photogrammetric inspections were presented in Chapter 4. Photogrammetric technologies for 3D profile reconstructions and inspections were first reviewed. Implementation of the photogrammetric inspections on a wind turbine blade were detailed. The mean error of the reconstructed model under optimised conditions was below 0.25 mm, the peak-to-peak error was less than 4.3 mm, and the standard deviation was below 0.92 mm when compared with a ground-truth, metrology-grade reconstruction. Three parameters (motion blur, focal blur, and environmental brightness conditions) had direct impacts on the image quality and ultimate inspection accuracy, and were quantified in this chapter. The results of a laser-based trajectory showed the mitigation effect with an active correction mechanism and appropriate environment setup. This integration of the laser scanner improved the photogrammetric inspection accuracy and filled the gap of close-range inspections of targets with complex geometry. The laser scanner

data was integrated into image processing to remove background features. The experimental results illustrated that the background features were involved in the Agisoft image alignment process. This demonstrated the limitation of the current reconstruction pipeline and also presented an example for integrating the laser data into inspections. Finally, an extraction algorithm was demonstrated, which highlighted the discontinuities and scuffs on the resulting 3D profile. These works deepened the understanding of the challenges during photogrammetric inspections (especially those performed indoors) and provided approaches to mitigate the negative influences of these challenges and improve the inspection accuracy.

Chapter 5 focused on the implementation and evaluation of a contact-based ultrasonic inspection system. The inspection payload was composed of a conventional, split-crystal, 5 MHz probe and ultrasonic transceiver circuitry. The UAV successfully conducted the contact-based ultrasonic measurements. While inspecting a sample of 13 mm thickness, the UAV system demonstrated a measurement error of 0.03 mm. During this process, the standard deviation of the craft's positional error was recorded as below 63.26 mm, accompanied by an angular alignment error relative to the surface normal vector of below 2.71°. The errors corresponded to the UAV's positional and alignment accuracy, transducer alignment constraints, and electrical noise. The impact of these factors on the measurement accuracy were characterised, but could not be mitigated. Therefore, coded excitations were investigated to improve the received signal SNR and measurement accuracy for use within current inspection hardware. These findings provide the benchmarks on existing inspection methods and form the basis for future work. The connections between the ultrasonic alignment angles and the ultrasonic measurement errors will serve as the basis for the further airborne ultrasonic system development.

6.2 Future Work

A number of key areas for future work in UAV-deployed inspections were presented throughout the thesis. These research areas will further improve inspection accuracy and the efficiency of airborne NDT inspections.

The inspections demonstrated in this thesis were undertaken in a laboratory-based environment, which is an idealised situation with controlled flight conditions. The Vicon MX system offers sub-millimetre accuracy on UAV positional tracking and navigation. Real outdoor inspections require the UAV to fly in windy conditions and to operate with less accurate positional tracking. Therefore, investigations into a different flight controller approaches and DGPS should be considered for outdoor inspections.

The integration of a 2D planar laser scanner measured the UAV standoff distance and alignment offset against the target object. The current laser scanner with curve fitting procedure can only map the surroundings and identify the target in a 2D plane. This introduced standoff errors, observed while inspecting the edge of the wind turbine blade. Future work in this area should consider a detailed 3D mapping during flight, using a 3D scanner or a 3D camera, which contains a larger field of view. Moreover, the laser scanner outputs can be integrated into the reconstruction progress to improve the accuracy of the current photogrammetric reconstructions. This laser curve fitting and waypoints generation strategy presented in Chapter 3, which used a flat surface. The laser scanner successfully produced the adaptive flight path during the inspections, but positions at the turbine blade edges had slightly larger standoff errors. The curve fitting model was not suitable for curve estimation of the turbine blade edges and complex geometries. Future work will consider methodologies to improve the curve fitting procedure.

Since the laser scanner allows the waypoints generation on the flight, the object movements during the inspection are less likely causing the UAV collisions. How-

ever, during the 3D photogrammetric inspections, the asset needs to be stationary because of the nature of Structure from Motion. Therefore, based on current techniques, the target objects, such as wind turbine blades, require a temporary shut down during the in-service inspections. Hence, future work will consider integration of other sensors (e.g. a structured light camera), so that the inspections can be utilised on dynamic moving objects.

Particular attention was paid to the contributions of background features on the current reconstruction pipeline. The background features impacted the camera alignment. This remains problematic, as outdoor inspections do not offer such dense background features. These issues can be solved by tuning the parameters and optimising the algorithms to extract more features from the turbine blade. However, the source code of the reconstruction process in Agisoft Photoscan is restricted, and thus, optimisations to the current pipeline are not possible. Future work in this area will investigate a research-based system to reconstruct 3D profiles. The system will provide adjustable parameters and optimisations for different industrial applications. It will also allow for the integration of laser readings and image poses from position tracking systems into the reconstruction process, thereby improving inspection accuracy.

The autonomous discontinuity extraction algorithm presented at the end of Chapter 4 could not classify defects. Improvements to this algorithm with the integration of artificial intelligence and neural networks will provide autonomous discontinuity classification, making review of the 3D profile more effective for inspectors. The inspectors can quickly locate the defects and classify the degree of damage using such enhanced 3D utilities. A strategy for integration of the reconstruction model into a mixed reality headset is also being evaluated in the research group. This utility will provide an immersive experience, so that inspectors can better assess the level of damage and the object's health condition.

Due to hardware limitations, the current camera was triggered with a 2 Hz repetition frequency, whereas the nominal camera frequency could achieve 35 Hz. Thus, 33 more images could be captured in a second. A quality assessment could be conducted to filter blurry images before the 3D reconstruction procedure. Additionally, the image acquisition could be more efficient in return for fewer acquired images, triggering the camera at desired positions instead of through continuous triggering. The image sharpness will be real-time assessed to ensure enough features have been captured to satisfy the accuracy requirements. Moreover, due to the nature of UAV stability, the camera cannot be precisely positioned at the focusing distance. Therefore, a motorised lens would be useful to adjust the camera focus in accordance with the laser's instantaneous measurements. Such works guarantee that only the best images are captured in relevant areas to be utilised for reconstruction, thereby improving the inspection accuracy and efficiency.

A series of evaluations of coded excitation were presented at the end of Chapter 5. Further researches will analyse and evaluate various coding methods on the UAV platforms. Furthermore, as described in Chapter 5, the conventional ultrasonic transducer will be replaced by a dry-coupled wheel probe, which will be more practical in real inspections. A C-scan inspection could be conducted using a wheel probe combined with the coded excitation strategy. In addition, alternative UAV mechanical designs, such tiltrotor (described in Chapter 2), are under evaluation. These novel designs are intended to lessen probe alignment issues and further improve inspection accuracy beyond current efforts.

In a long term vision of ultrasonic inspection, future work should investigate alternative mechanical mounting designs to lessen probe alignment issues and further reduce the payload mass. Additional research should also focus on novel ultrasonic transducer topologies with a wider angular coupling capability. This is a strategy to provide greater redundancy against alignment error originating from the non-idealises in UAV positioning.

Bibliography

[1] R. G. Little, "Controlling Cascading Failure: Understanding the Vulnerabilities of Interconnected Infrastructures," *Journal of Urban Technology*, vol. 9, no. 1, pp. 109–123, 2002.

[2] I. Atomic and E. Agency, *Non-destructive Testing : A Guidebook for Industrial Management and Quality Control Personnel*. No. 9, 1999.

[3] Merriam-Webster, "Photogrammetry." [online] https://www.merriam-webster.com/dictionary/photogrammetry [Accessed: 30-Dec-2018].

[4] S. Jordan, J. Moore, S. Hovet, J. Box, J. Perry, K. Kirsche, D. Lewis, and Z. T. H. Tse, "State-of-the-art technologies for UAV inspections," *IET Radar, Sonar & Navigation*, vol. 12, pp. 151–164, Jan 2018.

[5] D. Ensminger and L. J. Bond, *Ultrasonics: fundamentals, technologies, and applications*. 2011.

[6] P. Thayer, "RCNDE industrial members' vision for the future requirements for NDE," *Insight: Non-Destructive Testing and Condition Monitoring*, vol. 54, no. 3, pp. 124–127, 2012.

[7] P. Thayer, "Enabling the fourth industrial revolution (4IR) and the role of NDE and monitoring," *Insight: Non-Destructive Testing and Condition Monitoring*, vol. 59, no. 9, pp. 469–472, 2017.

[8] M. Friedrich, G. Dobie, C. C. Chan, S. G. Pierce, W. Galbraith, S. Marshall, and G. Hayward, "Miniature Mobile Sensor Platforms for Condition Monitoring of Structures," *IEEE Sensors Journal*, vol. 9, no. 11, pp. 1439–1448, 2009.

[9] G. Dobie, R. Summan, S. G. Pierce, W. Galbraith, and G. Hayward, "A noncontact ultrasonic platform for structural inspection," *IEEE Sensors Journal*, vol. 11, no. 10, pp. 2458–2468, 2011.

[10] G. Dobie, R. Summan, C. MacLeod, and S. Gareth Pierce, "Visual odometry and image mosaicing for NDE," *NDT and E International*, vol. 57, pp. 17–25, 2013.

[11] Eddyfi, "I-Flex ECA Probes," 2018. [online] https://www.eddyfi.com/products/i-flex-eca-probes/ [Accessed: 30-Dec-2018].

[12] D. Roca, S. Lagüela, L. Díaz-Vilariño, J. Armesto, and P. Arias, "Low-cost aerial unit for outdoor inspection of building façades," *Automation in Construction*, vol. 36, pp. 128–135, 2013.

[13] V. N. Nguyen, R. Jenssen, and D. Roverso, "Automatic autonomous vision-based power line inspection: A review of current status and the potential role of deep learning," *International Journal of Electrical Power and Energy Systems*, vol. 99, pp. 107–120, 2018.

[14] R. A. Clark, G. Punzo, C. N. MacLeod, G. Dobie, R. Summan, G. Bolton, S. G. Pierce, and M. Macdonald, "Autonomous and scalable control for remote inspection with multiple aerial vehicles," *Robotics and Autonomous Systems*, vol. 87, pp. 258–268, 2017.

[15] D. Lattanzi and G. R. Miller, "3D Scene Reconstruction for Robotic Bridge Inspection," *Journal of Infrastructure Systems*, vol. 21, no. 2, p. 04014041, 2015.

[16] S. S. Mansouri, C. Kanellakis, E. Fresk, D. Kominiak, and G. Nikolakopoulos, "Cooperative coverage path planning for visual inspection," *Control Engineering Practice*, vol. 74, pp. 118–131, 2018.

[17] Gaia-Wind, "Gaia-Wind," 2018. [online] http://www.gaia-wind.com/ [Accessed: 10-Nov-2018].

[18] KNJN, "Xylo-EM FPGA board." [online] https://www.knjn.com/FPGA-FX2.html [Accessed: 30-December-2018].

[19] S. Bouabdallah, P. Murrieri, and R. Siegwart, "Design and control of an indoor micro quadrotor," in *IEEE International Conference on Robotics and Automation, 2004. Proceedings. ICRA '04. 2004*, pp. 4393–4398 Vol.5, 2004.

[20] GB Inspection Systems Ltd., "Compression Wave 0º Probes," 2018. [online] https://www.gbinspection.com/products/probes-accessories/compression-wave-0-probes [Accessed: 30-Dec-2018].

[21] FLIR, "Inspectahire relies on the FLIR GFx320 Optical Gas Imaging camera for maintenance inspections and hydrocarbon leak detection in the offshore oil and gas industry," 2017.

[22] Ascending Technologies, "AscTec Firefly Technical Data," 2015. [online] http://wiki.asctec.de/display/AR/AscTec+Firefly#AscTecFirefly-TechnicalData [Accessed: 07-Nov-2018].

[23] G. Punzo, C. MacLeod, K. Baumanis, R. Summan, G. Dobie, G. Pierce, and M. Macdonald, "Bipartite Guidance, Navigation and Control Architecture for Autonomous Aerial Inspections Under Safety Constraints," *Journal of Intelligent and Robotic Systems: Theory and Applications*, pp. 1–13, 2018.

[24] A. Parsch, "Curtiss/Sperry "Flying Bomb," 2018. [online] http://www.designation-systems.net/dusrm/app4/sperry-fb.html [Accessed: 30-Dec-2018].

[25] Microdrones, "UAVs For Search and Rescue – Because Every Second Counts," 2018. [online] https://www.microdrones.com/en/industry-experts/public-safety/search-and-rescue/ [Accessed: 30-Dec-2018].

[26] E. Lygouras, A. Gasteratos, K. Tarchanidis, and A. Mitropoulos, "ROLFER: A fully autonomous aerial rescue support system," *Microprocessors and Microsystems*, vol. 61, pp. 32–42, 2018.

[27] H. A. Kurdi, E. Aloboud, M. Alalwan, S. Alhassan, E. Alotaibi, G. Bautista, and J. P. How, "Autonomous task allocation for multi-UAV systems based on the locust elastic behavior," *Applied Soft Computing Journal*, vol. 71, pp. 110–126, 2018.

[28] K. Guevara, M. Rodriguez, N. Gallo, G. Velasco, K. Vasudeva, and I. Guvenc, "UAV-based GSM network for public safety communications," *Conference Proceedings - IEEE SOUTHEASTCON*, vol. 2015-June, no. June, 2015.

[29] 3DR, "Drone Surveying and Mapping." [online] https://3dr.com/industries/survey-mapping/ [Accessed: 30-Dec-2018].

[30] S. Grzonka, G. Grisetti, and W. Burgard, "A fully autonomous indoor quadrotor," *IEEE Transactions on Robotics*, vol. 28, no. 1, pp. 90–100, 2012.

[31] S. Espositoa, P. Fallavollitaa, W. Wahbehb, C. Nardinocchic, and M. Balsia, "Performance evaluation of UAV photogrammetric 3D reconstruction," *International Geoscience and Remote Sensing Symposium (IGARSS)*, pp. 4788–4791, 2014.

[32] M. P. Christiansen, M. S. Laursen, R. N. Jørgensen, S. Skovsen, and R. Gislum, "Designing and testing a UAV mapping system for agricultural field surveying," *Sensors (Switzerland)*, vol. 17, no. 12, 2017.

[33] H. Aasen, A. Burkart, A. Bolten, and G. Bareth, "Generating 3D hyperspectral information with lightweight UAV snapshot cameras for vegetation monitoring: From camera calibration to quality assurance," *ISPRS Journal of Photogrammetry and Remote Sensing*, vol. 108, pp. 245–259, 2015.

[34] Health Safety Executive, "Working at height - A brief guide," 2014. [online] http://www.hse.gov.uk/pubns/indg401.pdf [Accessed: 30-Dec-2018].

[35] T. Omar and M. L. Nehdi, "Remote sensing of concrete bridge decks using unmanned aerial vehicle infrared thermography," *Automation in Construction*, vol. 83, pp. 360–371, 2017.

[36] Cyberhawk, "UAV Inspection Surveying," 2018. [online] https://www.thecyberhawk.com/[Accessed: 30-Dec-2018].

[37] Vertex Air, "Drone Thermal Imaging," 2018. [online] http://vertexaccess.co.uk/vertexair/services/thermal-imaging/ [Accessed: 30-Dec-2018].

[38] X. Li, Q. Yang, Z. Chen, X. Luo, and W. Yan, "Visible defects detection based on UAV-based inspection in large-scale photovoltaic systems," *IET Renewable Power Generation*, vol. 11, no. 10, pp. 1234–1244, 2017.

[39] senseFly, "Engineering & Construction." [online] https://www.digi.com/resources/documentation/digidocs/PDFs/90000982.pdf [Accessed: 26-April-2019].

[40] N. Metni and T. Hamel, "A UAV for bridge inspection: Visual servoing control law with orientation limits," *Automation in Construction*, vol. 17, no. 1, pp. 3–10, 2007.

[41] M. Gerke and P. Seibold, "Visual inspection of power lines by U.A.S.," *EPE 2014 - Proceedings of the 2014 International Conference and Exposition on Electrical and Power Engineering*, pp. 1077–1082, 2014.

[42] T. H. Chung, M. R. Clement, M. A. Day, K. D. Jones, D. Davis, and M. Jones, "Live-fly, large-scale field experimentation for large numbers of fixed-wing UAVs," *Proceedings - IEEE International Conference on Robotics and Automation*, vol. 2016-June, pp. 1255–1262, 2016.

[43] A. Moutinho, J. R. Azinheira, E. C. de Paiva, and S. S. Bueno, "Airship robust path-tracking: A tutorial on airship modelling and gain-scheduling control design," *Control Engineering Practice*, vol. 50, pp. 22–36, 2016.

[44] Y. Yang, J. Wu, and W. Zheng, "Positioning Control for an Autonomous Airship," *Journal of Aircraft*, vol. 53, no. 6, pp. 1638–1646, 2016.

[45] R. Fedorenko and V. Krukhmalev, "Indoor Autonomous Airship Control and Navigation System," *MATEC Web of Conferences*, vol. 42, p. 01006, 2016.

[46] J. Müller and W. Burgard, "Efficient probabilistic localization for autonomous indoor airships using sonar, air flow, and IMU sensors," *Advanced Robotics*, vol. 27, no. 9, pp. 711–724, 2013.

[47] F. B. Abdallah, N. Azouz, L. Beji, and A. Abichou, "Modeling and stabilization of a cable-driven parallel platform suspended by an airship," *11th International Workshop on Robot Motion and Control, RoMoCo 2017 - Workshop Proceedings*, pp. 53–58, 2017.

[48] S. J. Newman, *Basic helicopter aerodynamics*, vol. 3. 2011.

[49] Sikorsky, "Sikorsky S-92 Helicopter," 2018. [online] http://www.sikorsky.com/Pages/Products/Commercial/S92/S92.aspx [Accessed: 30-Dec-2018].

[50] Boeing, "Boeing CH-47 CHINOOK," 2018. [online] http://www.boeing.com/defense/ch-47-chinook/ [Accessed: 30-Dec-2018].

[51] S. Bouabdallah, A. Noth, and R. Siegwart, "PID vs LQ control techniques applied to an indoor micro quadrotor," *2004 IEEE/RSJ International Conference on Intelligent Robots and Systems (IROS) (IEEE Cat. No.04CH37566)*, vol. 3, pp. 2451–2456, 2004.

[52] Federal Aviation Administration, "Aerodynamics of Flight," in *Pilot's handbook of Aeronautical Knowledge*, no. Cl, pp. 2–5, 2010.

[53] J. R. Page and P. E. I. Pounds, "The Quadroller: Modeling of a UAV/UGV hybrid quadrotor," *IEEE International Conference on Intelligent Robots and Systems*, pp. 4834–4841, 2014.

[54] D. Findlay, M. Jafarinasab, and S. Sirouspour, "Optimization-based design of a novel hybrid aerial/ground mobile manipulator," *IEEE International Conference on Intelligent Robots and Systems*, vol. 2015-Decem, pp. 2467–2472, 2015.

[55] A. Kalantari and M. Spenko, "Modeling and performance assessment of the HyTAQ, a hybrid terrestrial/aerial quadrotor," *IEEE Transactions on Robotics*, vol. 30, no. 5, pp. 1278–1285, 2014.

[56] Flyability, "Elios - Inspect & Explore Indoor and Confined Spaces," 2018. [online] https://www.flyability.com/elios/ [Accessed: 03-Jan-2019].

[57] M. Ryll, H. H. Bülthoff, and P. R. Giordano, "A novel overactuated quadrotor unmanned aerial vehicle: Modeling, control, and experimental validation," *IEEE Transactions on Control Systems Technology*, vol. 23, no. 2, pp. 540–556, 2015.

[58] Z. Liu, Y. He, L. Yang, and J. Han, "Control techniques of tilt rotor unmanned aerial vehicle systems: A review," *Chinese Journal of Aeronautics*, vol. 30, no. 1, pp. 135–148, 2017.

[59] S. H. Jeong and S. Jung, "Novel design and position control of an omni-directional flying automobile (Omni-Flymobile)," *Control Automation and Systems (ICCAS), 2010 International Conference on*, pp. 2480–2484, 2010.

[60] M. Elsamanty, M. Fanni, A. Ramadan, and A. Abo-Ismail, "Modeling and control of a novel Hybrid Ground Aerial Robot," *2013 IEEE International Conference on Mechatronics and Automation, IEEE ICMA 2013*, pp. 1559–1565, 2013.

[61] W. C. Myeong, K. Y. Jung, S. W. Jung, Y. H. Jung, and H. Myung, "Development of a drone-type wall-sticking and climbing robot," *2015 12th International Conference on Ubiquitous Robots and Ambient Intelligence, URAI 2015*, pp. 386–389, 2015.

[62] S. Jung, J. U. Shin, W. Myeong, and H. Myung, "Mechanism and system design of MAV(Micro Aerial Vehicle)-type wall-climbing robot for inspection of wind blades and non-flat surfaces," *ICCAS 2015 - 2015 15th International Conference on Control, Automation and Systems, Proceedings*, pp. 1757–1761, 2015.

[63] R. Siegwart, I. R. Nourbakhsh, and D. Scaramuzza, *Introduction to Autonomous Mobile Robots*. MIT Press, 2011.

[64] P. D. S. J. Dick and R. D. Launius, *Societal Impact of Space Flight*. 2013.

[65] W. Randal, W. Timothy, *Small Unmanned Aircraft*. 2012.

[66] William J. Hughes Technical Center NSTB/WAAS T&E Team, "Global Positioning System (GPS) Standard Positioning Service (SPS) Performance Analysis Report," 2014. [online] http://www.nstb.tc.faa.gov/reports/PAN85_0414.pdf [Accessed: 30-Dec-2018].

[67] Henri Eisenbeiß, *UAV Photogrammetry*. PhD thesis, 2009.

[68] L. S. Monteiro, T. Moore, and C. Hill, "What is the accuracy of DGPS?," *Journal of Navigation*, vol. 58, no. 2, pp. 207–225, 2005.

[69] J. N. Gross, Y. Gu, and M. B. Rhudy, "Robust UAV Relative Navigation with DGPS, INS, and Peer-to-Peer Radio Ranging," *IEEE Transactions on Automation Science and Engineering*, vol. 12, no. 3, pp. 935–944, 2015.

[70] R. Hahnemann, D. Schindler, M. Kamel, R. Siegwart, and J. Nieto, "A decentralized multi-agent unmanned aerial system to search, pick up, and relocate objects," *SSRR 2017 - 15th IEEE International Symposium on Safety, Security and Rescue Robotics, Conference*, pp. 123–128, 2017.

[71] S. Lee and Y. Choi, "Reviews of unmanned aerial vehicle (drone) technology trends and its applications in the mining industry," *Geosystem Engineering*, vol. 19, no. 4, pp. 197–204, 2016.

[72] A. Nishar, S. Richards, D. Breen, J. Robertson, and B. Breen, "Thermal infrared imaging of geothermal environments by UAV (unmanned aerial vehicle)," *Journal of Unmanned Vehicle Systems*, vol. 4, no. 2, pp. 136–145, 2016.

[73] Y. Song, B. Xian, Y. Zhang, X. Jiang, and X. Zhang, "Towards autonomous control of quadrotor unmanned aerial vehicles in a GPS-denied urban area via laser ranger finder," *Optik*, vol. 126, no. 23, pp. 3877–3882, 2015.

[74] L. Li, "Time-of-Flight Camera – An Introduction," 2014. [online] http://www.ti.com/lit/wp/sloa190b/sloa190b.pdf [Accessed: 30-Dec-2018].

[75] F. Wang, J. Cui, S. K. Phang, B. M. Chen, and T. H. Lee, "A mono-camera and scanning laser range finder based UAV indoor navigation system," *2013 International Conference on Unmanned Aircraft Systems, ICUAS 2013 - Conference Proceedings*, pp. 694–701, 2013.

[76] F. Bonnin-Pascual, A. Ortiz, E. Garcia-Fidalgo, and J. P. Company-Corcoles, "A reconfigurable framework to turn a MAV into an effective tool for vessel inspection," *Robotics and Computer-Integrated Manufacturing*, vol. 56, pp. 191–211, 2019.

[77] Z. Li, H. Zhang, J. Li, T. Yang, and P. Li, "Monocular Vision SLAM-Based UAV Autonomous Landing in Emergencies and Unknown Environments," *Electronics*, vol. 7, no. 5, p. 73, 2018.

[78] N. Gageik, P. Benz, and S. Montenegro, "Obstacle detection and collision avoidance for a UAV with complementary low-cost sensors," *IEEE Access*, vol. 3, pp. 599–609, 2015.

[79] D. P. Massa, "Choosing an Ultrasonic Sensor for Proximity or Distance Measurement Part 1: Acoustic Considerations | Sensors," *Sensors (Peterborough, NH)*, vol. 26, no. 8, pp. 1–6, 1999.

[80] U. Papa and G. Del Core, "Design of sonar sensor model for safe landing of an UAV," *2nd IEEE International Workshop on Metrology for Aerospace, MetroAeroSpace 2015 - Proceedings*, pp. 346–350, 2015.

[81] Z. Yan, L. Fabresse, J. Laval, and N. Bouraqadi, "Metrics for performance benchmarking of multi-robot exploration," *IEEE International Conference on Intelligent Robots and Systems*, vol. 2015-Decem, pp. 3407–3414, 2015.

[82] R. S. Lim, H. M. La, and W. Sheng, "A robotic crack inspection and mapping system for bridge deck maintenance," *IEEE Transactions on Automation Science and Engineering*, vol. 11, no. 2, pp. 367–378, 2014.

[83] D. Nister, O. Naroditsky, and J. Bergen, "Visual odometry," pp. 652–659, 2004.

[84] H. Durrant-Whyte, D. Rye, and E. Nebot, "Localization of Autonomous Guided Vehicles," *Robotics Research*, pp. 613–625, 2011.

[85] A. J. Davison, I. D. Reid, N. D. Molton, and O. Stasse, "MonoSLAM: Real-time single camera SLAM," *IEEE Transactions on Pattern Analysis and Machine Intelligence*, vol. 29, no. 6, pp. 1052–1067, 2007.

[86] G. C. De Croon, C. De Wagter, B. D. Remes, and R. Ruijsink, "Sky segmentation approach to obstacle avoidance," *IEEE Aerospace Conference Proceedings*, 2011.

[87] S. Majumder, R. Shankar, and M. S. Prasad, "Obstacle size and proximity detection using stereo images for agile aerial robots," *2nd International Conference on Signal Processing and Integrated Networks, SPIN 2015*, pp. 437–442, 2015.

[88] A. Huang, N. Roy, A. Bachrach, P. Henry, M. Krainin, D. Maturana, and D. Fox, "Visual Odometry and Mapping for Autonomous Flight Using an RGB-D Camera," *Springer Tracts in Advanced Robotics*, vol. 100, pp. 235–252, 2011.

[89] S. Hrabar, "3D path planning and stereo-based obstacle avoidance for rotorcraft UAVs," *2008 IEEE/RSJ International Conference on Intelligent Robots and Systems, IROS*, pp. 807–814, 2008.

[90] L. R. García Carrillo, A. E. Dzul López, R. Lozano, and C. Pégard, "Combining stereo vision and inertial navigation system for a quad-rotor UAV," *Journal of Intelligent and Robotic Systems: Theory and Applications*, vol. 65, no. 1-4, pp. 373–387, 2012.

[91] M. Kass, A. Witkin, and D. Terzopoulos, "Snakes: Active contour models," *International Journal of Computer Vision,*, pp. 321–331, 1988.

[92] Y. Lai, "How Does the Kinect Work?," *Imid 2009*, pp. 1069–1072, 2009.

[93] M. Iacono and A. Sgorbissa, "Path following and obstacle avoidance for an autonomous UAV using a depth camera," *Robotics and Autonomous Systems*, vol. 106, pp. 38–46, 2018.

[94] M. C. Santos, L. V. Santana, A. S. Brandao, and M. Sarcinelli-Filho, "UAV obstacle avoidance using RGB-D system," *2015 International Conference on Unmanned Aircraft Systems, ICUAS 2015*, pp. 312–319, 2015.

[95] J. M. Santos, M. S. Couceiro, D. Portugal, and R. P. Rocha, "A Sensor Fusion Layer to Cope with Reduced Visibility in SLAM," *Journal of Intelligent and Robotic Systems: Theory and Applications*, vol. 80, no. 3-4, pp. 401–422, 2015.

[96] Vicon, "Go Further with Vicon MX T-Series," 2011.

[97] P. Merriaux, Y. Dupuis, R. Boutteau, P. Vasseur, and X. Savatier, "A study of vicon system positioning performance," *Sensors (Switzerland)*, vol. 17, no. 7, 2017.

[98] F. M. Palacios, E. S. E. Quesada, G. Sanahuja, S. Salazar, O. G. Salazar, and L. R. G. Carrillo, "Test bed for applications of heterogeneous unmanned vehicles," *International Journal of Advanced Robotic Systems*, vol. 14, no. 1, 2017.

[99] E. G. Rojo-Rodriguez, O. Garcia, E. J. Ollervides, P. Zambrano-Robledo, and E. S. Espinoza-Quesada, "Robust Consensus-Based Formation Flight for Multiple Quadrotors," *Journal of Intelligent and Robotic Systems: Theory and Applications*, pp. 1–14, 2018.

[100] R. Summan, S. G. Pierce, C. N. Macleod, G. Dobie, T. Gears, W. Lester, P. Pritchett, and P. Smyth, "Spatial calibration of large volume photogrammetry based metrology systems," *Measurement: Journal of the International Measurement Confederation*, vol. 68, pp. 189–200, 2015.

[101] E. W. SWOKOWSKI, *Calculus with Analytic Geometry*. Taylor & Francis, 1979.

[102] C. N. MacLeod, *Considerations for automated NDE applications*. PhD thesis, 2014.

[103] Ascending Technologies, "AscTec AutoPilot," 2015. [online] http://wiki.asctec.de/display/AR/AscTec+AutoPilot [Accessed: 30-Dec-2018].

[104] Y. Gu, M. Zhou, S. Fu, and Y. Wan, "Airborne WiFi networks through directional antennae: An experimental study," *2015 IEEE Wireless Communications and Networking Conference, WCNC 2015*, pp. 1314–1319, 2015.

[105] D. International, "XBee/XBee-PRO S1 802.15.4 (Legacy) User Guide." [online] https://www.sensefly.com/industry/engineering-construction-drones/ [Accessed: 26-April-2019].

[106] Ascending Technologies, "XBee Modules," 2015. [online] http://wiki.asctec.de/display/AR/XBee+Modules [Accessed: 30-Dec-2018].

[107] Microsoft, "C# Guide," 2018. [online] https://docs.microsoft.com/en-us/dotnet/csharp/ [Accessed: 30-Dec-2018].

[108] D. Mellinger, *Trajectory generation and control for quadrotors*. PhD thesis, 2012.

[109] Hokuyo, "Scanning Laser Range Finder URG-04LX Specifications," 2005. [online] https://www.hokuyo-aut.jp/dl/Specifications_URG-04LX_1513063395.pdf [Accessed: 31-Oct-2018].

[110] A. Zulu and S. John, "A Review of Control Algorithms for Autonomous Quadrotors," *Open Journal of Applied Sciences*, vol. 04, no. 14, pp. 547–556, 2014.

[111] S. Bennett, "A Brief History of Automatic Control," *IEEE Control Systems*, vol. 16, no. 3, pp. 17–25, 1996.

[112] Araki M, "Pid Control," *Control systems, robotics and automation*, 2002.

[113] G. M. Hoffmann, H. Huang, S. L. Waslander, and C. J. Tomlin, "Precision flight control for a multi-vehicle quadrotor helicopter testbed," *Control Engineering Practice*, vol. 19, no. 9, pp. 1023–1036, 2011.

[114] H. Liu, Y. Bai, G. Lu, and Y. Zhong, "Robust attitude control of uncertain quadrotors," *IET Control Theory & Applications*, vol. 7, no. 11, pp. 1583–1589, 2013.

[115] L. Zadeh, "Fuzzy sets," *Information and Control*, vol. 8, pp. 338–353, Jun 1965.

[116] L. Reznik, *Fuzzy Controllers*, vol. 1. 1987.

[117] T. Sangyam, "Autonomous path tracking and disturbance force rejection of UAV using fuzzy based auto-tuning PID controller," *... (Ecti-Con), 2010 ...*, pp. 4–7, 2010.

[118] K. Astrom and R. M. Murray, *Feedback systems: an introduction for scientists and engineers*, vol. 46. 2013.

[119] B. Anderson and J. B. Moore, "Optimal control: linear quadratic methods," *Prentice Hall information and system sciences series*, pp. xi, 380 p., 1990.

[120] K. Alexis, "LQR Flight Control," 2016. [online] http://www.kostasalexis.com/uploads/5/8/4/4/58449511/10_flightcontrol_lq.pdf [Accessed: 30-Dec-2018].

[121] J. C. Lozier, "A steady state approach to the theory of saturable servo systems," *IRE Transactions on Automatic Control*, vol. 1, no. 1, pp. 19–39, 1956.

[122] N. E. Kahveci, P. A. Ioannou, and M. D. Mirmirani, "Adaptive LQ control with anti-windup augmentation to optimize UAV performance in autonomous soaring applications," *IEEE Transactions on Control Systems Technology*, vol. 16, no. 4, pp. 691–707, 2008.

[123] C. Hajiyev and S. Y. Vural, "LQR Controller with Kalman Estimator Applied to UAV Longitudinal Dynamics," *Positioning*, vol. 04, no. 01, pp. 36–41, 2013.

[124] L. M. Argentim, W. C. Rezende, P. E. Santos, and R. A. Aguiar, "PID, LQR and LQR-PID on a quadcopter platform," *2013 International Conference on Informatics, Electronics and Vision, ICIEV 2013*, 2013.

[125] S. Khatoon, D. Gupta, and L. K. Das, "PID & LQR control for a quadrotor: Modeling and simulation," *Proceedings of the 2014 International Conference on Advances in Computing, Communications and Informatics, ICACCI 2014*, pp. 796–802, 2014.

[126] P. V. Kokotović, "The Joy of Feedback: Nonlinear and Adaptive," *IEEE Control Systems*, vol. 12, no. 3, pp. 7–17, 1992.

[127] H. K. Khalil, *Nonlinear Systems*. 2002.

[128] S. Bouabdallah and R. Siegwart, "Backstepping and sliding-mode techniques applied to an indoor micro Quadrotor," *Proceedings - IEEE International Conference on Robotics and Automation*, vol. 2005, pp. 2247–2252, 2005.

[129] X. Huo, M. Huo, and H. R. Karimi, "Attitude stabilization control of a quadrotor UAV by using backstepping approach," *Mathematical Problems in Engineering*, vol. 2014, 2014.

[130] S. Bouabdallah and R. Siegwart, "Full control of a quadrotor," *IEEE International Conference on Intelligent Robots and Systems*, pp. 153–158, 2007.

[131] J. Colorado, A. Barrientos, A. Martinez, B. Lafaverges, and J. Valente, "Mini-quadrotor attitude control based on hybrid backstepping & Frenet-Serret theory," *Proceedings - IEEE International Conference on Robotics and Automation*, pp. 1617–1622, 2010.

[132] H. Mo and G. Farid, "Nonlinear and Adaptive Intelligent Control Techniques for Quadrotor UAV - A Survey," *Asian Journal of Control*, 2018.

[133] J. Escareño, S. Salazar, H. Romero, and R. Lozano, "Trajectory control of a quadrotor subject to 2D wind disturbances: Robust-adaptive approach," *Journal of Intelligent and Robotic Systems: Theory and Applications*, vol. 70, no. 1-4, pp. 51–63, 2013.

[134] Z. T. Dydek, A. M. Annaswamy, and E. Lavretsky, "Adaptive control of quadrotor UAVs: A design trade study with flight evaluations," *IEEE Transactions on Control Systems Technology*, vol. 21, no. 4, pp. 1400–1406, 2013.

[135] K. D. Young, V. I. Utkin, and Ü. Özgüner, "A control engineer's guide to sliding mode control," *IEEE Transactions on Control Systems Technology*, vol. 7, no. 3, pp. 328–342, 1999.

[136] L. Jinkun, "Sliding Mode Control Using MATLAB," 2017.

[137] R. Xu and U. Ozguner, "Sliding Mode Control of a Quadrotor Helicopter," *Proceedings of the 45th IEEE Conference on Decision and Control*, pp. 4957–4962, 2006.

[138] A. Benallegue, A. Mokhtari, and L. Fridman, "High-order sliding-mode observer for a quadrotor UAV," *International Journal of Robust and Nonlinear Control*, vol. 18, no. 4-5, pp. 427–440, 2008.

[139] C. Peng, Y. Bai, X. Gong, Q. Gao, C. Zhao, and Y. Tian, "Modeling and robust backstepping sliding mode control with Adaptive RBFNN for a novel coaxial eight-rotor UAV," *IEEE/CAA Journal of Automatica Sinica*, vol. 2, no. 1, pp. 56–64, 2015.

[140] F. Muñoz, I. González-Hernández, S. Salazar, E. S. Espinoza, and R. Lozano, "Second order sliding mode controllers for altitude control of a quadrotor UAS: Real-time implementation in outdoor environments," *Neurocomputing*, vol. 233, pp. 61–71, 2017.

[141] Z. Jia, J. Yu, Y. Mei, Y. Chen, Y. Shen, and X. Ai, "Integral backstepping sliding mode control for quadrotor helicopter under external uncertain disturbances," *Aerospace Science and Technology*, vol. 68, pp. 299–307, 2017.

[142] C. V. Girish, F. Emilio, H. P. Jonathan, and L. Hugh, "Nonlinear Flight Control Techniques for Unmanned Aerial Vehicles," in *Handbook of Unmanned Aerial Vehicles*, pp. 577–612, Dordrecht: Springer Netherlands, 2015.

[143] J. P. How, E. Frazzoli, and G. V. Chowdhary, "Linear Flight Control Techniques for Unmanned Aerial Vehicles," in *Handbook of Unmanned Aerial Vehicles*, pp. 529–576, Dordrecht: Springer Netherlands, 2015.

[144] H. t. M. N. Elkholy and H. t. M. Nabil, "Dynamic Modeling and Control of a Quadrotor Using Linear and Nonlinear Approaches," *The American University in Cairo*, 2014.

[145] F. Furrer, M. Burri, M. Achtelik, and R. Siegwart, "Robot operating system (ros)," *Studies Comp.Intelligence Volume Number:625*, vol. The Complete Reference (Volume 1), no. 978-3-319-26052-5, p. Chapter 23, 2016. ISBN:978-3-319-26052-5.

[146] L. Kneip, F. Tache, G. Caprari, and R. Siegwart, "Characterization of the compact Hokuyo URG-04LX 2D laser range scanner," in *2009 IEEE International Conference on Robotics and Automation*, 2009.

[147] C. N. Macleod, R. Summan, G. Dobie, and S. G. Pierce, "Quantifying and improving laser range data when scanning industrial materials," *IEEE Sensors Journal*, vol. 16, no. 22, pp. 7999–8009, 2016.

[148] H. Kawata, A. Ohya, S. Yuta, W. Santosh, and T. Mori, "Development of ultra-small lightweight optical range sensor system," *2005 IEEE/RSJ International Conference on Intelligent Robots and Systems, IROS*, pp. 3277–3282, 2005.

[149] V. Nguyen, A. Martinelli, N. Tomatis, and R. Siegwart, "A comparison of line extraction algorithms using 2D laser rangefinder for indoor mobile robotics," *2005 IEEE/RSJ International Conference on Intelligent Robots and Systems, IROS*, pp. 1768–1773, 2005.

[150] P. Bourke, "Minimum Distance between a Point and a Line," pp. 1–2, 1988.

[151] I. Colomina and P. Molina, "Unmanned aerial systems for photogrammetry and remote sensing: A review," *ISPRS Journal of Photogrammetry and Remote Sensing*, vol. 92, pp. 79–97, 2014.

[152] H. F. Zhou, H. Y. Dou, L. Z. Qin, Y. Chen, Y. Q. Ni, and J. M. Ko, "A review of full-scale structural testing of wind turbine blades," *Renewable and Sustainable Energy Reviews*, vol. 33, pp. 177–187, 2014.

[153] J. Sabel, "Optical 3D motion measurement," *In Instrumentation and Measurement Technology Conference, 1996. IMTC-96. Conference Proceedings. Quality Measurements: The Indispensable Bridge between Theory and Reality., IEEE*, vol. 1, pp. 367–370, 1996.

[154] J. T. Johnson, S. Hughes, and J. van Dam, "A stereo-videogrammetry system for monitoring wind turbine blade surfaces during structural testing," *Journal Name: ASME Early Career Technical Journal*, vol. 8, no. 1, 2009.

[155] T. Lundstrom, J. Baqersad, C. Niezrecki, and P. Avitabile, "Using high-speed stereophotogrammetry techniques to extract shape information from wind turbine/rotor operating data," *Conference Proceedings of the Society for Experimental Mechanics Series*, vol. 6, pp. 269–275, 2012.

[156] L. Wang and Z. Zhang, "Automatic Detection of Wind Turbine Blade Surface Cracks Based on UAV-Taken Images," *IEEE Transactions on Industrial Electronics*, vol. 64, no. 9, pp. 7293–7309, 2017.

[157] M. Stokkeland, K. Klausen, and T. A. Johansen, "Autonomous visual navigation of Unmanned Aerial Vehicle for wind turbine inspection," *2015 International Conference on Unmanned Aircraft Systems, ICUAS 2015*, pp. 998–1007, 2015.

[158] G. Morgenthal and N. Hallermann, "Quality Assessment of Unmanned Aerial Vehicle (UAV) Based Visual Inspection of Structures," *Advances in Structural Engineering*, vol. 17, no. 3, pp. 289–302, 2014.

[159] J. O'Connor, M. J. Smith, and M. R. James, "Cameras and settings for aerial surveys in the geosciences: Optimising image data," *Progress in Physical Geography*, vol. 41, pp. 325–344, Mar 2017.

[160] Agisoft LLC, "Agisoft PhotoScan User Manual: Professional Edition, Version 1.4," 2018. [online] http://www.agisoft.com/pdf/photoscan-pro_1_4_en.pdf [Accessed: 07-Nov-2018].

[161] GOM, "ATOS Triple Scan," 2015. [online] http://www.gom.com/metrology-systems/system-overview/atos-triple-scan.html [Accessed: 07-Nov-2018].

[162] N. Snavely, S. M. Seitz, and R. Szeliski, "Photo tourism," *ACM SIGGRAPH 2006 Papers on - SIGGRAPH '06*, p. 835, 2006.

[163] Y. Furukawa and J. Ponce, "Accurate, dense, and robust multiview stereopsis," *IEEE Transactions on Pattern Analysis and Machine Intelligence*, vol. 32, no. 8, pp. 1362–1376, 2010.

[164] J. Engel, T. Schops, and D. Cremers, "LSD-SLAM: Large-Scale Direct monocular SLAM," *Lecture Notes in Computer Science (including subseries Lecture Notes in Artificial Intelligence and Lecture Notes in Bioinformatics)*, vol. 8690 LNCS, no. PART 2, pp. 834–849, 2014.

[165] R. a. N. Rse, "KinectFusion : Real-Time Dense Surface Mapping and Tracking," 2013.

[166] A. Rajput, E. Funk, A. Börner, and O. Hellwich, "A Regularized Volumetric Fusion Framework for Large-Scale 3D Reconstruction," *ISPRS Journal of Photogrammetry and Remote Sensing*, vol. 141, pp. 124–136, 2018.

[167] M. Keller, D. Lefloch, M. Lambers, S. Izadi, T. Weyrich, and A. Kolb, "Real-time 3D reconstruction in dynamic scenes using point-based fusion," *Proceedings - 2013 International Conference on 3D Vision, 3DV 2013*, pp. 1–8, 2013.

[168] Q. Peng, L. Tu, K. Zhang, and S. Zhong, "Automated 3D scenes reconstruction using multiple stereo pairs from portable four-camera photographic measurement system," *International Journal of Optics*, vol. 2015, pp. 1–9, 2015.

[169] L. Shapiro and G. Stockman, *Computer Vision*. 2011.

[170] K. N. Snavely, *Scene Reconstruction and Visualization from Internet Photo Collections*. PhD thesis, 2008.

[171] M. J. Westoby, J. Brasington, N. F. Glasser, M. J. Hambrey, and J. M. Reynolds, "'Structure-from-Motion' photogrammetry: A low-cost, effective tool for geoscience applications," *Geomorphology*, vol. 179, pp. 300–314, 2012.

[172] Autodesk, "Create accurate 3D models with reality capture," 2018. [online] https://www.autodesk.co.uk/products/recap/overview [Accessed: 30-Dec-2018].

[173] C. Wu, "VisualSFM : A Visual Structure from Motion System," 2011. [online] http://www.cs.washington.edu/homes/ccwu/vsfm [Accessed: 30-Dec-2018].

[174] M. Prosdocimi, M. Burguet, S. Di Prima, G. Sofia, E. Terol, J. Rodrigo Comino, A. Cerdà, and P. Tarolli, "Rainfall simulation and Structure-from-Motion photogrammetry for the analysis of soil water erosion in Mediterranean vineyards," *Science of the Total Environment*, vol. 574, pp. 204–215, 2017.

[175] V. Pradeep, C. Rhemann, S. Izadi, C. Zach, M. Bleyer, and S. Bathiche, "MonoFusion: Real-time 3D reconstruction of small scenes with a single web camera," *2013 IEEE International Symposium on Mixed and Augmented Reality, ISMAR 2013*, pp. 83–88, 2013.

[176] A. Masiero and A. Vettore, "Improved feature matching for mobile devices with IMU," *Sensors (Switzerland)*, vol. 16, no. 8, 2016.

[177] C. Eschmann and T. Wundsam, "Web-Based Georeferenced 3D Inspection and Monitoring of Bridges with Unmanned Aircraft Systems," *Journal of Surveying Engineering*, vol. 143, no. 3, p. 04017003, 2017.

[178] B. Riveiro and M. Solla, "Non-Destructive Techniques for the Evaluation of Structures and Infrastructure," p. 398, 2016.

[179] S. Foster and D. Halbstein, "Integrating 3D Modeling, Photogrammetry and Design," 2014.

[180] J. Gang, "Structured-light 3D surface imaging: a tutorial," *Advances in Optics and Photonics*, vol. 3, pp. 128–160, 2011.

[181] L. Zhang, B. Curless, and S. M. Seitz, "Rapid shape acquisition using color structured light and multi-pass dynamic programming," *Proceedings - 1st International Symposium on 3D Data Processing Visualization and Transmission, 3DPVT 2002*, pp. 24–36, 2002.

[182] A. Shpunt and Z. Zalevsky, "Depth-varying light fields for three dimensional sensing," 2007.

[183] Creative, "Intel RealSense 3D Camera: Technical Specifications," 2014. [online] http://support.creative.com/kb/ShowArticle.aspx?sid=124661 [Accessed: 30-Dec-2018].

[184] Y. Ji, Q. Xia, and Z. Zhang, "Fusing Depth and Silhouette for Scanning Transparent Object with RGB-D Sensor," *International Journal of Optics*, vol. 2017, 2017.

[185] P. Henry, M. Krainin, E. Herbst, X. Ren, and D. Fox, "RGB-D mapping: Using Kinect-style depth cameras for dense 3D modeling of indoor environments," *International Journal of Robotics Research*, vol. 31, no. 5, pp. 647–663, 2012.

[186] J. Shotton, A. Fitzgibbon, M. Cook, T. Sharp, M. Finocchio, R. Moore, A. Kipman, and A. Blake, "Real-time human pose recognition in parts from single depth images," in *CVPR 2011*, vol. 411, pp. 1297–1304, IEEE, Jun 2011.

[187] Y. Cui, S. Schuon, D. Chan, S. Thrun, and C. Theobalt, "3D shape scanning with a time-of-flight camera," *Proceedings of the IEEE Computer Society Conference on Computer Vision and Pattern Recognition*, pp. 1173–1180, 2010.

[188] A. Anwer, S. S. Azhar Ali, A. Khan, and F. Meriaudeau, "Underwater 3-D Scene Reconstruction Using Kinect v2 Based on Physical Models for Refraction and Time of Flight Correction," *IEEE Access*, vol. 5, pp. 15960–15970, 2017.

[189] FILR, "Chameleon3 5.0 MP Color USB3 Vision (Sony IMX264)," 2017. [online] https://eu.ptgrey.com/chameleon3-50-mp-color-usb3-vision-sony-imx264-3 [Accessed: 03-Nov-2018].

[190] Computar, "M0824-MPW2," 2017. [online] https://computar.com/product/1331/ [Accessed: 31-Oct-2018].

[191] J. J. Koenderink and A. J. van Doorn, "Affine structure from motion," *Journal of the Optical Society of America A*, vol. 8, no. 2, p. 377, 1991.

[192] R. Jain, R. Kasturi, and B. Schunck, *Machine Vision*. McGraw-Hill Education, 1995.

[193] F. Durand and B. Freeman, "Focus and Depth of Field." [online] https://groups.csail.mit.edu/graphics/classes/CompPhoto06/html/lecturenotes/22_DepthDefocus_6.pdf [Accessed: 30-December-2018].

[194] A. Adams and N. Willett, "Depth of field." [online] http://graphics.stanford.edu/courses/cs178-10/applets/dof.html [Accessed: 30-December-2018].

[195] Stephen H. Westin, "ISO 12233 Test Chart," 2010. [online] ttps://www.graphics.cornell.edu/~westin/misc/res-chart.html [Accessed: 10-Nov-2018].

[196] F. Crete, T. Dolmiere, P. Ladret, and M. Nicolas, "The blur effect: perception and estimation with a new no-reference perceptual blur metric," p. 64920I, 2007.

[197] C. Mineo, S. G. Pierce, P. I. Nicholson, and I. Cooper, "Robotic path planning for non-destructive testing - A custom MATLAB toolbox approach," *Robotics and Computer-Integrated Manufacturing*, vol. 37, pp. 1–12, 2016.

[198] K. Kraus, *Photogrammetry: Geometry from Images and Laser Scans*. Walter de Gruyter, 2007.

[199] T. C. Hutchinson and Z. Chen, "Improved Image Analysis for Evaluating Concrete Damage," *Journal of Computing in Civil Engineering*, vol. 20, no. 3, pp. 210–216, 2006.

[200] Y. Wu, Y. Qin, Z. Wang, and L. Jia, "A UAV-Based Visual Inspection Method for Rail Surface Defects," *Applied Sciences*, vol. 8, no. 7, p. 1028, 2018.

[201] K. Jang, N. Kim, and Y.-K. An, "Deep learning–based autonomous concrete crack evaluation through hybrid image scanning," *Structural Health Monitoring*, p. 147592171882171, Jan 2019.

[202] Rami A. Mattar and Remy Kalai, "Development of a Wall-Sticking Drone for Non-Destructive Ultrasonic and Corrosion Testing," *Drones*, vol. 2, no. 1, p. 8, 2018.

[203] R. Jarvis, F. Cegla, M. Kovac, and A. Farinha, "NDE sensor delivery using unmanned aerial vehicles," *Insight: Non-Destructive Testing and Condition Monitoring*, vol. 60, no. 8, pp. 463–467, 2018.

[204] TexoDrone, "UAV INTEGRATED UT GAUGE," 2018. [online] https://www.texodroneservices.co.uk/service/uav_integrated_ut [Accessed: 01-Dec-2018].

[205] Apellix, "UT," 2018. [online] https://www.apellix.com/ut-probe/ [Accessed: 12-Dec-2018].

[206] C. J. Hellier, *Handbook of Nondestructive Evaluation*. 2003.

[207] H. Zhang, S. Wu, D. Ta, K. Xu, and W. Wang, "Coded excitation of ultrasonic guided waves in long bone fracture assessment," *Ultrasonics*, vol. 54, no. 5, pp. 1203–1209, 2014.

[208] I. A. Veres, A. Cleary, G. Thursby, C. McKee, I. Armstrong, G. Pierce, and B. Culshaw, "Golay code modulation in low-power laser-ultrasound," *Ultrasonics*, vol. 53, no. 1, pp. 122–129, 2013.

[209] Z. Zhou, B. Ma, J. Jiang, G. Yu, K. Liu, D. Zhang, and W. Liu, "Application of wavelet filtering and Barker-coded pulse compression hybrid method to air-coupled ultrasonic testing," *Nondestructive Testing and Evaluation*, vol. 29, no. 4, pp. 297–314, 2014.

[210] Z. Nazarchuk, V. Skalskyi, and O. Serhiyenko, "Propagation of elastic waves in solids," *Foundations in Engineering Mechanics*, pp. 29–73, 2017.

[211] R. E. Johnson, *Engineering physics*, vol. 32. 1979.

[212] I. A. Viktorov, *Rayleigh and Lamb Waves, Physical Theory and Applications*. 1967.

[213] A. Safari and E. K. Akdoğan, "Piezoelectric and acoustic materials for transducer applications," *Piezoelectric and Acoustic Materials for Transducer Applications*, pp. 1–481, 2008.

[214] M. I. Haller and B. T. Khuri-Yakub, "A surface micromachined electrostatic ultrasonic air transducer," *IEEE Transactions on Ultrasonics, Ferroelectrics, and Frequency Control*, vol. 43, no. 1, pp. 1–6, 1996.

[215] M. Khoury, G. E. Tourtollet, and A. Schröder, "Contactless measurement of the elastic Young's modulus of paper by an ultrasonic technique," *Ultrasonics*, vol. 37, no. 2, pp. 133–139, 1999.

[216] R. Farlow, *Low noise techniques applied to a piezoceramic receiver for gas coupled ultrasonic flaw detection*. PhD thesis, 1998.

[217] T. Kundu, *Ultrasonic Nondestructive Evaluation*. 2004.

[218] H. O. Masahiko Hirao, "EMATs for Science and Industry : Noncontacting Ultrasonic Measurements ," p. 2016, 2016.

[219] Eddyfi, "Swift and Scorpion2 Remote-Access Tank Shell Inspection Solution," 2018. [online] https://www.silverwingndt.com/scorpion2/ [Accessed: 30-Dec-2018].

[220] Olympus, "NDT Instruments, RollerFORM," 2017. [online] https://www.olympus-ims.com/en/rollerform/ [Accessed: 30-Dec-2018].

[221] B. Drinkwater, R. Dwyer-Joyce, and P. Cawley, "A study of the transmission of ultrasound across solid–rubber interfaces," *The Journal of the Acoustical Society of America*, vol. 101, no. 2, pp. 970–981, 2002.

[222] KUKA, "KR AGILUS," 2015. [online] https://www.kuka.com/en-de/products/robot-systems/industrial-robots/kr-agilus [Accessed: 30-Dec-2018].

[223] X. Song, D. Ta, and W. Wang, "A base-sequence-modulated golay code improves the excitation and measurement of ultrasonic guided waves in long bones," *IEEE Transactions on Ultrasonics, Ferroelectrics and Frequency Control*, vol. 59, no. 11, pp. 2580–2583, 2012.

[224] J. Isla and F. Cegla, "Coded Excitation for Pulse-Echo Systems," *IEEE Transactions on Ultrasonics, Ferroelectrics, and Frequency Control*, vol. 64, no. 4, pp. 736–748, 2017.

[225] M. J. E. Golay, "Complementary Series," *IRE Transactions on Information Theory*, vol. 7, no. 2, pp. 82–87, 1961.

[226] B. Zhou, D. M. Green, and J. C. Middlebrooks, "Characterization of external ear impulse responses using Golay codes.," *The Journal of the Acoustical Society of America*, vol. 92, no. 2, pp. 1169–71, 1992.

[227] M. M. Daffalla and A. A. Babiker, "Adaptive Coding, Modulation and Filtering of Radar Signals," in *Topics in Radar Signal Processing*, InTech, May 2018.